Final Technical Report

High Efficiency Clean Combustion (HECC) Program

High Efficiency, Low Emissions Homogeneous Charge Compression Ignition (HCCI) Engines

Department of Energy Contract
DE-FC26-05NT-42412

Project Title: **High Efficiency, Low Emissions Homogeneous Charge Compression Ignition (HCCI) Engines**

High Efficiency Clean Combustion (HECC) Research Program

Recipient: **Caterpillar Inc.**
DOE Award No.: **DE-FC26-05NT-42412**
DOE Technology Manager: **Roland Gravel**
NETL Project Manager: **Carl Maronde**
Principal Investigator: **Chris Gehrke**
Program Manager: **Scott Fiveland**

DISCLAIMER

Final Report for Caterpillar / DOE High Efficiency Clean Combustion (HECC) Research Program

DOE Contract: DE-FC26-05NT42412

Executive Summary
This is the final report of the High Efficiency Clean Combustion (HECC) Research Program for the U.S. Department of Energy. Work under this co-funded program began in August 2005 and finished in July 2010. The objective of this program was to develop and demonstrate a low emission, high thermal efficiency engine system that met 2010 EPA heavy-duty on-highway truck emissions requirements (0.2g/bhp-hr NOx, 0.14g/bhp-hr HC and 0.01g/bhp-hr PM) with a thermal efficiency of 46%. To achieve this goal, development of diesel homogenous charge compression ignition (HCCI) combustion was the chosen approach. This report summarizes the development of diesel HCCI combustion and associated enabling technologies that occurred during the HECC program between August 2005 and July 2010.

This program showed that although diesel HCCI with conventional US diesel fuel was not a feasible means to achieve the program objectives, the HCCI load range could be increased with a higher volatility, lower cetane number fuel, such as gasoline, if the combustion rate could be moderated to avoid excessive cylinder pressure rise rates. Given the potential efficiency and emissions benefits, continued research of combustion with low cetane number fuels and the effects of fuel distillation are recommended. The operation of diesel HCCI was only feasible at part-load due to a limited fuel injection window. A 4% fuel consumption benefit versus conventional, low-temperature combustion was realized over the achievable operating range.

Several enabling technologies were developed under this program that also benefited non-HCCI combustion. The development of a 300MPa fuel injector enabled the development of extended lifted flame combustion. A design methodology for minimizing the heat transfer to jacket water, known as precision cooling, will benefit conventional combustion engines, as well as HCCI engines. An advanced combustion control system based on cylinder pressure measurements was developed. A Well-to-wheels analysis of the energy flows in a mobile vehicle system and a 2nd Law thermodynamic analysis of the engine system were also completed under this program.

Acknowledgement and Disclaimer
The material in this report is based upon work supported by the U.S. Department of Energy under Award No. DE-FC26-05NT42412. Any opinions, findings, conclusions or recommendations expressed in this material are those of the author and do not necessarily reflect the view of the Department of Energy.

Table of Contents

Table of Contents 5
Introduction 6
1. Combustion Development Activities 7
1.1: Diesel HCCI Feasibility Analysis 7
1.1.1: Single Cylinder HCCI Combustion Development 7
1.1.2: Liquid Wall Impingement Study 14
1.1.3: Variable Compression Ratio 25
1.1.4: Multi-cylinder PCCI Results 29
1.1.5: Conclusions on feasibility of diesel HCCI 34
1.2: Fuel Property Effects 36
1.2.1: Diesel Fuel Property Effects 36
1.2.2: Gasoline and Diesel Blending 38
1.3: Non-HCCI Combustion Development 42
1.3.1: Extended Flame Lift-off Combustion 42
1.3.2: K-factor Nozzle Geometry Effects 48
2: Enabling Component Technology Development 54
2.1: Advanced Fuel Injector Development 54
2.2: Variable Compression Ratio (VCR) Engine 57
2.3: Precision Cooling 62
2.3.1: Thermal Modeling of Jacket Water Heat Rejection in Block, Liner, and Head 62
2.3.2: Correlation of Jacket Water Conjugate Heat Transfer 65
2.3.3: Precision Engine JW Cooling Process Applied 70
2.4: Combustion Controls 72
3: Engine System Efficiency Analysis 80
3.1: Well-to-Wheels Analysis 80
3.2: 2nd Law Efficiency Analysis 93

Final Report for Caterpillar / DOE High Efficiency Clean Combustion (HECC) Research Program

DOE Award No. DE-FC26-05NT42412
Program Manger: Scott Fiveland
Caterpillar, Inc.
PO Box 1875
Peoria, IL 61656-1875
309-578-6543; Fiveland_Scott_B@cat.com

DOE Technology Development Manager: Roland Gravel
[roland.gravel@ee.doe.gov]

NETL Project Manager: Carl Maronde
[carl.maronde@netl.doe.gov]

Introduction

The objectives of this program were to develop and demonstrate a low emission, high thermal efficiency engine system that met 2010 EPA heavy-duty on-highway truck emissions requirements (0.2g/bhp-hr NOx, 0.14g/bhp-hr HC and 0.01g/bhp-hr PM) with a thermal efficiency of 46%. To achieve the 46% thermal efficiency goal, Caterpillar and its partners have pursued advanced forms of low-temperature diesel combustion, such as homogenous charge compression ignition (HCCI) and premixed charge compression ignition (PCCI) combustion. Both HCCI and PCCI are forms of premixed combustion. In the context of this paper, HCCI refers generically to premixed combustion and more specifically to cases with a significant time between the end of fuel injection and start of combustion. PCCI refers to premixed combustion where the direct fuel injection occurs late in the compression stroke and all or most of the fuel is injected prior to start of combustion.

Premixed, low temperature combustion has the potential to simultaneously achieve low NOx and soot emissions and high thermal efficiency. The nature of low temperature combustion presents several challenges to successful implementation. Proper mixture preparation, combustion control and excessive heat rejection were a few examples of challenges facing the program. Activities were focused on determining the feasibility of diesel HCCI and PCCI combustion, and developing enabling technologies.

This report will present a feasibility analysis of diesel premixed combustion and summarize the combustion development activities that support that analysis. Related non-HCCI combustion technologies that were developed in this program will then be discussed. This will be followed by a summary of the enabling component technologies that were developed. Finally engine system efficiency analysis activities will be reported.

1. Combustion Development Activities

To achieve the 46% thermal efficiency goal, combustion needed to be optimized to maximize expansion work, and pumping losses needed to be minimized. This could be accomplished by shortening the combustion duration, properly phasing combustion, and reducing in-cylinder heat transfer. To achieve low emissions, low temperature combustion was desired to reduce NOx emissions and air-fuel premixing was desired to minimize soot emissions. All these requirements could be achieved with HCCI combustion. However, proper mixture preparation, combustion control and load capability were all challenges that needed to be addressed to enable a feasible diesel HCCI combustion system

Combustion technology development was focused on developing an understanding of the mixing, combustion and emissions processes and in-cylinder heat transfer. Understanding the impact of mixture preparation and fuel properties on combustion rate and emissions was critical to expanding the engine load capability of HCCI and reducing emissions. A few non-HCCI combustion technologies were investigated as potential compatible solutions for situations when the engine was operating at conditions that were unfavorable to HCCI.

The combustion development activities resulted in an increased understanding of the capabilities and limitations of HCCI and PCCI combustion. This information was used to determine the feasibility of diesel premixed combustion for heavy-duty application. This analysis and a summary of the development work that supported it are discussed in the following section. Some of the enabling technologies developed for HCCI and PCCI are also valuable for non-HCCI combustion. The application of these technologies to non-HCCI combustion is discussed in Section 1.2.

1.1: Diesel HCCI Feasibility Analysis

Mixture preparation is a major challenge for high-efficiency, low temperature combustion. Achieving short burn durations and controlling emissions requires adequate control of the mixing process. Achieving high loads with good combustion efficiency and adequate PM emissions requires a high level of air utilization. Premixed combustion, such as homogeneous charge compression ignition (HCCI) or premixed charge compression ignition (PCCI), can produce short combustion durations, however, sufficient mixing and control of the ignition process are key to managing the burn rate and controlling emissions. The following sections describe work that was undertaken to understand the benefits and limitations of diesel HCCI combustion. All the test work in this section was performed using typical commercially available diesel fuel.

1.1.1: Single Cylinder HCCI Combustion Development

Single-cylinder engine experiments were conducted to better understand the impact of the primary combustion control parameters on the HCCI combustion process and emissions. The three primary control parameters studied were start of injection (SOI) timing, exhaust gas recirculation (EGR) and intake valve closing actuation (IVA). Data was collected from a single-cylinder test engine configured for HCCI operation, and operating at 1200 rpm and 6 bar BMEP. The compression ratio was 14:1 and the injector nozzle remained constant for all tests.

In the first set of data the start-of-injection (SOI) timing was held fixed, while the EGR fraction and the IVA setting were swept. The result of sweeping EGR and IVA is that a range of

combustion phasing is explored. The points that were tested can be seen in Figure 1.1.1a, along the operational limits that were encountered. Potential limits of operation include cylinder pressure rise rates, combustion stability (combustion retard limit) and minimum IVA control setting. For the second set of data, the EGR fraction was held constant at 50%, while the SOI timing and the IVA setting were swept. By testing a range of IVA values, a range of combustion phasing was explored for this data set as well. The points that were tested can be found in Figure 1.1.1b , along with the limits of operation. Regression modeling was performed on both of these data sets, and the results will be presented as contour plots in the discussion below.

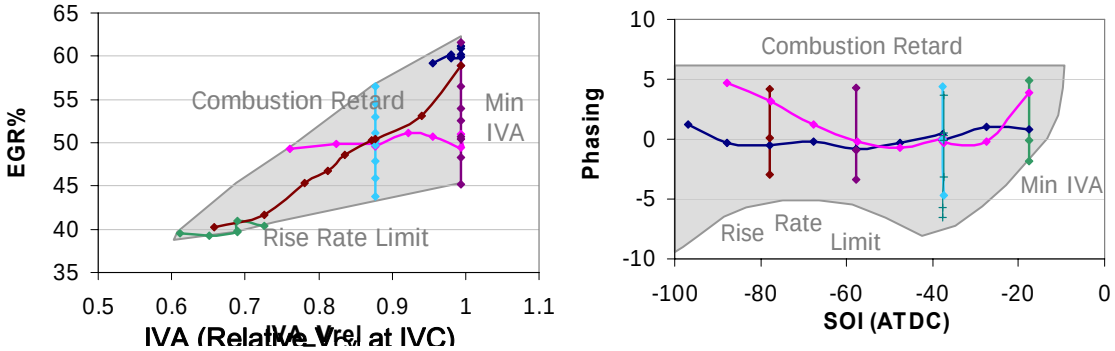

(a) **(b)**

Figure 1.1.1. Test points for (a)the constant SOI data set (EGR and IVA sweep) and (b)the 50% EGR data set (SOI and IVA sweep)

In all contour plots presented, a gray circle has been placed at the 50% EGR, 0 ATDC phasing, 40 SOI condition. In the contour plots for the constant SOI data set, the gray line shown corresponds to a line of constant IVA. In the contour plots for the constant EGR data set the gray line corresponds to a line of constant combustion phasing.

Cylinder Pressure Rise Rate

The rise rate plots are shown in Figure 1.1.2 for the two data sets. Excessive rise rates should be avoided since they lead to louder engine noise, greater structural requirements on the engine and have the potential to damage cylinder pressure transducers. For testing, the cylinder pressure rise rate was limited to 6 MPa/deg to minimize damage to the pressure transducers. The limit for a production heavy duty diesel will likely be around 2-3 MPa/deg to prevent engine noise from becoming too harsh and structural issues from being problematic over the lifetime of the engine.

Figure 1.1.2a shows the rise rate contours versus combustion phasing and EGR fraction. There is a combustion phasing effect (more advanced timings leads to higher rise rates), but there is also an EGR effect. For a given combustion phasing, the rise rates are better if more EGR is present. While the uses of IVA or EGR are equally effective at retarding combustion phasing, EGR is the more powerful method when rise rates are considered. Since the high-load challenge of HCCI involves balancing the air-fuel ratio limit with the rise rate limit, this suggests that a higher EGR fraction (versus more IVA) should allow for a higher load to be achieved. However, the engine pumping losses and heat rejection requirements of the cooling system increase with EGR fraction.

The effect that injection timing has on rise rates is shown in Figure 1.1.2b. Because these contours look more like a parabola and less like straight horizontal lines, it says that rise rates do depend on injection timing. Specifically, if we follow the gray constant phasing line, we find that rise rates peak around 60 BTDC, and get better as timing is either advanced or retarded from that point. The reason for this dependence is likely due to the lower local equivalence ratios due to the increased mixing time. To extend the load capability of the HCCI engine, it is desirable to run at the injection timing with less rise rates, all else being equal.

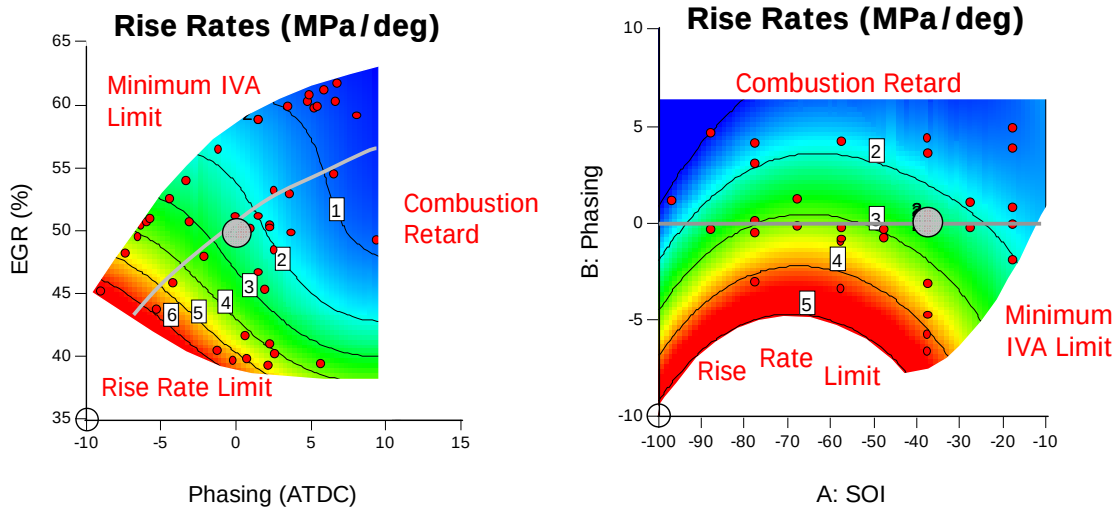

a. **b.**

Figure 1.1.2. Cylinder pressure rise rates for the constant SOI data set (a.), and the constant EGR data set (b.)

NOx emissions

NOx emissions for the two data sets are shown in Figure 1.1.3. The NOx emissions were found to be mostly dependent on combustion phasing and EGR fraction. NOx emissions did increase at retarded injection timings as the combustion became less premixed. When injection timing was more advanced than -30 deg adtc, the NOx emissions were relatively insensitive to the injection timing. Comparing the NOx emissions from Figure 1.1.3 with the cylinder pressure rise rate data in Figure 1.1.2**,** shows that the EGR level and combustion phasing at this load would be constrained by the 2-3 MPa/deg cylinder pressure rise rate limit and not by NOx emissions.

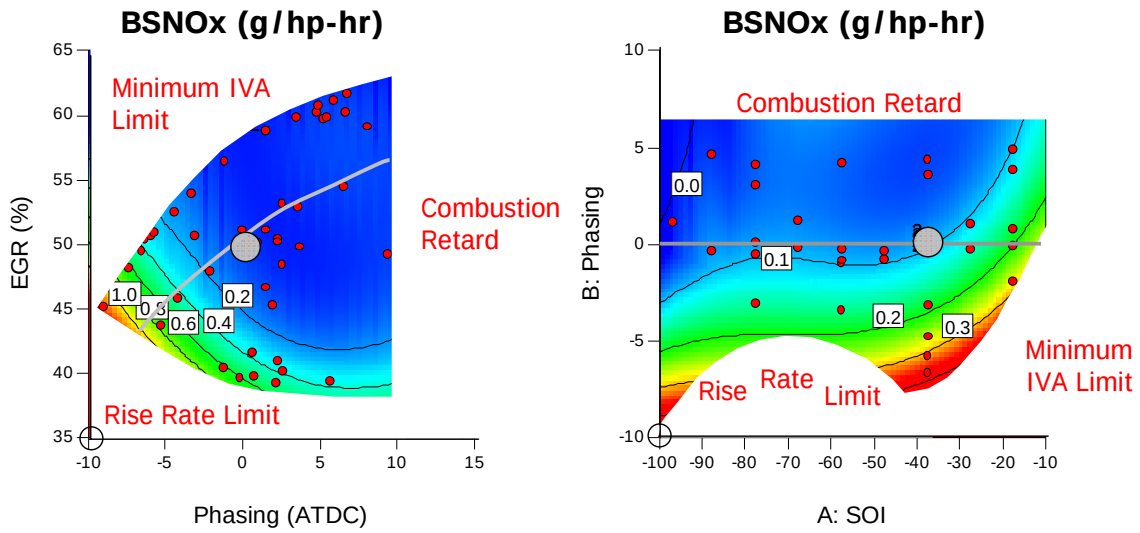

a. **b.**

Figure 1.1.3. Brake specific NOx emissions for the constant SOI data set (a.) and the constant EGR data set (b.)

Hydrocarbon Emissions

The hydrocarbon (HC) emissions for the two data sets are shown in Figure 1.1.4. The constant SOI data set in Figure 1.1.4a illustrates that the HC emissions are a strong function of combustion phasing. Hydrocarbon emissions are higher at retarded phasing and are lower with advanced phasing. According to the figure, the method of achieving a particular combustion phasing such as more IVA and less EGR versus more EGR and less IVA does not change the trend.

The HC emissions for the constant EGR data set are shown in Figure 1.1.4b. Here, two distinct trends can be seen. First, HC emissions are highly dependent on the fuel injection timing with HC emissions increasing as injection timing is advanced. This trend is most clearly seen in Figure 1.1.5, which is a plot of the slice of data taken from the contour plot of Figure 1.1.4b along the gray line (which corresponds to a constant combustion phasing of TDC). Also included on the contour plot of Figure 1.1.4b is a red line running through the "best compromise" point represented by the gray circle. This red line has a slope of one and represents a line of constant mixing time. For this particular line drawn, this time for mixing is about 37 crank degrees. If the contour lines paralleled this red line, it would suggest that HC emissions were a strong function of mixing time. However, in Figure 1.1.4b, the slope of the contours is less than one. This indicates that the HC emissions had a strong SOI dependence in addition to mixing time.

Figure 1.1.5 and Figure 1.1.6 give some insight into the strong dependence of HC emissions on the injection timing. Figure 1.1.5 shows that as injection timing was advanced, HC emissions appeared to increase in two distinct steps. The first increase occurred when injection timing was advanced from 60 BTDC to 70BTDC. The second increased occurred when timing was advanced from 90 BTDC to 100 BTDC. In Figure 1.1.6, the two plumes of the 50 x 90 showerhead injector (one at 50 degrees and one at 90 degrees) have been overlaid on a plot of the piston position for various injection timings. This figure indicates that the between 60 BTDC to

70 BTDC, the outer plume started spraying out of the bowl. Similarly, between 90 to 100 BTDC, the inner plume started to spray out of the bowl. This data suggests that the injection timing effect is linked to the ability to keep the fuel in the piston bowl. The fuel that escaped the bowl was likely either too lean or too cool for combustion, and hydrocarbon emissions were the result.

The current engine-out hydrocarbon goal is to achieve less than 1.0 g/hp-hr hydrocarbons. This would provide a level of HC that with a 90% conversion efficiency catalyst could meet the 2010 / Tier 4 emissions standards. Thus the allowable fuel injection window would be limited to earlier than 50 to 60 BTDC.

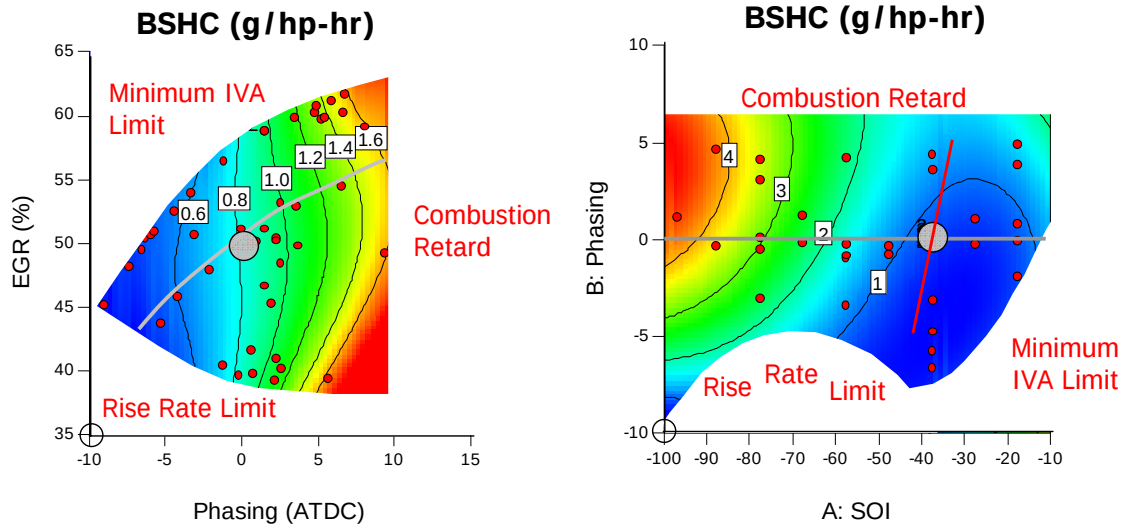

Figure 1.1.4. Brake specific unburned hydrocarbon emissions for the constant SOI data set (left) and the constant EGR data set (right)

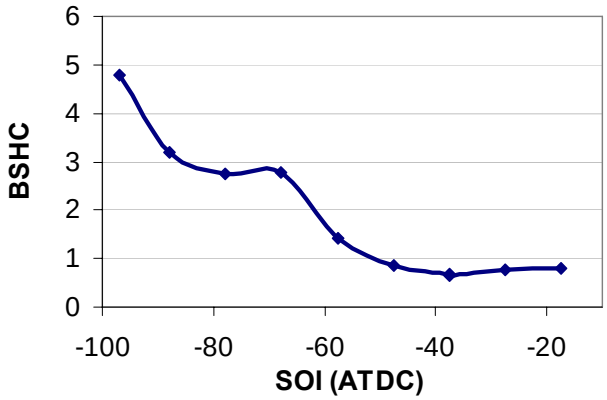

Figure 1.1.5. Hydrocarbon emissions for an SOI sweep performed at 0° ATDC combustion phasing

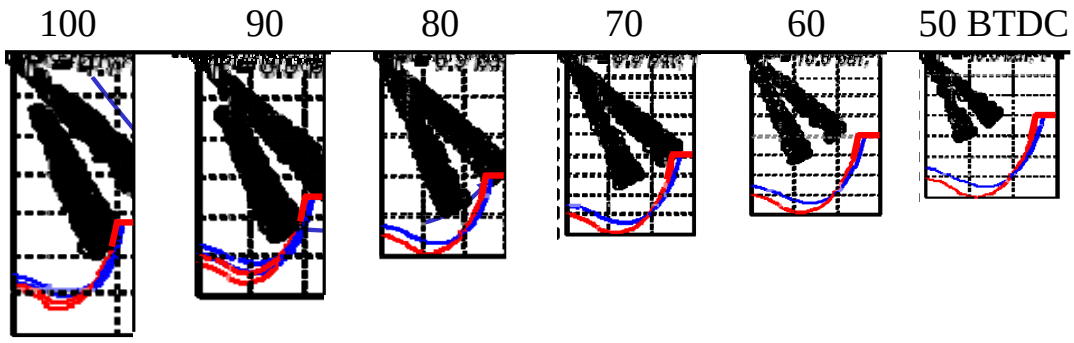

Figure 1.1.6. Piston location (blue line) relative to the liquid fuel spray for the different injection timings

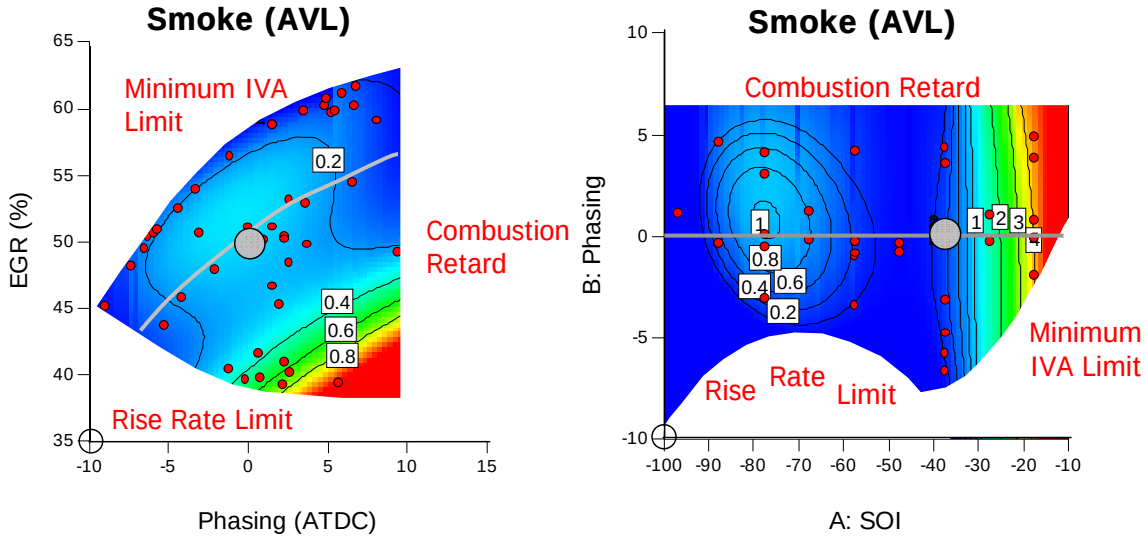

a. **b.**

Figure 1.1.7. Smoke emissions for the constant SOI data set (a.) and the constant EGR data set (b.)

Smoke Emissions

Contour plots of smoke emissions can be found in Figure 1.1.7. Examination of the smoke contour plot in Figure 1.1.7a reveals that the smoke contours tend to parallel the IVA contours (the gray line in the figure is a line of constant IVA). Increasing IVA (moving to the lower right corner) reduced the total mass and thus the density in the cylinder. When a significant amount of IVA was used, the cylinder densities at the time of injection (40 BTDC for the constant SOI data set) were greatly reduced. The increased use of IVA also lowered the gas temperatures during the entire compression stroke, including the time during the injection event and the mixture preparation process. Thus the fuel vaporization process could also have been affected.

Figure 1.1.7b shows the smoke trend with SOI timing. Two general features of the contour plot are evident. Smoke increased rapidly as injection timing was retarded toward top-dead-center, and a local smoke maximum exists at advanced timings. The existence of the local smoke

maximum was unexpected. The advanced injection timing should allow for greater premixing and lower soot emissions. The increase in smoke emissions also seemed to parallel the increase in HC emissions between 50 and 70 BTDC. This phenomenon will be discussed further in Section 1.1.2:.

CO emissions

CO emissions can be found in Figure 1.1.8. CO emissions can be produced by locally rich mixtures or by quenching at low temperatures. If the temperatures are too low, the reaction kinematics of the CO to CO2 oxidation reaction are too slow which essentially prevents the reaction from occurring.

Figure 1.1.8a reveals that CO emissions increased as we moved to the top-right corner of the contour plot (i.e. retarded combustion and elevated EGR). Comparing this contour plot to the NOx plot of Figure 1.1.3a, suggests that this increase in CO emissions could be due to the low temperature. If locally rich equivalence ratios were the challenge, we would expect that high CO would occur all along the right-hand side of the CO contour plot where the equivalence ratio is the highest. Since the highest CO emissions are concentrated in the upper right corner, we concluded that the CO emissions are due to low temperature quenching.

Figure 1.1.8b reveals two regions of high CO emissions, one at the top-left and one at the top-right. Looking to the NOx contours in Figure 1.1.3b, extremely low NOx emissions were observed in the upper left corner, which suggests this spike might be attributed to the low-temperature mechanism. However, only moderately low NOx was observed in the top-right corner. The local equivalence ratio would have increased as the injection timing is retarded towards top-dead center. The mixing time decreased, and thus local equivalence ratios were likely richer. Thus, the mechanism responsible for the CO spike in the top-right corner was likely the locally rich mechanism.

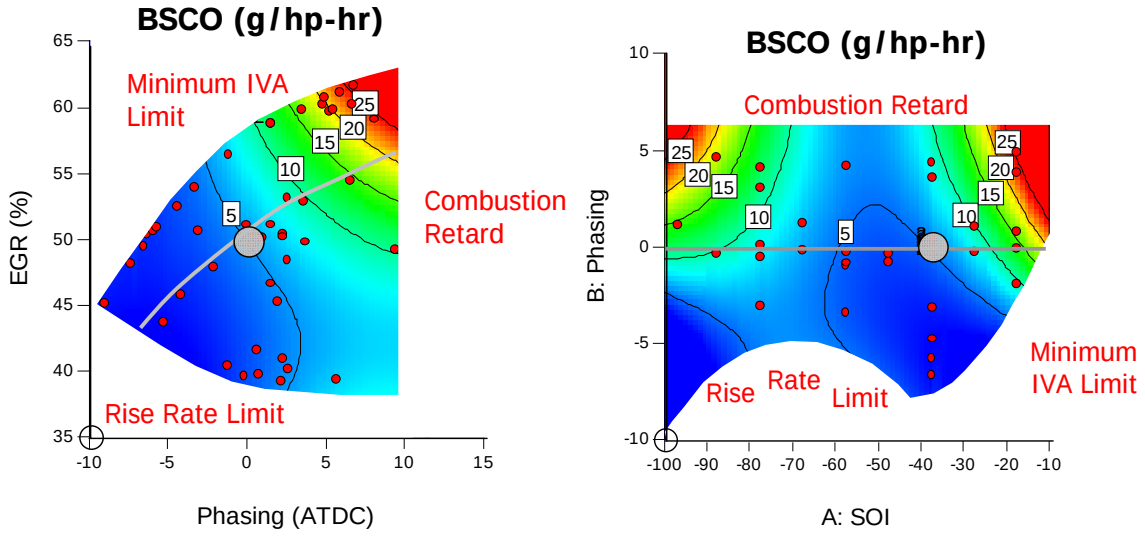

Figure 1.1.8. Brake specific CO emissions for the constant SOI data set (left) and the constant EGR data set (right)

Conclusions

The challenges associated with utilizing HCCI diesel combustion were demonstrated with this parametric study of combustion control variables at a single engine operating condition. The results showed that cylinder pressure rise rate, smoke emissions and HC emissions were the constraining factors. NOx and CO emissions were considered, but were less constraining at the test condition.

Cylinder pressure rise rates generally limited the combustion phasing to after TDC and EGR rates greater than 45-50%. This also ensured that NOx emissions were sufficiently low. HC emissions limited the amount of combustion phasing retard to about 5 ATDC, and also limited the SOI timing to earlier than 50 BTDC. Thus HC emissions put a limit on the maximum ignition delay. Soot emission required sufficient ignition delay for premixing, and thus further constrained the SOI. At the test condition, an ignition delay of 30-40 deg was required. Thus SOI needed to begin before 30-40 BTDC. Similar to HC and smoke, CO emissions required sufficient premixing to avoid locally rich equivalence ratios and required sufficiently advance combustion phasing to avoid quenching. However, the limits at the test condition were less constraining than HC or smoke emissions.

This data set also illustrates the challenge with increasing the load capability of HCCI combustion. At the test condition, the allowable SOI window was limited between 40 and 50 BTDC. As fueling is increased, the time needed for premixing must also increase thus requiring an earlier SOI. Thus, in this case, maximum engine load would be limited by the 50 BTDC SOI constraint. Understanding and ultimately moving this limit on SOI advance is critical to enabling HCCI combustion at high engine loads. This is the focus of the next section.

1.1.2: Liquid Wall Impingement Study

The goal of this task is to use the Sandia Compression-ignition Optical Research Engine (SCORE) to support the development of High Efficiency Clean Combustion (HECC) strategies that industry will use to meet upcoming stringent emissions regulations without sacrificing engine efficiency. The SCORE is a single-cylinder version of a Caterpillar® 3176/C-10 heavy-duty diesel engine that has been modified to provide extensive optical access into the cylinder. A schematic of the engine showing the optical access modifications is provided in Figure 1.1.9 and its basic hardware parameters are shown in Table 1.1.1. More detailed specifications of the optical engine are provided in Ref. [1].

For the testing described here, the engine was equipped with a hydraulically-actuated electronically-controlled unit injector (HEUI). The general specifications of the fuel-injection system are provided in Table 1.1.2. For this study, the injector was equipped with a 15-hole, dual-row, narrow-included-angle nozzle (10 holes x 70° and 5 holes x 35°) with 103 µm orifices. Figure 1.1.9 provides an axial slice through the center of the cylinder bore showing the alignment of two outer-row and one inner-row fuel sprays. The 70° included angle of the outer row of 10 evenly spaced orifices was chosen such that liquid fuel would impinge fully within the piston bowl for start of injection (SOI) timings as early as 70° before TDC (BTDC). The inner row of 5 evenly spaced orifices was aligned such that the axis of every other outer-row jet was co-planar with the axis of an inner-row jet and the cylinder-bore axis.

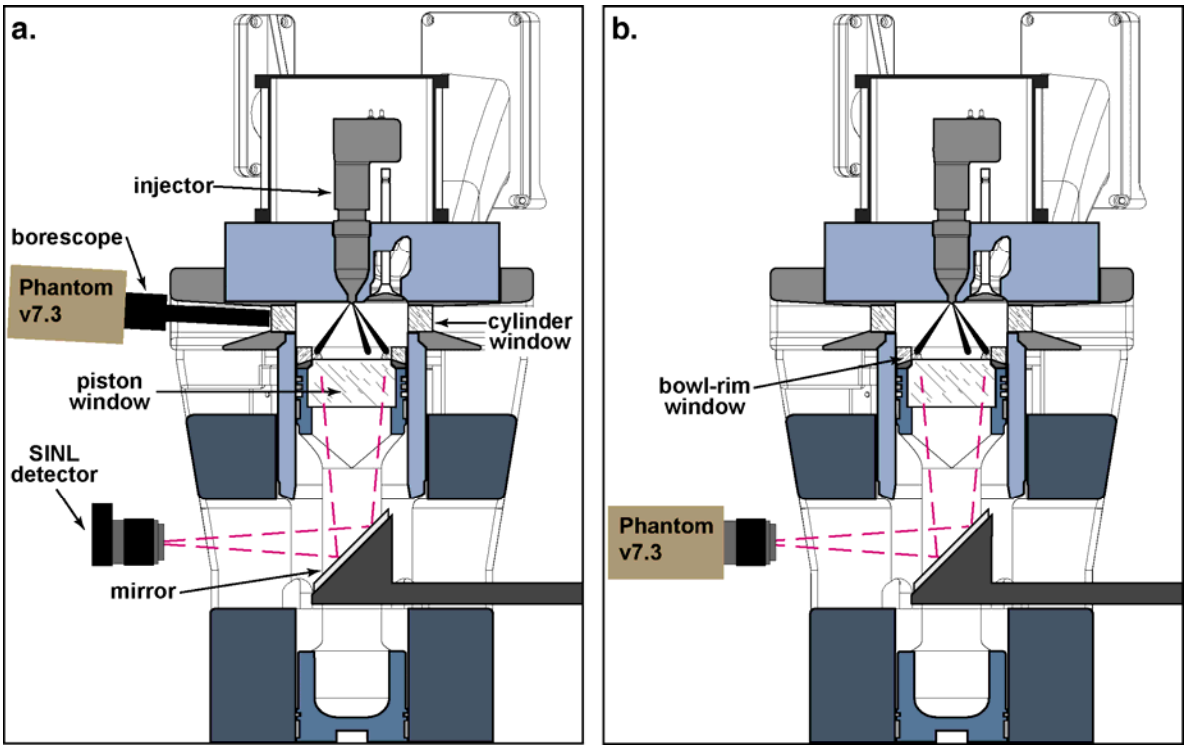

Figure 1.1.9. Schematic of SCORE configured for collecting SINL data and high-speed movies. a. Setup for high-speed imaging through the cylinder window. b. Setup for high-speed imaging through the piston window.

Table 1.1.1: SCORE Specifications

Research engine type	1-cyl. version of C-10/3176
Cycle	4-stroke CIDI
Valves per cylinder	4
Bore	125 mm
Stroke	140 mm
IVO[a]	32° BTDC exhaust
IVC[a]	153° BTDC comp.
EVO[a]	116° ATDC comp.
EVC[a]	11° ATDC exhaust
Connecting rod length	225 mm
Connecting rod offset	None
Piston bowl diameter	90 mm
Piston bowl depth	16.4 mm
Squish height	1.5 mm
Swirl ratio[b]	0.59
Displacement per cyl.	1.72 liters
Compression ratio	11.76:1

[a]All valve timings are for 0.03 mm lift

[b]Measured at the Caterpillar Technical Center using an AVL swirl meter

Table 1.1.2: SCORE Fuel-Injection System Specifications

Injector type	Cat® HEUI™ A
Injector model	HIA-450
Nozzle style	Single-guided
Outer row	10 x 103 µm x 70° VCO
Inner row	5 x 103 µm x 35° minisac
Orifice diameter	103µm
Oil rail pressure	20.8 MPa (3000 psig)
Max. injection pressure	142 MPa (20600 psia)
Intensification ratio	6.85:1
Valve opening pressure	31 MPa (4500 psig)

Optical measurements

In-cylinder spray-visualization and natural-luminosity (NL) movies were acquired using a Phantom V7.3, 14 bit, high-speed camera. Two camera views were utilized to provide quasi-3D information about the in-cylinder fuel penetration, mixing, and combustion. The first camera view images through a cylinder-wall window, see Figure 1.1.9a. This setup utilizes a 20-mm-diameter borescope with a 115° field of view that enables in-cylinder imaging with a clear view from the surface of the head down to the bottom of the piston bowl from approximately -90° to +90° ATDC with a single optical setup. For spray-visualization imaging through the cylinder wall window, two high-intensity discharge (HID) lamps replace the spatially integrated natural luminosity (SINL) detector shown in Figure 1.1.9a. These HIDs are directed through the piston window to illuminate the fuel jets with diffuse, white light.

High-speed NL imaging was accomplished for both camera views shown in Figure 1.1.9. For high-speed NL imaging through the cylinder window, simultaneous SINL measurements were made through the piston window. SINL is a measure of the time history of natural luminosity integrated across the view through the piston window; this is accomplished with a single-element, silicon photodetector (New Focus, Model 2031) [2]. The SINL detector can be configured to provide a linear signal level for all luminosity levels encountered in the current study.

Simulated exhaust gas recirculation

The SCORE has a simulated exhaust gas recirculation (EGR) system capable of supplying a mixture of air, N_2, and CO_2. The mixture is supplied by computer-controlled regulators based on model calculations to match the intake oxygen mole fraction as well as the constant-pressure specific heat capacity of the in-cylinder mixture at a given crank angle during the compression stroke in a metal engine utilizing real EGR. The mass of CO_2 is increased to compensate for the lack of H_2O in the simulated-EGR mixture.

Emissions Measurements

In addition to the optical diagnostics, the engine is equipped with exhaust-gas emissions analyzers including: 1) a heated flame-ionization detector (California Analytical Instruments,

Inc. (CAI) Model 600 HFID) for unburned hydrocarbons (HC); 2) a non-dispersive infra-red absorption and paramagnetic detector (CAI Model 602-P NDIR/O_2) for CO, CO_2, and O_2; 3) a heated chemiluminescence detector (CAI Model 600 HCLD) for NO_x; and 4) a smoke meter (AVL Model 415S). Because the SCORE is operated in a skip-fired mode where the injector is only fired once every 12 engine cycles, it is necessary to scale the emissions values to represent continuous-fired operation [3]. The scaled emissions concentrations are then converted into indicated specific emission values based on the known intake mass flow rates of air, simulated EGR, and fuel, as well as the measured gross indicated mean effective pressure (gIMEP) calculated from the cylinder-pressure data. The emissions results were not scaled to grams per brake hp-hr because the pumping and frictional work in the SCORE is not representative of those in a production engine.

Operating conditions

A 1200-rpm, light-load, 50% simulated-EGR operating condition was roughly identified using results from metal-engine testing performed at the Caterpillar Technical Center for a similar-sized engine. The exact parameters for the SCORE baseline operating condition were selected to minimize emissions of smoke, NO_x, HC, and CO resulting from single-parameter sweeps of injection timing and injection pressure. The baseline parameter values are provided in Table 1.1.3. A total of seven single- and two-parameter sweeps were performed to test the sensitivity of the baseline operating condition to changes of injection timing, injection pressure, equivalence ratio, simulated EGR, intake temperature, intake boost, and load. Details of the parameter limits for each sweep are provided in Table 1.1.4.

Table 1.1.3: Baseline Operating Condition

Load, gIMEP	4.82 bar
Boost	1.418 bar
IMT	42° C
simulated EGR	50%
Equivalence ratio	0.39
Max. fuel-injection pressure	142 MPa
SOI	-39.5° ATDC
Intake O_2 mole fraction	15.0 %
Intake CO_2 mole fraction	5.0 %
Simulated compression ratio	12.0:1
Speed	1200 rpm

From the results of the injection timing and injection pressure sweeps, a single injection timing and injection pressure combination was chosen as the basis of the two-parameter sweeps. Most of the two-parameter sweeps were chosen such that the second varied parameter was boost pressure. Boost was chosen as the second parameter in most sweeps to allow load, equivalence ratio, percent EGR, and intake manifold temperature (IMT) to be varied one at a time, independently of each other. However, diesel fuel is a two-stage ignition fuel and shows significant changes in cool-flame chemistry with increased cylinder pressure [4]. Therefore, a sweep of IMT and equivalence ratio was chosen to separate some of the effects of increased IMT from those of increased boost.

Table 1.1.4: Operating Conditions for the Parameter Sweeps

	Injection Timing [°ATDC]	Injection Pressure [MPa]	Φ [-]	EGR [%]	Intake Temp. [°C]	Load gIMEP [bar]	Boost [bar]
Baseline Condition	-39.5	142	0.39	50	42	4.82	1.418
Injection Timing Sweep	-69.5 to -29.5	142	0.39	46.6 to 50.2	42	4.82	1.418
Injection Pressure Sweep	-36.3 to -39.5	47, 95, 142	0.39	50	42	4.82	1.418
Equivalence Ratio and Boost Sweep	-39.5	142	0.24 to 0.58	50	42	4.82	2.060 to 1.132
EGR and Boost Sweep	-39.5	142	0.39	30 to 70	42	4.82	1.188 to 1.949
Intake Temperature and Boost Sweep	-39.5	142	0.39	50	32 to 62	4.82	1.373 to 1.508
Intake Temperature and Equivalence Ratio	-39.5	142	0.39 to 0.41	50	32 to 62	4.82	1.418
Load and Boost Sweep	-39.5	142	0.39	50	42	3.82 to 5.83	1.203 to 1.629

Injection timing sweep results

An injection-timing sweep at constant injection pressure was accomplished to determine the effects of spray targeting and in-cylinder fuel-air mixing on engine performance and emissions. The injection-timing limits were chosen to allow some time between the end of injection and the start of combustion for the most retarded case, and to contain the fuel within the piston bowl for the most advanced case. Spray-visualization of the SOI = -29.5° injection timing case showed that the fuel jets finish penetrating into the piston bowl at approximately -15° ATDC and apparent heat release rate (AHRR) data shows that the cool-flame combustion phase begins at approximately -10° ATDC; therefore this case is near the limit of retarding the injection timing toward TDC while still allowing time for the fuel to premix. Similarly, the SOI = -69.5° injection timing case represents the most advanced injection timing where the outer row of fuel jets is fully contained within the piston bowl; therefore, this represents the limit of advancing the injection timing without cylinder wall wetting. Figure 1.1.10 shows an individual image from each extreme injection timing condition. From these images it is clear that the liquid fuel impinges on the surfaces of the piston bowl, even at the most retarded injection timing studied. As shown in Figure 1.1.11, the in-cylinder temperatures over the injection timing are below the end boiling point of the fuel until after the end of injection for the baseline injection timing of SOI = -39.5°.

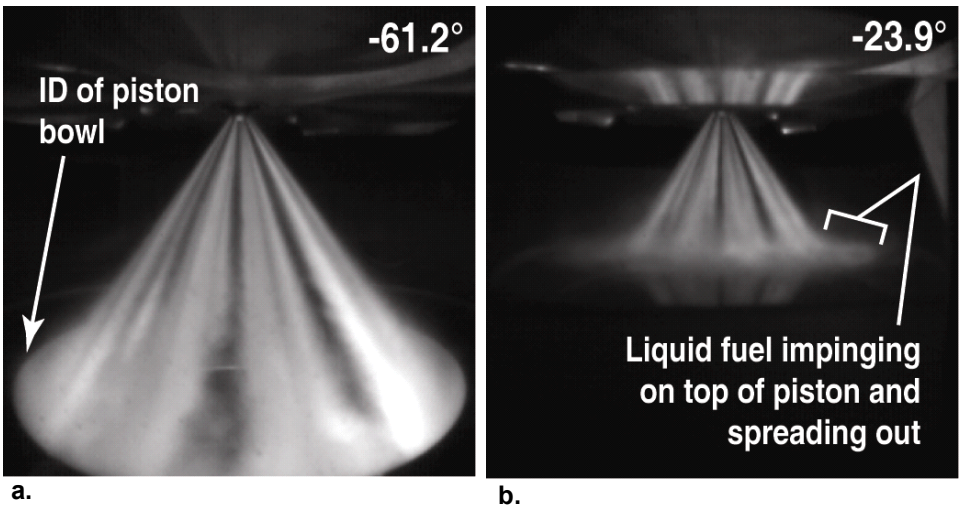

Figure 1.1.10. Spray visualization images through the cylinder window for two injection timings. a. SOI = -69.5°ATDC and b. SOI = -29.5° ATDC

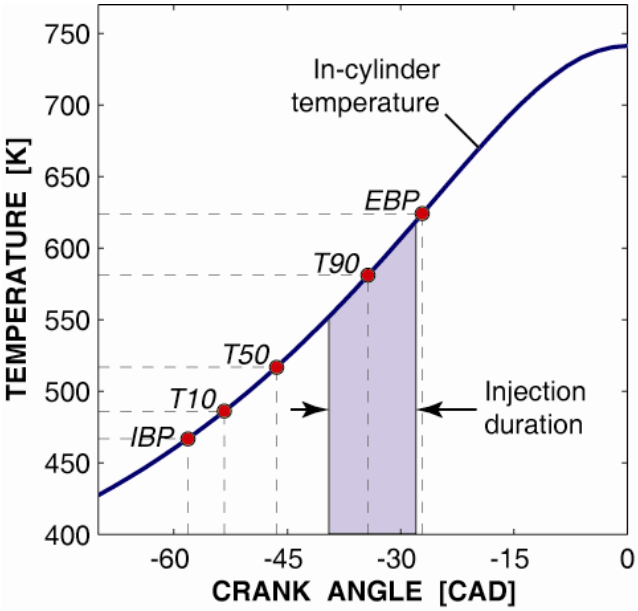

Figure 1.1.11. In-cylinder temperature as a function of crank angle for the baseline operating condition, including some fuel distillation points. Note that all of the fuel is injected into in-cylinder temperatures below the end boiling point of the fuel at this condition.

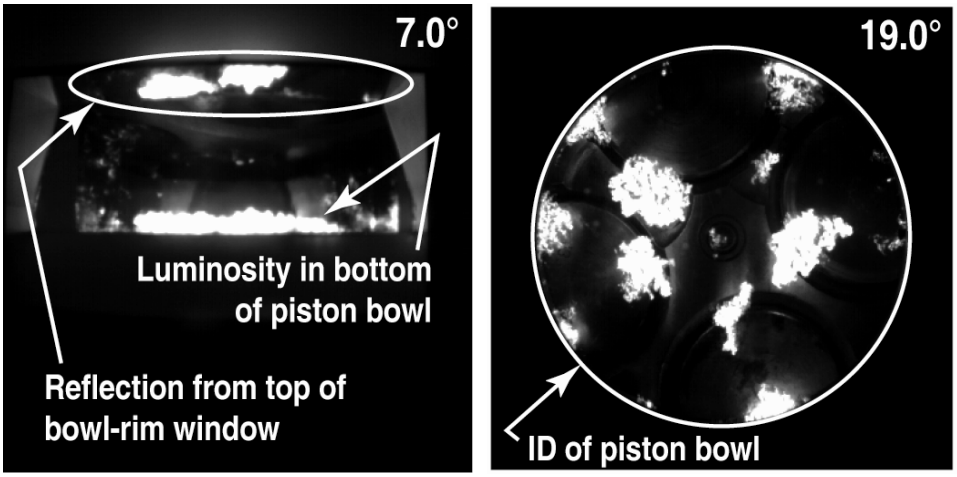

Figure 1.1.12. Natural luminosity images from the high-speed camera for an injection timing of SOI = -69.5°ATDC for both a. cylinder window view and b. piston window view. Pool fire activity is clearly visible in the selected images.

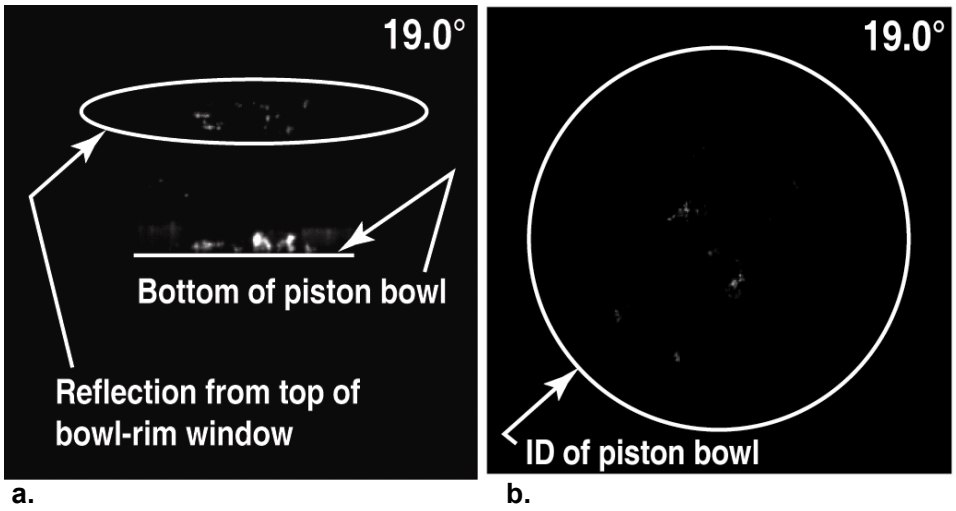

Figure 1.1.13. Natural luminosity images from the high-speed camera for an injection timing of SOI = -39.5°ATDC for both a. cylinder window view and b. piston window view.

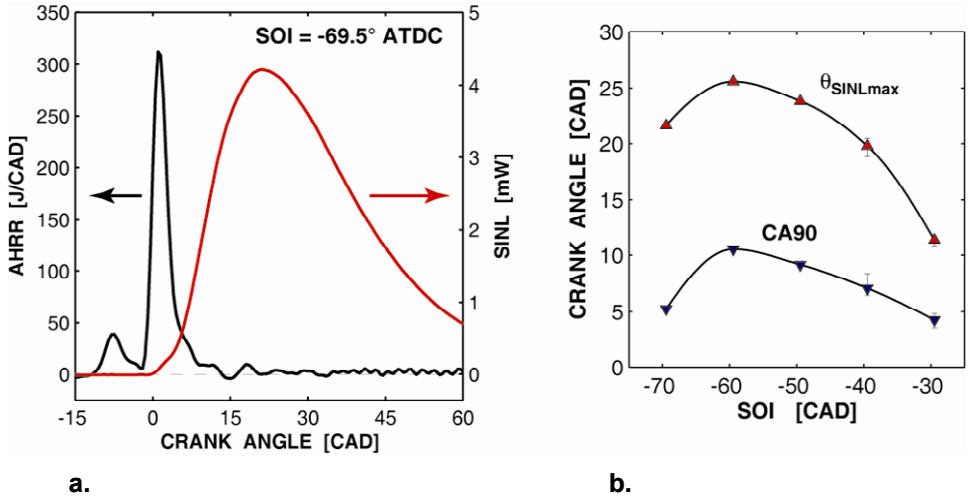

Figure 1.1.14. A. shows relative timing of apparent heat release for the SOI = -69.5°ATDC injection timing along with the spatially integrated natural luminosity (SINL) trace. This clearly shows that most of the intense luminosity from pool fire activity occurs after then end of significant heat release. B. shows the 90% heat release timing relative to the timing of peak SINL for all of the injection timing single-parameter sweep cases studied.

Figure 1.1.12 shows selected images from the natural luminosity movies collected for the SOI = -69.5° case. These images show the intense pool fire activity that results from the liquid fuel impingement on the surfaces of the piston during injection event. A similar set of selected images are shown in Figure 1.1.13 for the SOI = -39.5° case. Even this retarded injection timing case still shows pool fire activity. Comparison of the AHRR data with either the high speed NL movies or the SINL data shows that these pool fires occur after the end of significant AHRR. Figure 1.1.14a shows the AHRR trace overlaid with the SINL trace for the SOIa = -69.5° injection timing case. From this plot it can be observed that the natural luminosity does begin to increase in intensity around the time of peak heat release, but that the peak in SINL occurs after the end of significant heat release. And the intense natural luminosity from the pool fires observed in the high speed movies continues well into the expansion stroke. Figure 1.1.14b provides similar timing data for all of the injection timing sweep cases by comparing the CA90 (90% cumulative heat release timing) with the timing of the peak SINL signal for each case.

Figure 1.1.15 shows the importance of spray targeting on smoke and NO_x emissions for early direct-injection diesel low-temperature combustion. It was expected that engine-out emissions of smoke and NO_x would both continue to reduce towards a minimum level as injection timing was advanced to provide additional mixing time before the start of combustion. While this trend was observed when initially advancing injection timing earlier before TDC, the trend levels out and then reverses at the earliest injection timings studied. Spray visualization results show that these earlier injection timings resulted in liquid fuel impinging on the vertical wall of the piston bowl and NL movies showed that this resulted in increased pool fire activity.

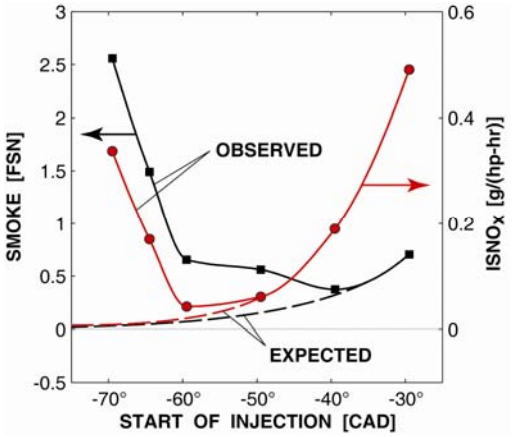

Figure 1.1.15. Smoke and indicated NO_x emissions for the injection timing single-parameter sweep showing the expected continued reduction in emissions levels with advanced timing compared with the observed increase in emissions as spray-bowl targeting changed at the most advanced timings.

Pool-fire effects on emissions

Figure 1.1.16 compares the emissions results with peak SINL levels for the five two-parameter sweeps. Again, the NL movies showed that the majority of the SINL signal results from the intense pool fires that result from the fuel films caused by jet impingement on the surfaces of the piston bowl. Figure 1.1.16a shows that engine-out smoke and NO_x levels rise steadily as the peak SINL value increases. This observation provides significant evidence to link these emissions to the diffusion combustion of the pool fires where rich equivalence ratios provide conditions necessary for soot production and near-stoichiometric conditions are also available to enhance thermal NO_x production.

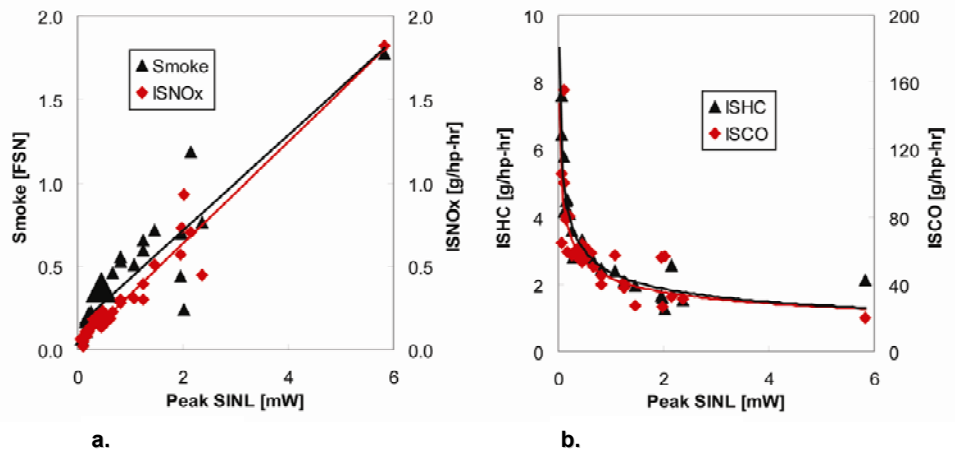

Figure 1.1.16. Peak SINL vs. emissions for the two-parameter sweeps. The baseline condition is marked by the larger symbols on each plot. NO_x and smoke emissions increase approximately linearly with increases in peak SINL. HC and CO emissions are relatively constant for peak SINL above 1 mW, but rise significantly as the peak SINL levels are reduced to near-zero levels.

Similarly Figure 1.1.16b shows how the HC and CO emissions trend with increased peak SINL. HC and CO emissions are very high for near-zero peak SINL values , but decrease rapidly as the pool-fire intensity begins to increase. They then reach a nearly steady level that does not change significantly as the peak SINL values continue to rise. These results provide further evidence of the detrimental effects that liquid-fuel impingement on emissions for early direct-injection diesel low-temperature combustion. Even if the primary heat release provides sufficient thermal energy to vaporize these fuel films, without the momentum available during the injection event, this fuel will be unable to sufficiently mix with in-cylinder oxygen to provide simultaneous low emissions of NO_x, soot, CO and HC. When all of the results of this study are combined, a clear picture emerges that shows liquid impingement and associated pool fires are highly detrimental to attempts to produce high-efficiency, low-emissions results from early direct injection of diesel fuel.

Summary / Conclusion

Low-temperature combustion of diesel fuel was studied in a heavy-duty, single-cylinder, optical engine employing a 15-hole, dual-row, narrow-included-angle nozzle (10 holes x 70° and 5 holes x 35°) with 103-µm-diameter orifices. Seven single- and two-parameter sweeps around a 4.82–bar gross indicated mean effective pressure baseline operating condition were performed to map the sensitivity of the combustion and emissions to variations in injection timing, injection pressure, equivalence ratio, simulated exhaust-gas recirculation, intake temperature, intake boost, and load.

Spray-visualization movies showed impingement of liquid fuel on the piston surface as a result of the low in-cylinder temperature at the time of injection. And high-speed NL movies revealed that intense pool-fire activity resulted from the vaporization and ignition of these fuel films created by liquid-fuel impingement within the piston bowl. Comparison of the emissions results with peak SINL values showed a strong correlation suggesting that the pool fires are a significant contributing factor to the overall emissions levels. Smoke and NO_x emissions were observed to rise steadily as pool-fire intensity increased. This can likely be explained by the fact that the resulting diffusion flame will provide both fuel-rich combustion zones needed for particulate matter production and high-temperature, near-stoichiometric zones needed for thermal NO_x production. HC and CO emissions were nearly constant provided that some level of pool-fire activity was observed, but these emissions showed a dramatic increase as the pool-fire activity was reduced to near-zero levels.

References

1. Mueller, C.J., Martin, G.C., Briggs, T.E., and Duffy, K.P., "An Experimental Investigation of In-Cylinder Processes under Dual-Injection Conditions in a DI Diesel Engine," *SAE Paper 2004-01-1843, SAE Trans., Vol. 113, Sect. 3,* 2004.
2. Upatnieks, A. and Mueller, C.J., "Clean, Controlled DI Diesel Combustion Using Dilute, Cool Charge Gas and a Short-Ignition- Delay, Oxygenated Fuel," *SAE Paper 2005-01-0363,* 2005.
3. Mueller, C.J. and Upatnieks, A., "Operational Characteristics of Oxygenate-Water Fuel Blends Studied in an Optical DI Diesel Engine With Simulated Exhaust Gas Recirculation," *SAE Paper 2007-01-2017, SAE Trans., Vol. 116, Sect. 4,* 2007.

4. Dec, J.E. and Sjoberg, M., "EGR and Intake Boost for Managing HCCI Low-Temperature Heat Release Over Wide Ranges of Engine Speed," *SAE Paper 2007-01-0051, SAE Trans., Vol. 116, Sect. 3,* 2007.

1.1.3: Variable Compression Ratio

Variable compression ratio (VCR) was investigated as a mechanism to control combustion phasing and enable operation at higher BMEP. In general, the compression ratio would be reduced as load increased (see Figure 1.1.17) to reduce compression temperatures and enable a sufficient ignition delay. However, reducing compression ratio will have a negative impact on the thermal efficiency. If the BSFC improvement with HCCI at higher engine loads more than offsets the negative impact of reduced compression ratio, then HCCI + VCR would potentially add value relative to conventional diesel combustion. The potential added value of the VCR engine will need to be weighed against the increased cost and complexity to determine if it would be production-viable. The performance and emissions of the VCR engine under HCCI conditions was tested and will be discussed in the section.

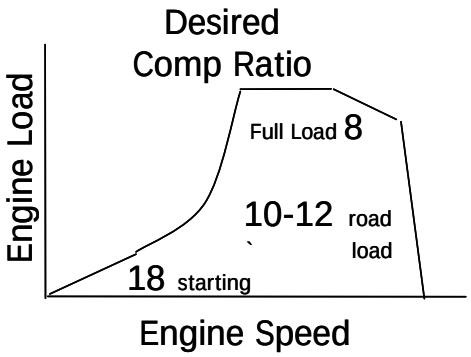

Figure 1.1.17. Rationale for Variable Compression Ratio (VCR) engine.

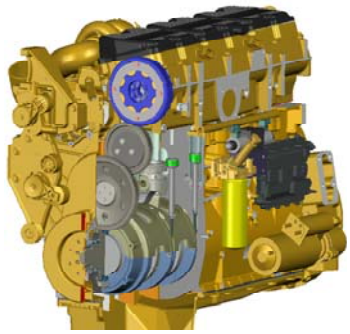

VCR
US Patent
Application
2006/0112911

Figure 1.1.18. Variable Compression Ratio (VCR) engine

A picture of the variable compression ratio (VCR) concept engine is shown in Figure 1.1.18. This engine was designed and built under the DOE Heavy Truck Clean Diesel Program. Testing was performed on the VCR HCCI engine in order to better understand the way in which the engine can be operated at both high and low loads. In addition to the VCR mechanism, this engine had an intake valve actuation (IVA) system that allowed for intake valve closure (IVC) to be delayed by as much as 100 crank degrees from the nominal value. Using the late intake valve

closing (LIVC) strategy reduced the effective compression ratio of the engine as the gas is now compressed during just a portion of the compression stroke.

With the ability to change compression ratio, each operating point for the engine can be optimized. An example of this optimized benefit of a VCR engine is shown below in Figure 1.1.19. When compared to a fixed 11:1 compression ratio baseline, the VCR engine could achieve a 1% BSFC advantage at 625 kPa BMEP by using a compression ratio of 12:1. The VCR engine could also achieve a 5% BSFC advantage by reducing compression ratio to 10:1 at 1000 kPa BMEP. The trend of increasing BSFC with increasing compression ratio seems counter intuitive. However, at the 1000 kPa BMEP condition, reducing the compression ratio retarded the combustion phasing to a more optimal timing. The improvement in fuel consumption due to combustion phasing was more significant than the loss of efficiency due to the reduced compression ratio.

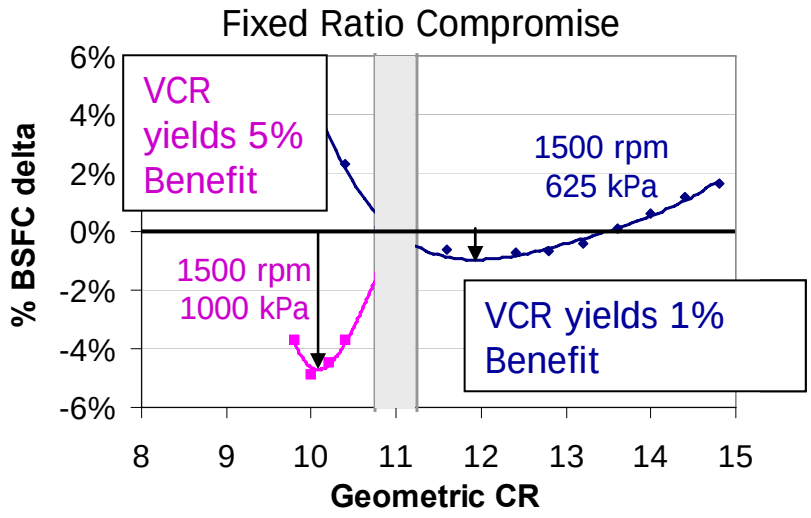

Figure 1.1.19. The benefit of using a VCR engine for optimizing compression ratio at operation between 625KPa BMEP and 100 kPa BMEP.

The results also included the detailed establishment of "operational limits" as shown in Figure 1.1.20. Specifically, the engine was run at all possible combinations of compression ratio, EGR fraction, combustion phasing, injection timing and intake valve actuation (IVA) that yielded a specific combustion phasing near top-dead center (TDC). Only certain combinations of those five parameters yielded an acceptable operating condition. Other combinations were deemed unacceptable for reasons including excessive pressure rise rates, overly rich air-fuel ratios, and excessive NOx emissions. Additionally, there were times when a combination could not be run because a subsystem such as the VCR mechanism or IVA system ran out of authority (hit its maximum or minimum value) and thus no longer had the ability to influence combustion phasing.

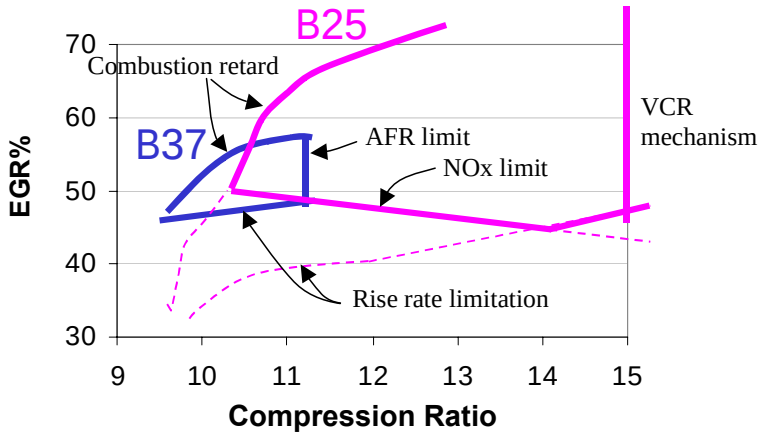

Figure 1.1.20. Operating limits for 1500 rpm 25% load (B25) and 37% load (B37) operating conditions for 2° ADTC phasing

As the load increases, the size of the operating range decreases, and also shifts toward a lower compression ratio. For a fixed compression ratio, the load range of the engine would be limited to the loads that have overlapping operating regions. For a variable compression ratio engine, the range of loads could be increased.

The ability of the VCR mechanism to extend load capability of an HCCI engine was also demonstrated in Figure 1.1.21. Smoke emissions at selected points were superimposed on air-fuel ratio contours. The contour corresponding to an air-fuel ratio of 16 has been highlighted in the figure. An air-fuel ratio of 16 might represent the practical air-fuel ratio limit of the engine. Below this air-fuel ratio the smoke number is very high (≥ 1), and at higher air-fuel ratios the smoke number is more acceptable (<0.5). Thus, the figure illustrates how dropping the compression ratio extends this air-fuel ratio limit to higher load. For a variable compression ratio engine, the high load compression ratio can be dropped with little consequences for the lower load conditions. For a non-VCR engine, the downside of dropping the compression ratio is that at lower loads, problems with white smoke, cold startability, HC emissions and BSFC would be encountered.

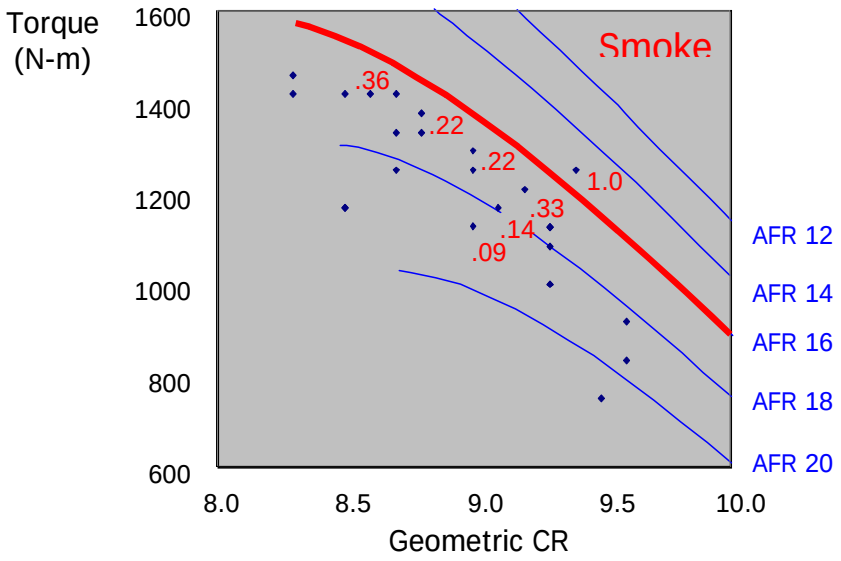

Figure 1.1.21. Smoke emissions and air-fuel ratio contours as a function of compression ratio and engine load

The functionality of the VCR engine for HCCI combustion was verified, and the ability to extend load and optimize fuel consumption were demonstrated. However, the fuel consumption levels of this engine were higher than expected. Subsequent inspection of the engine after testing was complete revealed a bearing failure in the VCR mechanism that likely contributed to higher friction. This bearing failure and analysis of the proposed solution is included in section 2.2:.

1.1.4: Multi-cylinder PCCI Results

A series of tests were conducted to assess the performance of part-load PCCI combustion on a C15 engine with a production-like engine configuration. The intent of the tests was to define the upper and lower engine load limits, identify key parameters affecting emissions, and determine control system requirements. The C15 engine was configured with compression ratio, piston bowl shape, fuel system, and air system configuration typical of a production on-highway truck engine. Key control parameters, such as injection timing, injection pressure, and EGR rate were varied over a range of speeds and loads to determine the acceptable operating range of PCCI combustion for a typical engine configuration and to assess the emissions and engine performance. The knowledge gained from these tests will be used to identify control system requirements for a multi-mode combustion strategy that uses PCCI at part-load.

Test Set-up

The test engine was configured to be representative of a typical on-highway truck production engine. The base engine configuration was a MY2007 C15 on-highway truck engine, however some modifications were made. The Cat Engine Technologies Ultimate Flow Cylinder Head was used to enable the use of a Cat CR350 common rail fuel injection system. A common rail fuel system was preferred because it allowed a greater range of early injection timings than the cam-based MEUI production injector. The air system configuration of the C15 test engine is shown in Figure 1.1.22. The configuration is typical of a MY2007 C15 engine with low pressure exhaust recirculation, known as Clean Gas Induction (CGI). However, a second CGI cooler was added to allow for the high CGI flow rates necessary for PCCI operation. The MY2007 production turbochargers were used. The fuel injector nozzles, piston bowl shape and compression rate were typical of a production engine. The injector nozzles were 6 holes x .214mm x 130°. A “concept” piston bowl shape, similar to the MY2007 production piston bowl, with a resulting compression ratio of 16.8, was used.

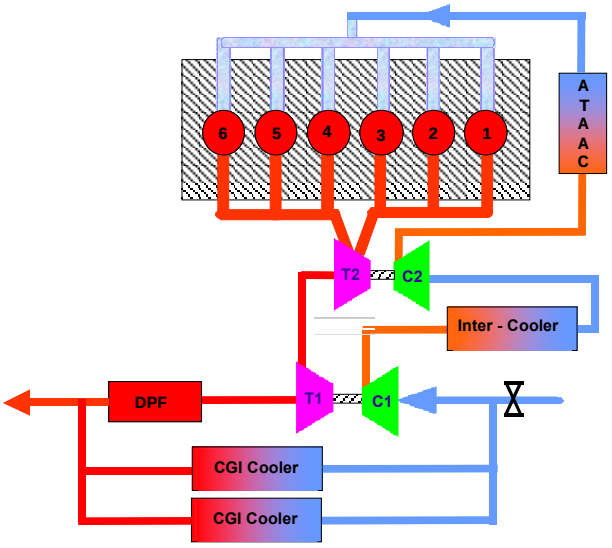

Figure 1.1.22. Air System Schematic

Three sets of PCCI combustion tests will be discussed below. A series of tests to study the effects of fuel injection timing and CGI level on combustion and emissions was conducted at 25% load. A second series of tests examined the effect of load change and defined the factors

that limit the achievable engine load with PCCI combustion. Finally, a third series of tests examined the effect of injection pressure on PCCI combustion and emissions.

Effect of Injection Timing and CGI level

A series of timing sweep tests were conducted at 1200, 1500 and 1800 rpm, and 25% load. For purposes of this discussion only the results at 1200 rpm will be analyzed. The results at the other speeds were similar. Three timing sweeps were performed at 1200 rpm, 450 kPa BMEP. A sweep was performed at roughly 55% CGI, one at roughly 59% CGI, and a sweep was performed trying to hold combustion phasing around 3 deg BTDC.

The NOx emissions for the injection timing sweeps are shown in Figure 1.1.23. Figure 1.1.23b also includes the NOx emissions of a CGI sweep at constant injection timing of 21 deg BTDC. The results show that NOx is a strong function of CGI and a function of combustion phasing. The sensitivity of NOx emissions to combustion phasing appears to decrease as the CGI level increases, as can be seen by comparing the 55% CGI results to the 59% CGI results in Figure 1.1.23.

In Figure 1.1.23a, NOx emissions begin to decrease at advanced injection timings. This NOx reduction corresponds to the combustion phasing retard that occurs at advanced timings. In addition to retarded combustion phasing, another possible NOx reduction mechanism is the additional dilution of portions of the fuel-air mixture to low equivalence ratios. Since the ignition delay is longer at advanced injection timings, allowing for increased mixing, this is more likely to occur. At this point, the relative contribution of each of the mechanisms is unknown. Additional analysis will be needed to determine if a premixed, low-equivalence ratio mixture was a significant factor in this case.

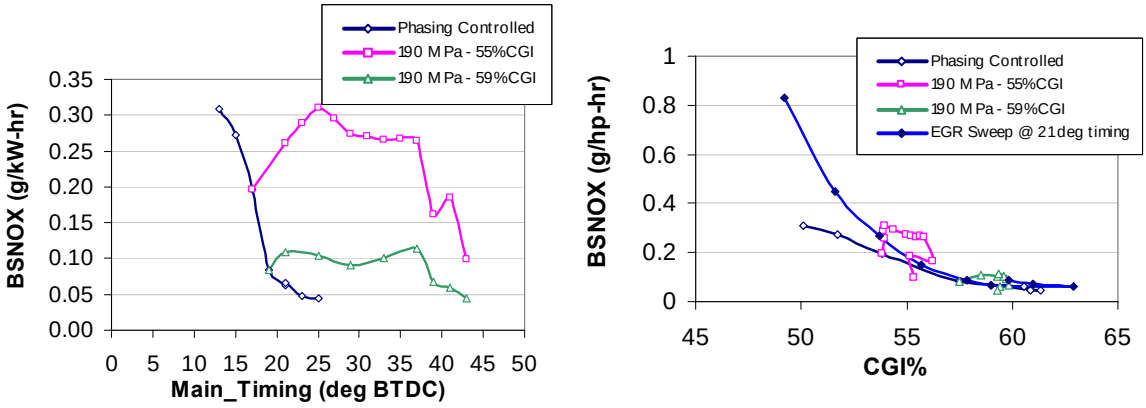

Figure 1.1.23. (a) NOx emissions for fuel injection timing sweeps at 1200 rpm, 450 kPa BMEP (190 MPa injection pressure) ; (b) NOx emissions plotted versus CGI %, also includes results from a CGI sweep at constant fuel injection timing.

Control of CGI flow is critical to the control on NOx emissions. The sensitivity of NOx emissions to changes in CGI flow is demonstrated in Figure 1.1.23. A variation between 55% and 59% CGI caused NOx to vary nearly 0.2 g/hp-hr. At 2010 on-highway emissions levels, this level of variation would be unacceptable. Precise control of CGI flow rate based on intake

manifold gas composition or emissions feedback would be required. If EGR was used, even distribution between cylinders would also be critical to controlling NOx emissions

The AVL smoke emissions for the injection timing sweeps are shown in Figure 1.1.24. The smoke emissions rapidly decreased as timing is advanced. This was consistent with increased premixing of the air-fuel mixture prior to ignition. The very low soot levels would indicate a significant portion of the fuel-air mixture was at an equivalence ratio less than 2. As CGI level was increased, more advanced timing was required to achieve the necessary level of premixing to achieve a low soot condition.

At the most advanced timings, the AVL smoke rapidly increased. The timing of the increase was not influenced by the CGI level, but CGI level did influence the magnitude of the soot increase. Unlike with retarded timings, the lower CGI level resulted in the largest soot increase. The rapid soot emissions increase at the advanced timings also corresponds to injection timings that would have resulted in liquid fuel reaching the piston surface. While direct evidence of liquid fuel impingement – soot emissions relationship was not available in this case; the results are consistent with findings from the Sandia Optical Engine discussed earlier. The results from the Sandia Optical Engine showed a relationship between soot formation and the existence of pool fires caused by liquid fuel impingement on the piston surface.

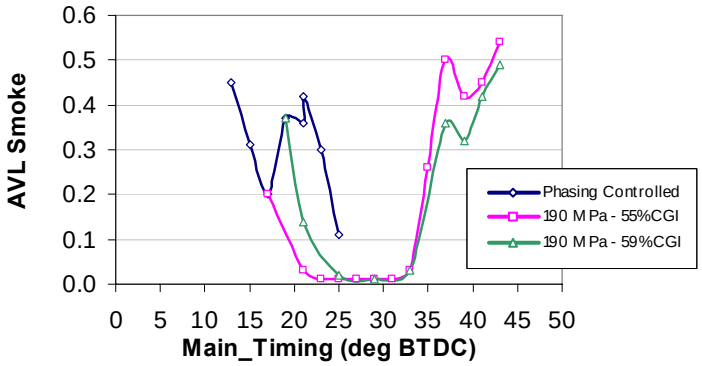

Figure 1.1.24. AVL smoke emissions for fuel injection timing sweeps at 1200 rpm, 450 kPa BMEP (190 MPa injection pressure)

The HC emission results from the injection timing sweeps are shown in Figure 1.1.25. In general, the HC emissions were controlled within acceptable limits, except for the most advanced injection timings. Similar to the AVL smoke emissions in Figure 1.1.24, the HC emissions increased rapidly starting around 37 deg BTDC. This increase corresponded with the injection timing that would result in a portion of the fuel spray being injected over the piston bowl and into the squish region.

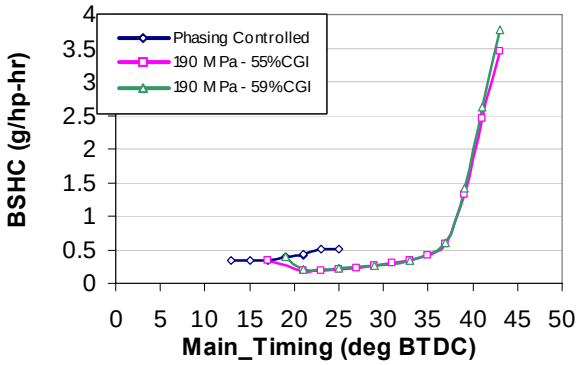

Figure 1.1.25. HC emissions for fuel injection timing sweeps at 1200 rpm, 450 kPa BMEP (190 MPa injection pressure)

The results from Figure 1.1.24 and Figure 1.1.25, define the ideal fuel injection window. At the conditions tested, starting fuel injection prior to 37 deg BTDC, resulted in high HC emissions and would likely result in fuel impingement on the cylinder liner. Regardless of aftertreatment or other technologies that may mitigate the high HC emissions, the issues related to fuel reaching the liner, such as piston ring deposits and oil dilution, dictate that the fuel spray remains in the piston bowl. Thus fuel injection should start no earlier that 37 deg BTDC for the hardware configuration tested. Achieving low soot emissions required starting injection early enough to achieve adequate mixing. Under the conditions tested, fuel injection needed to start prior to 27 deg BTDC. One would expect the injection window to change as the engine operating conditions change. The influence of in-cylinder temperature and density on the spray vaporization and penetration, the influence of equivalence ratio on required mixing time, and the influence of in-cylinder temperature and CGI level on the ignition delay will affect the ideal injection window.

Effect of Engine Load

A series of engine load sweeps using PCCI combustion were conducted at 1200 rpm. The resulting NOx and AVL smoke emissions versus engine load are shown in Figure 1.1.26. The baseline BMEP sweep was aimed at keeping NOx below 0.3 g/hp-hr and AVL smoke below 0.5. The NOx and AVL smoke emissions for conventional high-CGI diesel combustion in a similarly configured engine are also shown in Figure 1.1.26. A second set of PCCI combustion results that have NOx nearly equal to the conventional diesel combustion data is also shown.

As load increased, the CGI rate needed to be decreased to maintain an acceptable equivalence ratio. As can be seen in Figure 1.1.26, the compromise between CGI rate for NOx control and adequate equivalence ratio for low smoke resulted in a gradual increase in NOx and smoke up to about 850 kPa BMEP. Above 850 kPa BMEP, it was not possible to maintain NOx at or below 0.3 g/hp-hr and also maintain AVL smoke below 0.5. However, when compared to conventional diesel combustion at equal NOx emissions, PCCI combustion produced lower soot emissions up to 920 kPa BMEP.

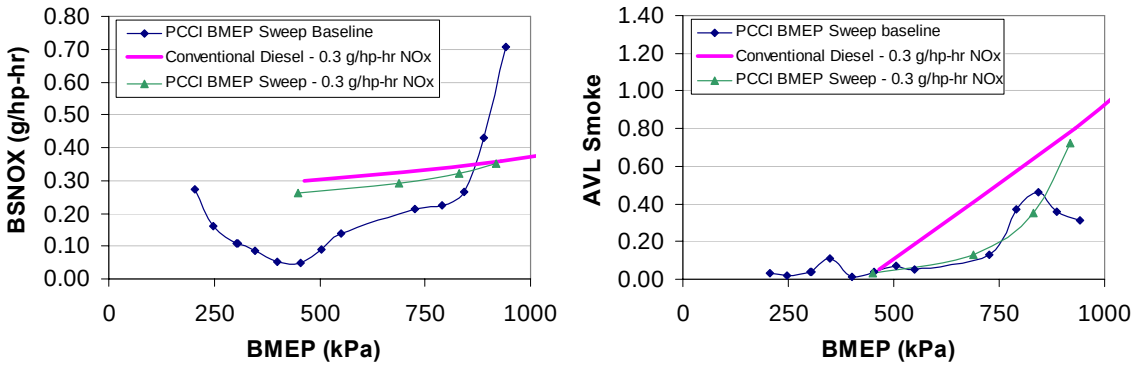

Figure 1.1.26. NOx and AVL smoke emissions for BMEP sweeps at 1200 rpm using PCCI combustion at low NOx (baseline), using conventional diesel combustion with approximately 0.3 g/hp-hr NOx and using PCCI combustion with approximately 0.3 g/hp-hr NOx

The BSFC results for the engine load sweeps are shown in Figure 1.1.27. At equal, NOx the BSFC of PCCI combustion is lower than conventional diesel up to about 850 kPa BMEP. Increased boost associated with increased engine load caused the combustion phasing to advance as load increased. Above 750 kPa BMEP, the advancing combustion phasing caused BSFC to increase with higher load. Another issue associated with advanced combustion phasing is high cylinder pressure rise rate, as shown in Figure 1.1.28. High rate of cylinder pressure rise rate is a source of combustion noise, as well as potential driver of enhanced in-cylinder heat transfer. During HCCI combustion development, a 5 Mpa/deg cylinder pressure rise rate threshold was used. This threshold was exceeded at 725 kPa BMEP. However, the appropriateness of this development threshold with the current engine configuration and under the conditions tested needs to be validated.

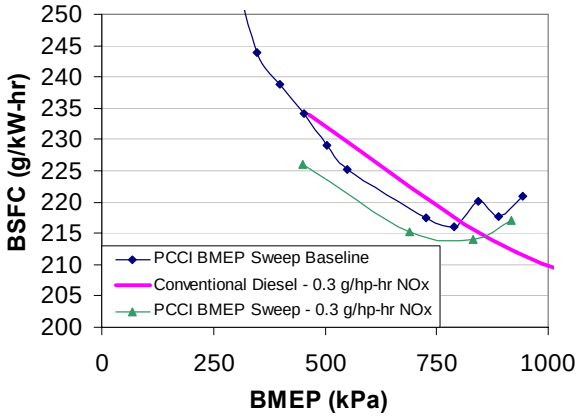

Figure 1.1.27. BSFC vs BMEP comparison at 1200 rpm for PCCI combustion at low NOx (baseline), conventional diesel combustion with approximately 0.3 g/hp-hr NOx and PCCI combustion with approximately 0.3 g/hp-hr NOx.

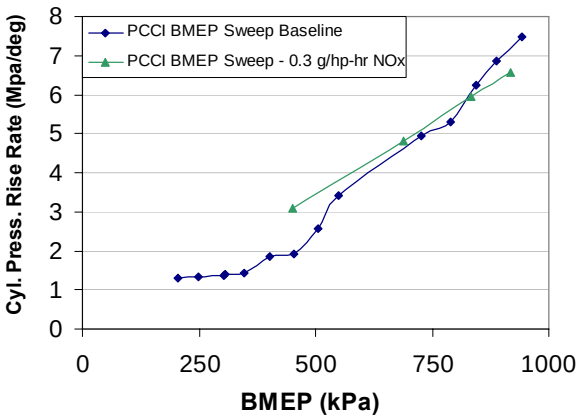

Figure 1.1.28. Cylinder pressure rise rates as a function of BMEP at 1200 rpm

Summary of Multi-Cylinder PCCI Testing

The above results show that PCCI combustion has equal or lower NOx, lower AVL smoke and better BSFC than conventional diesel combustion up to about 750 kPa BMEP for the engine configuration tested. However, cylinder pressure rise rate would likely limit the PCCI operation range to 725 kPa BMEP. The PCCI operating range and benefit versus conventional diesel combustion are limited by the ability to control combustion phasing. Therefore an additional method to control combustion phasing would be desirable. A method to retard combustion phasing without relying on diluent (CGI or EGR) or on reducing cylinder trapped mass (IVA) would reduce the CGI required for NOx control, reduce smoke emissions by increasing mixing time, reduce cylinder pressure rise rates, improve BSFC and thus increase load range.

1.1.5: Conclusions on feasibility of diesel HCCI

This project has shown that diesel HCCI or PCCI combustion can deliver lower fuel consumption with low soot and NOx emissions over a limited operating range. A limited fuel injection window constrains the quantity of fuel that can be combusted in a premixed fashion. Achieving sufficient ignition delay with diesel fuel such that combustion can be phased late enough to control the cylinder pressure rise rate is also a limiting factor.

To achieve HCCI combustion the following criteria need to be met:

- Injecting fuel into the squish region should be avoided. This results in excessive HC and CO emissions.
- Fuel must be injected late enough to avoid liquid fuel impingement on the piston, or any other surface.
- Fuel injection must end prior to the start of combustion, thus fuel injection must occur within the ignition delay time.
- Combustion phasing must be retarded enough such that the cylinder pressure rise rate limit is not exceeded.

To achieve full load, the allowable fuel injection window must be increased by injecting fuel earlier without liquid fuel impingement and increasing the ignition delay. To avoid liquid fuel impingement, higher gas temperature and density would be preferred, but to lengthen ignition

delay a lower temperature would be desired. Cylinder temperature can be lowered by reducing effective compression ratio, but this also reduces the gas density. Thus the boiling point and ignition properties of diesel fuel limit significantly limit the operating range of HCCI or PCCI combustion.

The boiling range window for a typical diesel fuel is shown in Figure 1.1.29. The boiling range window represents the earliest fuel injection can begin to avoid liquid fuel impingement. With diesel fuel, the fuel injection window starts around 40 - 50BTDC. As shown in previous section of this report, this limited the amount of fuel that could be premixed prior to ignition, and thus limited the engine to about 1/3 load.

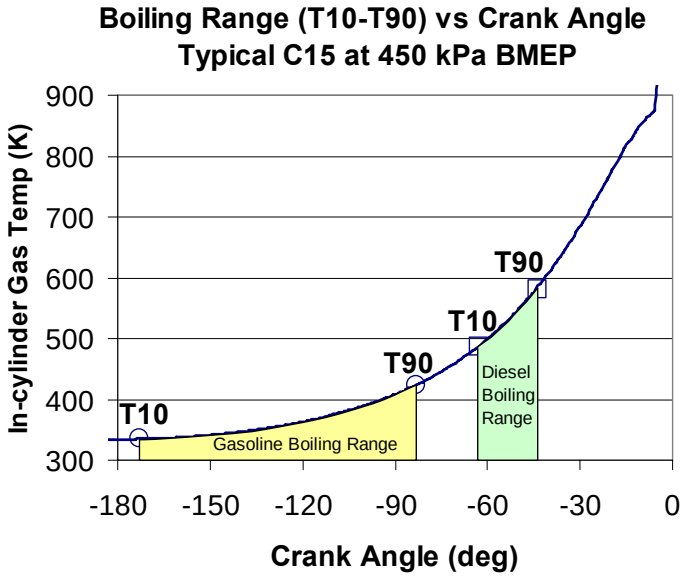

Figure 1.1.29. The boiling range windows for gasoline and diesel fuel for a typical C15 at 450kPa BMEP

The figure above also shows the boiling range window for gasoline. The more volatile fuel would significantly increase the fuel injection window. Subsequently, the longer ignition delay of a low cetane number fuel, such as gasoline, would also increase the fuel injection window. The impact of fuel properties on HCCI combustion will be discussed in the next section.

1.2: Fuel Property Effects

The fuel vaporization and ignition processes play a significant and critical role in HCCI combustion. In addition to the in-cylinder thermodynamic conditions, these two processes can be greatly impacted by the properties of the fuel. This section summarizes the work, built upon collaboration between Caterpillar and ExxonMobil, to better understand the impact of fuel property effects on HCCI combustion.

1.2.1: Diesel Fuel Property Effects

To investigate the impact of diesel fuel properties, particularly cetane number, on HCCI combustion, a series of diesel fuels, shown in Table 1.2.1 were tested. The experiments were focused on evaluating the effect of cetane number on HCCI load capability and emissions.

Table 1.2.1. Test Fuel Properties

Property	D14 (Typical US Cetane)	D18	D17	D19B	D16 (Low Cetane)
Cetane Number	45.9	34.8	30.9	29.6	< 19.6
Derived Cetane Number (IQT)	45.2	36.1	31.3	33.2	24.2
Boiling Range (T_{10}-T_{90}), ° F	416 - 587	427 - 608	428 - 607	435 - 576	441 - 596
Sulfur, mg/kg	11	21	19	13	23
Total Aromatics, mass%	34.8	44.2	47.7	29.4	53.7
Isoparaffins, mass%	8.3	26.3	33.8	55.5	44.2

One of the most important results obtained from this testing was the characterization of the minimum and maximum load ranges for each fuel. The maximum load was constrained by peak cylinder pressure and/or peak cylinder pressure rise rate. The minimum load was limited by combustion stability (ie misfire). These results are shown in Figure 1.2.1. In general, the lower cetane fuels enable a higher maximum load, but also a higher minimum load. The results with the higher geometric compression ratio utilized Intake Valve Actuation (IVA) to control the effective compression ratio to be similar to the lower geometric compression ratio results. Thus, the load range with the 14:1 compression ratio did not substantially change from the previous 12:1 compression ratio results which did not use any IVA.

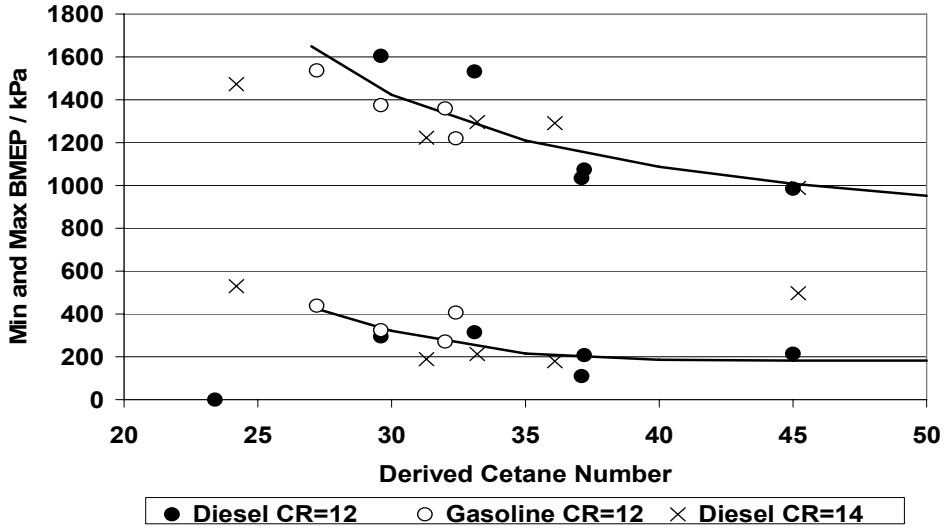

Figure 1.2.1. Load Ranges for Each Fuel at 1200 rpm

The ignition characteristic of a fuel, as measured by cetane number, has a very significant effect on combustion phasing. A lower cetane number fuel has a longer ignition delay, and thus has a more retarded combustion phasing, or allows less EGR to be used to obtain a given combustion phasing. This behavior can be seen in Figure 1.2.2, which compares the EGR required to achieve a constant combustion phasing with the D14 and D16 fuels. The lower cetane fuel (D16) required significantly less EGR to achieve the same combustion phasing. Utilizing less EGR would be beneficial for extending load range and lowering fuel consumption. However, as shown in Figure 1.2.3, utilizing less EGR caused a significant increase in NOx emissions. Maintaining the EGR level, holds the NOx at a low level, but results in retarded combustion phasing. Above 50% EGR, the combustion with D16 is retarded beyond the desired combustion stability limit.

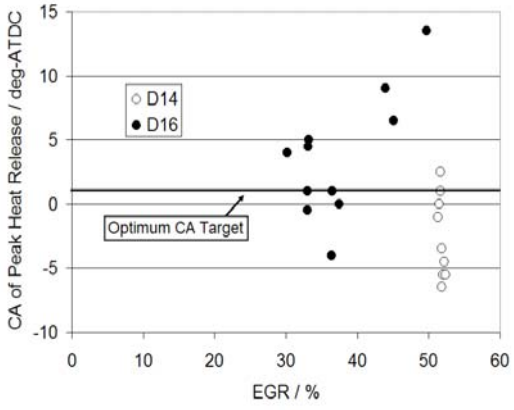

Figure 1.2.2. Combustion phasing results as a function of fuel and EGR

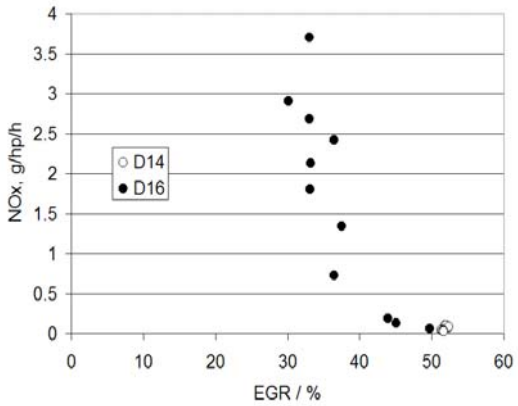

Figure 1.2.3. NOx emissions as a function of fuel and EGR

Lowering the cetane number of the fuel caused a longer ignition delay and decreased the dependence on EGR for controlling combustion phasing. However, without a significant increase in the level of air-fuel premixing, the NOx emissions were still dependent on the EGR level. As shown earlier with the results from the Sandia Optical Research Engine (see Figure 1.1.11) and the multi-cylinder PCCI engine (see Figure 1.1.29), the boiling point range of typical US diesel fuel constrained the fuel injection window and limited the amount of premixing that is possible. Thus, with diesel fuel, the benefits of lowering the cetane number were limited.

1.2.2: Gasoline and Diesel Blending

The work described in the previous section, demonstrated the impact of a fuel's ignition characteristic (ie. cetane number) on the load capability and EGR requirements for HCCI combustion. Blending gasoline fuel into diesel fuel was viewed as a practical method of formulating a lower cetane fuel for engine experiments. Since the cetane number of gasoline fuel is significantly lower than that of diesel fuel, blending gasoline and diesel fuels increases ignition delay. In addition, the high volatility of gasoline fuel could help fuel air mixing. Thus PCCI combustion could be achieved at a relatively lower EGR level.

This study evaluated combustion features, fuel consumption, emissions, and operating ranges of three different fuels (diesel, gasoline, and GD25) at various engine loads at 1200rpm. Properties of the fuels were summarized in Table 1.2.2. Analysis was performed at 40% EGR at 1200rpm to examine the characteristics of engine performance of the three fuels at PCCI and/or close to PCCI combustion conditions. Three fuels were designed to cover the range of cetane number resulting from blending commonly available transportation fuels (diesel and gasoline).

Table 1.2.2. Fuel properties of diesel, gasoline and a gasoline-diesel fuel blend (GD25)

Parameter		Diesel	GD25	Gasoline
Density at 60°F (g/cm^3)		0.8319	0.7829	0.7511
Derived Cetane number		43.2	25.8	14.9
Vapor pressure (psi at 100°F)		0.1	7.08	9.36
Distillation (°F)	10%	408	142	125
	50%	504	280	217
	90%	595	536	304
Sulfur (mg/kg)		3	11	29
Carbon fraction (% m/m)		86.61	87.97	87.17
Hydrogen fraction (% m/m)		13.39	13.03	12.83

Gasoline fuel gave significantly shorter combustion duration and longer ignition delay than the other two fuels (diesel and GD25) as shown in Figure 1.2.4. The significantly longer ignition delay was believed to lead to shorter combustion duration by allowing for greater fuel-air mixing prior to ignition. This shorter duration increased the work conversion efficiency, which led to higher thermal efficiency at the lower load conditions as shown in Figure 1.2.5(a). However, at 55% load, as shown in Figure 1.2.5(b), the peak thermal efficiency was equal to diesel fuel and slightly lower than GD25. The long ignition delay with gasoline resulted in significantly higher pressure-rise-rate at equal start-of-combustion as shown in Figure 1.2.6. Consequently, gasoline fuel required a more retarded start of combustion timing, which negated the effect of the shorter combustion duration. The longer ignition delay and higher cylinder pressure-rise-rate of gasoline fuel limited the allowable injection timing to a very narrow range (2 crank angle degrees) and eventually prevented the engine from running lower load conditions. At 25% load, higher intake air temperature and/or higher boost pressure were required to keep the engine combustion stable with gasoline fuel.

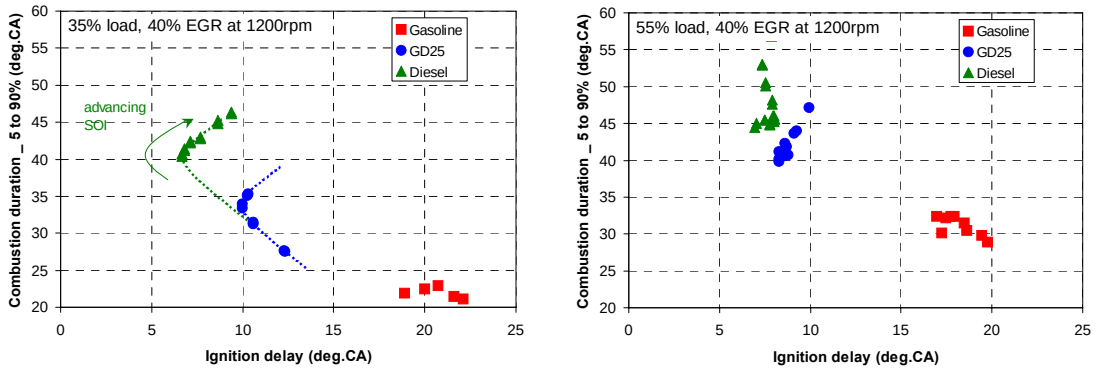

(a) 35% load (b) 55% load

Figure 1.2.4. Combustion duration comparison of diesel, gasoline, and GD25 at 1200rpm

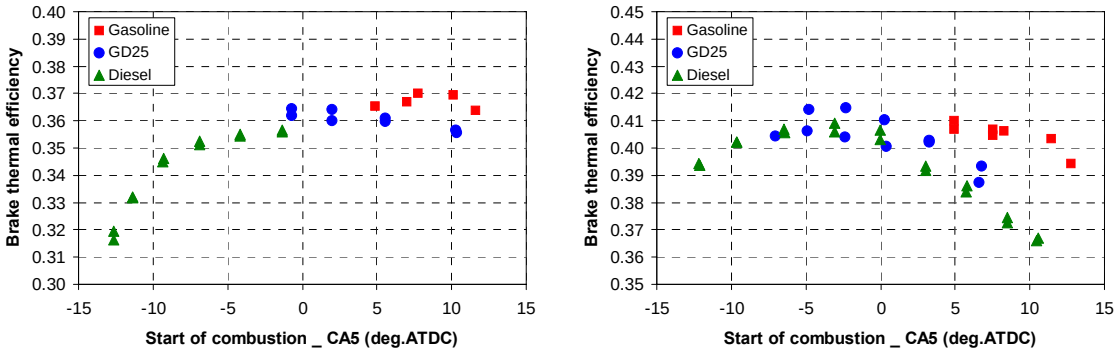

(a) 35% load (b) 55% load

Figure 1.2.5. Brake thermal efficiency comparison of gasoline, GD25, and diesel fuels at 1200rpm

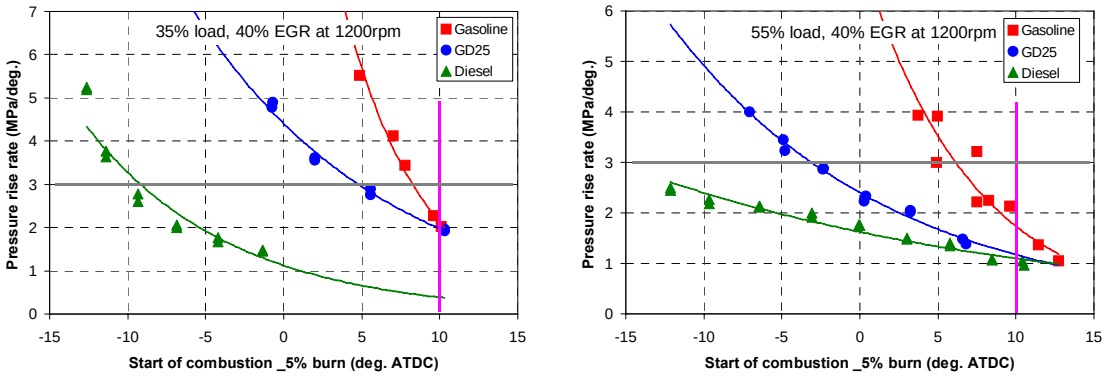

(a) 35% load (b) 55% load

Figure 1.2.6. Operating range of Gasoline, GD25, and diesel fuels limited by pressure-rise-rate and combustion stability at 1200rpm (40% EGR)

The most significant advantage of GD25 and gasoline fuels was lower soot emissions than diesel fuel. A comparison of the soot emissions with the three fuels at 55% load is shown in Figure 1.2.7. GD25 fuel could achieve lower level of soot emissions and higher thermal efficiency than diesel fuel. Gasoline fuel could achieve lower soot emission at equal thermal efficiency with diesel fuel, but at a lower efficiency than GD25.

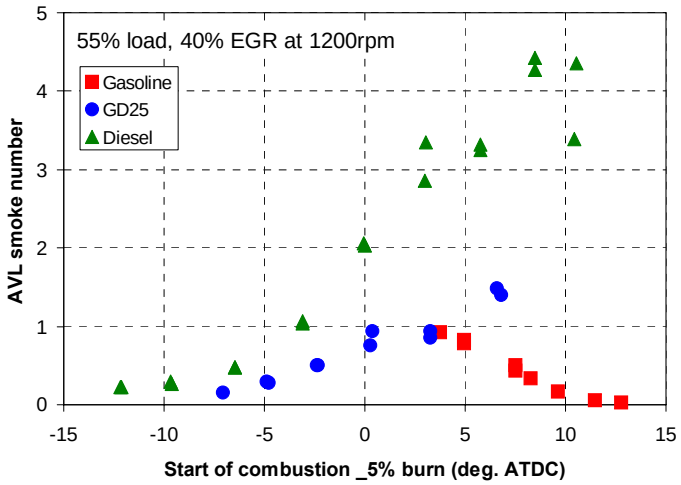

Figure 1.2.7. Soot emissions trends with respect to start-of-combustion at 55% load and 1200rpm with 40% EGR.

Using fuels with a lower cetane number and higher volatility than diesel fuel has shown some potential to increase thermal efficiency and reduce engine-out soot emissions. However, the increased cylinder pressure rise rate associated with these fuels limits their benefits and utilization. This project only focused on single fuel injection strategies. Alternative injection strategies could yield better control of the initial combustion rate and lower cylinder pressure rise rates. Given the potential efficiency and emissions benefits, continued research of combustion with lower cetane number and the effects of fuel distillation are recommended.

1.3: Non-HCCI Combustion Development

Several technologies developed in support of HCCI combustion development were also useful for non-premixed combustion. The high-pressure piezo-electric fuel injector, enabled development of extended lift-off combustion. The development of this technology will be discussed in Section 1.3.1:. Fuel injector nozzle orifice geometry was considered as parameter that could be used to impact fuel-air mixing for HCCI. The reverse-tapered geometry that was explored has a greater impact of non-premixed combustion. A summary of the work on this concept is discussed in Section 1.3.2:.

1.3.1: Extended Flame Lift-off Combustion

The concept of enhancing air-entrainment prior to the lift-off length in diesel fuel jet combustion has the potential to dramatically reduce soot emissions. When used in conjunction with exhaust gas recirculation (EGR), both NOx and smoke could potentially be kept at low levels to minimize the use of diesel exhaust aftertreatment with good thermal efficiency. This concept extends from the work at Sandia National Labs where diesel fuel jets burning with conventional diffusion flame structure were shown to exhibit little or no smoke formation when mixing is enhanced prior to the location where combustion begins (termed the lift-off length) (Picket and Siebers, Combust. Flame 138:114-135). This is accomplished by manipulating the lift-off and mixing parameters (such as increasing injection pressure, decreasing injector hole diameter, and lowering ambient temperature) so that enough air is entrained into the jet to cause combustion to occur only in regions where the equivalence ratio is less than 2, where soot formation is avoided. A general characteristic of this type of combustion is that the lift-off length of the fuel jet occurs substantially downstream from the liquid penetration length, and the term “lifted flame” has been used to describe this type of enhanced air-entrainment combustion. The potential for low engine-out emissions with good performance make this an attractive technology.

The current program focuses on making this type of combustion feasible in a high-load engine operating condition. The main obstacle to achieving sootless, lifted flame combustion at high load is the practical limits on the combustion system parameters. For example, in-cylinder temperature is limited by the required charge heat removal and the practical minimum compression ratio to achieve good cold start performance. The injection pressure is limited by current hardware availability and mechanical durability concerns. Orifice diameter is limited because a large amount of fuel is required for high load operation with reasonable injection durations, thus requiring a large flow area. If small holes are used, there has to be a large number of holes with little hole-to-hole separation. As the hole-to-hole separation angles become smaller, combustion plume interaction becomes significant causing high smoke values and removing the gains of the small orifice diameter. Therefore, this program focuses on using the highest available injection pressure in conjunction with small holes that are spaced optimally to reduce the plume interaction, thus achieving the objective of low soot combustion.

A significant portion of this work involved exploring the parameters involved with lifted flame combustion and identifying the limits of this concept for practical application. While some of these limits are well characterized and easily understood, such as the amount of fuel required, the emissions requirements, etc., other limits were poorly understood, such as the limitations on plume spacing to maintain sootless combustion and the requirements of the transient in-cylinder conditions. Significant results in engine tests, optical engine test, optical spray testing, and

simulation have been obtained to understand the fundamental mechanism for the increase in emissions as plumes become closely spaced. Understanding this interaction is important in recognizing the limitations in the lifted flame concept and designing combustion systems to utilize enhanced air entrainment prior to liftoff.

Methodology

This methodology consisted of development of a lifted flame combustion system. This development has undergone three main phases:

1. Test and development of potential lifted flame development concepts.
2. Determining the fundamental limitations on sootless, lifted flame combustion to design better combustion systems
3. Application of fundamental limitations to feasibility analysis and design of sootless combustion system

In phase 1, a C15 single cylinder engine was used in conjunction with the Caterpillar in-house computational fluid dynamics (CFD) code called xFD. Phase 2 utilized the facilities in the Caterpillar spray and combustion visualization laboratory and the Sandia optical engine along with CFD simulation and engine test to better define our knowledge of the limitations on lifted flame combustion. Most of these facilities have been defined previously or need little explanation. However, the High Temperature Pressure Vessel in the spray and combustion visualization laboratory will be described as it represents a relatively new and unique tool in combustion system development.

Heated and combusting spray tests were conducted at the High Temperature Pressure Vessel facility at Caterpillar's spray and combustion visualization laboratory. This facility is shown schematically in Figure 1.3.1. The system is a continuous flow chamber, where high temperature gas is heated as it flows through the chamber. The inlet gases are currently capable of being mixtures of air and nitrogen, so 0 to 21% oxygen with the balance nitrogen can be achieved. This enables testing of evaporating sprays or combusting sprays. The gases enter the vessel on the bottom, flow upwards through two 15 kW electric heating elements, and then into the test section. The combustion is visible through three optical windows across from and perpendicular to the injector axis. After the spray, the gases exit through the five separate tube-in-tube heat exchangers, where they are cooled to an intermediate temperature before heading to two larger heat exchangers for cooling to ambient temperature. The maximum gas pressure of the vessel is 15 MPa, while the maximum temperature capability of the heating system is 1000 K. Thus, top dead-center conditions can be maintained in the vessel, and the combustion can occur under conditions similar to those in the cylinder of a heavy duty diesel engine. The walls of the vessel are shielded from the high temperature environment by an inner liner with its own windows, and this liner is heated and insulated. Thus, the outer pressure-bearing walls and windows are not exposed to the high temperature gases. Filtered light emission measurements were used to characterize the combustion events, looking specifically at the combustion radical species' light emission as a marker for the flame and the broadband light emission as a soot indicator.

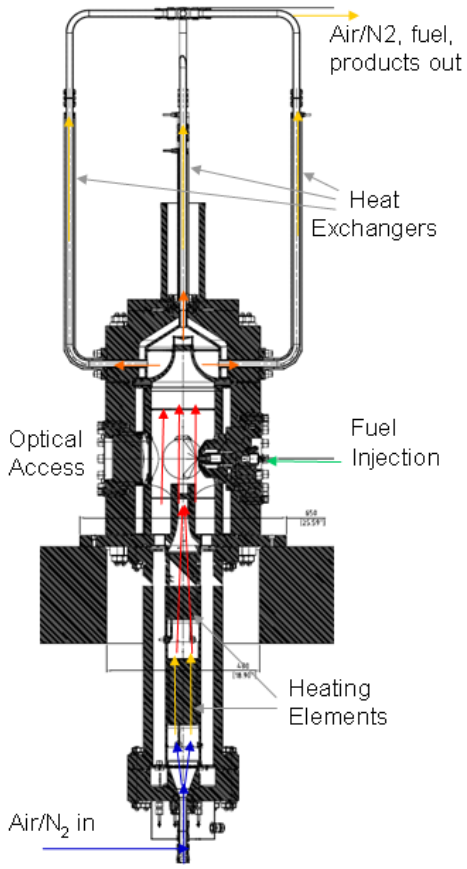

Figure 1.3.1. Schematic of HTPV spray and combustion test facility.

Test and Development of Potential Lifted Flame Development Concepts
Initial testing of potential lifted flame combustion systems showed the promise of the lifted flame combustion concept as shown in the low emissions levels from the C15 single cylinder engine in the 6 hole data at 50% load in Figure 1.3.2. However, the small orifices used in this combustion system were not capable of achieving high loads in the C15 engine. When a system capable of achieving higher loads using a larger number of orifices was tested, results were less promising as shown in the emissions increase of the 14-hole nozzle data shown in Figure 1.3.2.

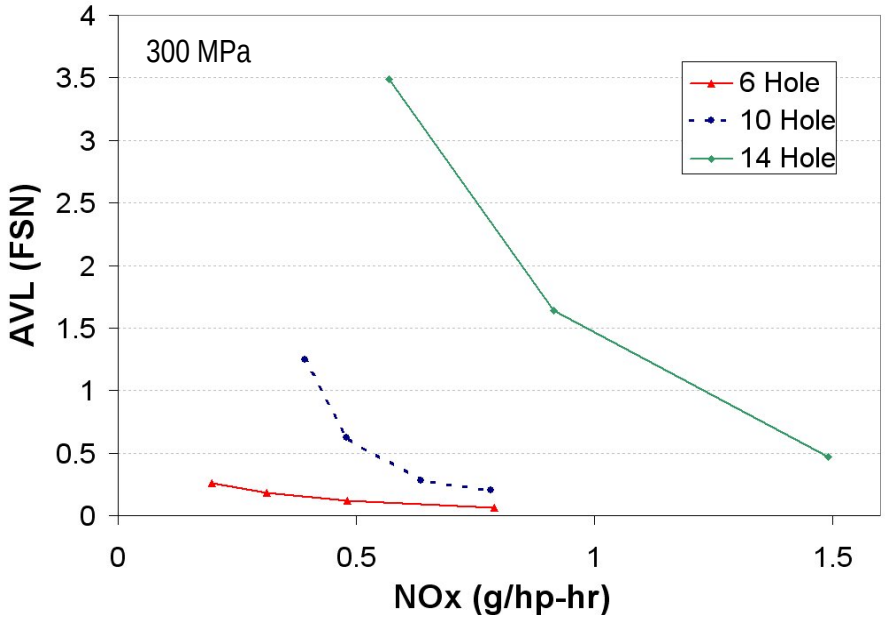

Figure 1.3.2. Effect of increasing number of spray jets on engine emissions.

This data showed that there was a significant effect of the number of orifices on the combustion and emissions performance. Two concurrent development paths were then undertaken. One path was to attempt to iterate the combustion system design to minimize the effects of plume interaction using our current knowledge. At the same time, it was acknowledged that this dramatic increase in emissions was not well understood, and that a research program was required to understand this phenomenon and develop a system that could avoid this dramatic increase.

The next step in the iterative development of the combustion system was to use multiple rows of orifices to increase plume spacing to attempt to increase jet spacing and hopefully avoid the interaction effects. An empirical phenomenological spray and combustion model along with CFD analysis were used to develop the orifice spacing and bowl shape of the combustion system. Sample results of this CFD evaluation are shown in Figure 1.3.3. As can be seen, the variations of the bowl shape were used to split the upper and lower spray to prevent spray interaction. A variety of bowl shapes were tried in simulation, which then lead to a set of two bowls for testing. One bowl had a 'W' shape providing a separation of the two jets by essentially producing a bowl profile for each row of jets, while the second bowl had a traditional bowl shape with no separation between the two jets. Overall, the CFD showed poor ability to predict a liftoff length near the expected value, exposing a weakness of these simulations to accurately predict liftoff length. Caterpillar is continuing to look into the fundamental phenomena and prediction of liftoff in a separate program with Purdue University.

In addition, a variety of nozzle iterations varying number of orifices and the included angle of the two rows were procured as well. During single cylinder engine test, these bowl-nozzle combinations showed improved results over the 14-orifice tests above. However, the emissions

still fell short of the benefits observed for the 6-hole lifted flame nozzle. This indicates that while these multi-row nozzles have potential to incrementally reduce plume interaction and could show additional benefit from further optimization, the interaction is still a significant issue, and that further understanding of the mechanism for this plume interaction must be obtained.

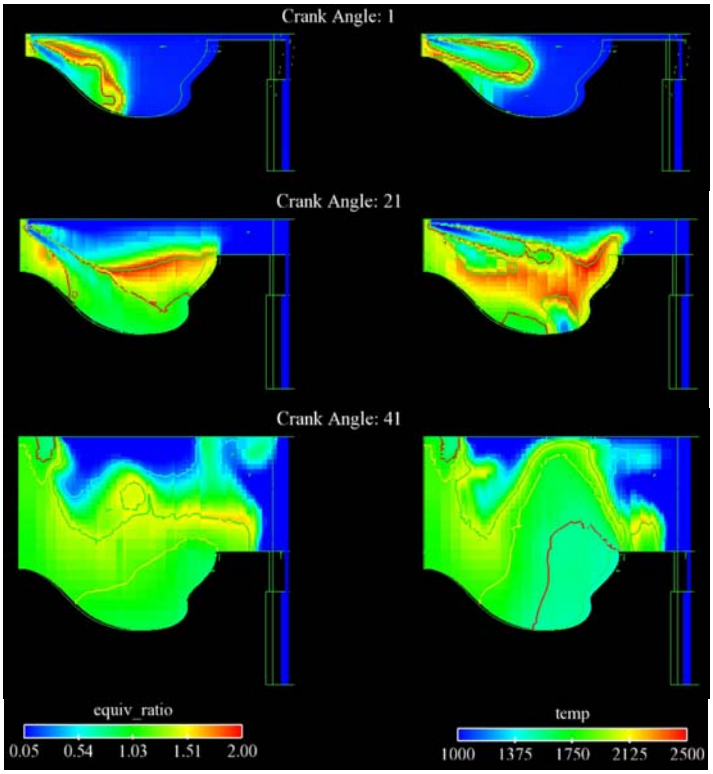

Figure 1.3.3. Equivalence ratio and temperature for bowl 1 with the 16 hole injector tip in the plane of the lower (left) and upper (right) nozzles according to xFD predictions.

The Fundamental Limitations on Sootless, Lifted Flame Combustion

In order to identify the mechanism for this plume interaction, a research program was carried out. This program consists of using testing and accompanying 3D CFD analysis to fully understand and model the phenomenon causing the emissions increase. The following scenarios represent processes that could be the cause of this plume interaction behavior:

- The air entrainment of each individual spray could be altered, with each plume having worse mixing because the neighboring plumes compete over the limited air to entrain.
- The overall spray momentum and penetration could be altered, in that as the jets become closer, the surrounding air flow field is altered significantly from that of an individual jet, possibly causing the jets to penetrate less which would affect the overall mixing behavior in the cylinder. This macroscopic flow effect could cause a reduction in late-cycle mixing due to the bulk flow in the cylinder.
- The neighboring jets could alter the flame characteristics and reduce the liftoff length of each jet and thus reduce the mixing prior to the liftoff length even if air entrainment is unaffected.

- The increased heat release rate due to faster fuel injection could cause an increase in the in-cylinder temperature field, leading to liftoff length retraction because liftoff length gets shorter at higher temperatures.
- Flame interaction of the neighboring plumes once the flames reach the piston bowl. The flames would then essentially collide with each other, and the air surrounding each plume would be combustion products of the neighboring plumes rather than fresh air to cool and oxidize each respective combustion zone.

Tests were performed to attempt to isolate the impact of each of these scenarios on the emissions increase of jet spacing in the Caterpillar spray and combustion and the Sandia optical engine.

Cold Spray tests were performed on a set of nozzles, looking for the possibility that the neighboring jets adversely affect the air entrainment or penetration of the jets. Overall, these tests showed that there was no effect of plume spacing on the air entrainment or jet penetration even for the case of an 18-orifice nozzle. This result agrees with other work (e.g. SAE 2010-01-0342) that has shown air entrainment and bulk spray motion are not affected by neighboring jets. Thus, these tests indicate that the source of the increased emissions of small jet spacing is likely not due to the neighboring jets causing a change in the air entrainment or bulk spray motion of each individual jet.

Combusting spray testing of nozzles having 6, 7, 8, 9, 10, and 14 holes have been carried out to look for the effect of jet spacing on liftoff length. This data provides important guidance to the plume spacing limit for lifted flame nozzles. That data shows that as the number of jets increased, there is a threshold plume spacing in terms of liftoff length behavior. Above this value, the liftoff is shortened, and below this value, the jets burn relatively unperturbed by the neighboring jets. Thus, the practical limit for plume spacing without significantly decreasing size of the regime where conditions produce sootless combustion was identified. It is also instructive to note that previous spray tests showed no significant change in the bulk spray behavior as the plume spacing decreased. Thus, the observed difference in liftoff behavior is a combustion effect as opposed to a spray effect. One possible cause for this behavior includes a change in the fluid dynamics in the region between the jets. Current theories of liftoff often suggest that the fluid strain extinguishes ignition prior to the liftoff length. The neighboring jets could be impacting the fluid strain in the region between the jets, allowing combustion to occur in that region. Another likely cause could be heat transfer from the neighboring jet, which heats the mixture and accelerates the reactions.

Optical engine tests have also been performed to look at the feasibility of sootless lifted flame combustion. These tests have illustrated the following characteristics:

- Re-entrainment of recirculated burned gases into the spray limits how late in the expansion stroke soot-free combustion can be sustained. The data show that recirculation is caused by jet-jet and jet-wall interactions that lead to shorter lift-off lengths, richer mixtures at the liftoff length, larger soot luminosity signals, and elevated engine-out smoke. This has a large impact on the maximum duration of injection, because increasing the amount of fuel injected after recirculation occurs can increase the engine-out smoke by approximately an order of magnitude. Simulation was carried out the investigate the recirculation risks in metal engine applications and how the recirculation

can be affected by design parameters such as orifice size, number of orifices, and injection pressure.

- Sustained soot-free combustion over the entire DOI is possible under in-cylinder conditions that are achievable in a heavy-duty engine. Further optimization and enhanced understanding of the trade-offs with this type of combustion strategy is likely to produce further benefits. Nevertheless, soot-free in-cylinder combustion using injector tips that have adequate flow capacity to enable high-load operation remains an elusive goal.

Feasiblity Analysis of Sootless, Lifted Flame Combustion

Based on the understanding of sootless lifted flame combustion gained from optical engine tests, metal engine tests, spray combustion tests, and computational fluid dynamics simulations reported above , some of the fundamental limits and specifications for lifted flame combustion have been identified. These limits are defined from the phenomena laid out above and involve maintaining the liftoff length above the threshold required for sootless combustion throughout the duration of injection. These limits have been used to determine the feasibility of this concept across Caterpillar's engine platforms, identifying the best fit for this concept.

Conclusions

- Sootless lifted flame combustion has been demonstrated in spray vessels and optical engines as a possibility for heavy duty engines.
- Understanding the effects of plume interactions was necessary to accurately identify the parameters where sootless combustion is achievable.
- Optical engine test, cold spray test, combusting spray test, engine test, and simulation were all required to determine the limitations on sootless combustion.
- The updated knowledge of the limitations of sootless combustion have been applied to a feasibility analysis of Caterpillar's engine platform, and a demonstration program is underway for the platform deemed most suitable for this technology.

1.3.2: K-factor Nozzle Geometry Effects

Injector nozzles drilled with reducing diameter of the orifice in the direction of fuel flow, as shown in Figure 1.3.4, are known as K-factor nozzles. K-factor nozzles have been shown to reduce cavitation within the orifice and may help reduce engine out smoke emissions. However reductions in smoke have not been observed consistently with multi-cylinder engine testing and the mechanisms through which k-factor nozzles affect in-cylinder combustion are not fully understood. The current work is focused on applying optical diagnostics to observe the injection, vaporization and combustion of injectors with varying levels of k-factor nozzle orifice taper in the high temperature and pressure vessel (HTPV) facility to determine what changes that k-factor can provide to free jet reactions. These results will be utilized to help understand engine testing data.

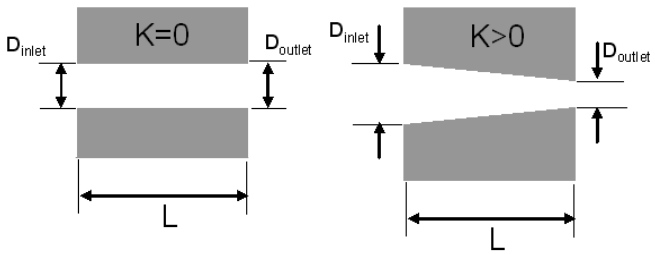

Figure 1.3.4. Schematic of K-factor orifice geometry.

A matrix of four nozzles were tested including two different orifice steady flow rates and two k-factor levels, k=0 and k=2.5, for each steady flow. Tests were performed at three fuel rail pressures, and varying ambient pressures and temperatures within the HTPV. Pressures of 60 and 120 bar were selected and then the temperature was swept between near the ignition limit to 900K (the current upper temperature of the HTPV).

In addition to the optical diagnostics, the injector nozzles were tested for their resistance to cavitation on an injection rate bench. This testing was performed by measuring changes in delivered fuel quantity with changes in rail pressure from 100 to 300 MPa and back pressure from 1 to 18MPa. The results of the rate bench tests confirmed that the current k-factor nozzles are significantly more resistant to cavitation.

Experimental Facility
These tests were conducted at the High Temperature Pressure Vessel facility at Caterpillar's spray visualization laboratory. This facility was previously described in the extended flame liftoff combustion section.

Optical Setup
Four optical diagnostics were utilized to study the combustion of the K-factor nozzles. The optical setup consisted of three cameras and two narrow-band dichroic mirrors such that three of the diagnostics were performed simultaneously. The first diagnostic is a time-integrated image of OH^* chemiluminescence. The second diagnostic is a high imaging of excited state CH* chemiluminescence near 430 nm with a Phantom V12 camera; though the captured light often includes a significant amounts of soot luminosity. These images can be interpreted as an indicator of the location of significant concentrations of CH* and/or hot soot, and thus show the location of the high temperature heat release. The third simultaneous diagnostic is the high speed imaging of natural luminosity with no spectral filtering at 40,000 frames per second with a Phantom V710 camera. This imaging collects the total luminosity from the flame, which was dominated by soot luminosity. The fourth diagnostic also utilizes the Phantom V710 camera along with a high-repetition rate copper vapor laser to image the liquid fuel penetration of the diesel jets. This requires that a 511nm narrow-band interference filter be placed in front of the camera to block most of the broad-band soot luminosity and therefore can not be imaged simultaneously with the natural luminosity (soot) imaging. The CH^* and OH^* imaging are repeated during the spray visualization imaging and can provide a direct comparison to verify repeatability of the combustion events.

Results and Discussion

Figure 1.3.5 shows time averaged results for the four diagnostics applied to study the k-factor nozzles. As stated above, the first three images of each row result from optically filtering various wavelength ranges of the natural combustion luminosity to observe the location of OH^*, CH^*, and soot within the reacting jets. The right image in each row is the result of Mie scattering laser light off of the liquid fuel jets. The lines drawn in each image are the result of post processing the images to measure the lift-off or liquid length of each plume. From both the images and the numerical results, the lift-off length are observed to significantly increase with increasing injection pressure while the liquid length remain nearly constant.

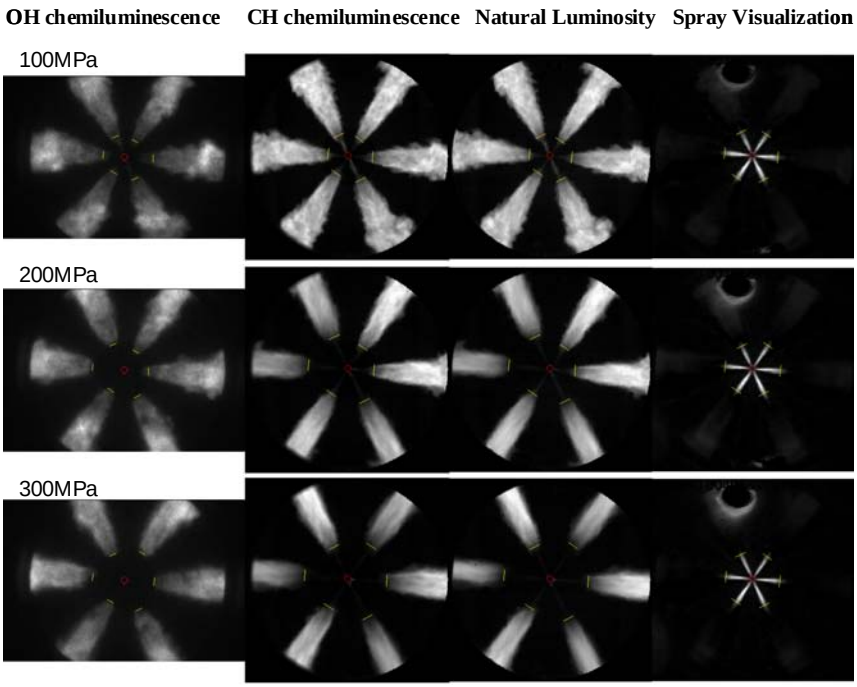

Figure 1.3.5. Time-averaged lift-off length, soot location and liquid length images for ambient conditions of 120bar and 865K with varying injection pressures.

Figure 1.3.6 shows the changes in lift-off length as defined from the OH chemiluminescence imaging of the four k-factor nozzles tested. The lift-off length for the lower steady flow nozzles, see in Figure 1.3.6.A, was increased for the k=2.5 nozzle. The lift-off length for the higher steady flow nozzles (2.8 kg/min), shown in Figure 1.3.6.B also show increase in the lift-off length for the k=2.5 nozzles at the lower temperatures. However, this increase in the lift-off length tends to disappear at the higher temperatures.

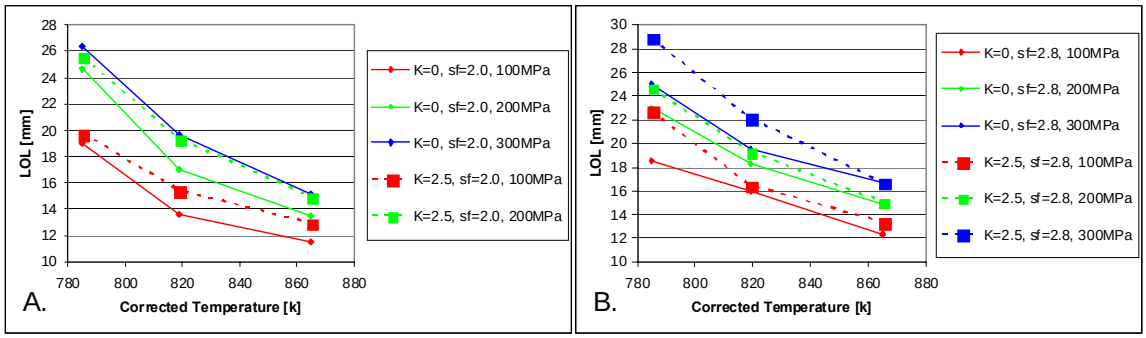

Figure 1.3.6. Variation of lift-off length as measured by OH chemiluminescence for all four k-factor nozzles tested at 120 bar ambient pressure. A. lift-off length of 2.0 kg/min steady flow nozzles. B. lift off length of 2.8 kg/min steady flow nozzles.

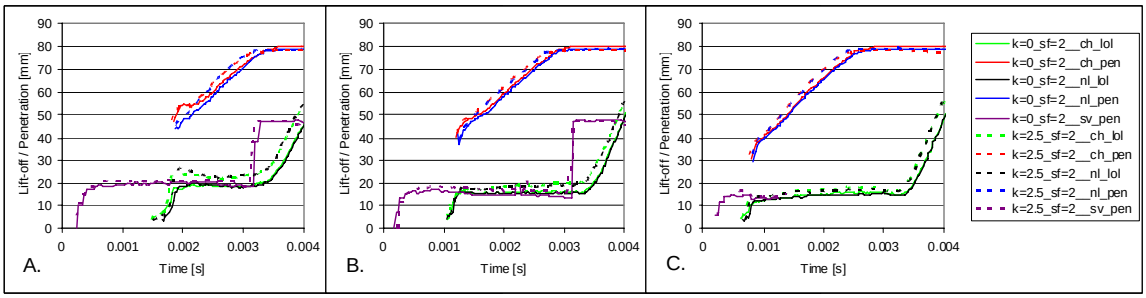

Figure 1.3.7 Time resolved liquid spray penetration, lift-off length, and combusting plume penetrations for the 2.0 kg/min steady flow nozzles at 100MPa injection pressure. The ambient conditions in the HTPV are 120bar for all three plots and the temperature was A. 785K, B. 819K, and C. 865K .

In addition to the time averaged images and OH lift-off length data, the individual high speed movies are processed for time-resolved values of liquid penetration, soot inception length and plume penetration. Figure 1.3.7 shows the results for the varying ambient temperature of the vessel on the injection, vaporization and combustion of the k=0 and k=2.5 nozzles with 2.0 kg/min steady flow. Each plot gives time on the x-axis from the start of current signal to the injector control solenoid. The y-axis displays the liquid penetration (labeled sv_pen), the lift-off length as determined from either the CH chemiluminescence (labeled ch_lol) or the NL movies (labeled nl_lol), or the penetration of the plume tip as determined from either the CH chemiluminescence (labeled ch_pen) or the NL movies (labeled nl_pen). All presented lengths have been scaled for distance along each jet based on geometry of the fuel sprays. The window size limits the viewable penetration of the jets to approximately 79 mm from the injector tip. The liquid length measurements show that the k=2.5 nozzle produces a slightly increased liquid length. The time-resolved measurements of the combustion are by CH chemiluminescence (dominated by soot luminosity in the current study) and NL imaging. After the start of combustion the lift-off length shows a quasi-steady value during the remainder of the injection event. The measurements show that the k=2.5 nozzle maintains a slightly longer quasi-steady lift-off length throughout the combustion event. After the end of injection, the NL lift-off length trace shows how the remaining soot propagates away from the injector. Finally, time-resolved

measurements of combusting plume penetration from CH chemiluminescence and NL imaging show the k=2.5 nozzle has a slightly faster penetration that the k=0 nozzle.

Figure 1.3.8 shows time resolved measurements of the reacting fuel jets at locations 32, 48, 64 mm downstream of the nozzle with red, green and blue lines, respectively. The k=2.5 nozzle shows a wider cone angle at 32mm location, and then narrows more quickly as the combustion propagates downstream. These cone angle measurements are accomplished on the highly sooting, natural luminosity high-speed movies. Therefore it is not possible to say that the location of the flame front changed, instead, it is only possible to say that the soot concentrations and/or temperatures are showing a different spatial pattern.

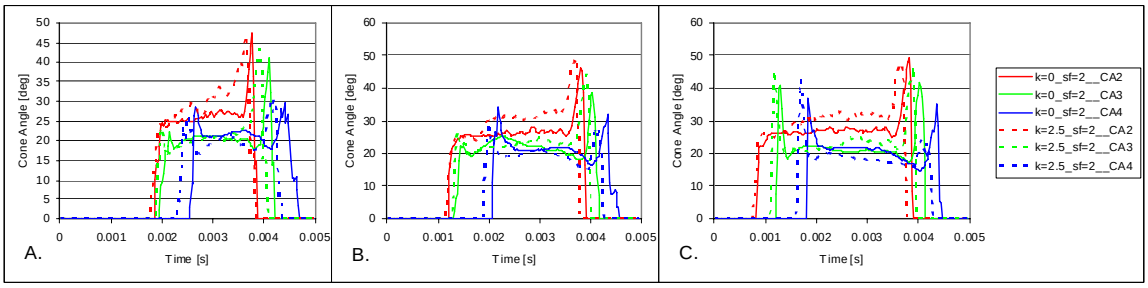

Figure 1.3.8. Time resolved cone angles of the combusting plumes for the 2.0 kg/min steady flow nozzles at 100MPa injection pressure. The ambient conditions in the HTPV are 120bar for all three plots and the temperature was A. 785K, B. 819K, and C. 865K .

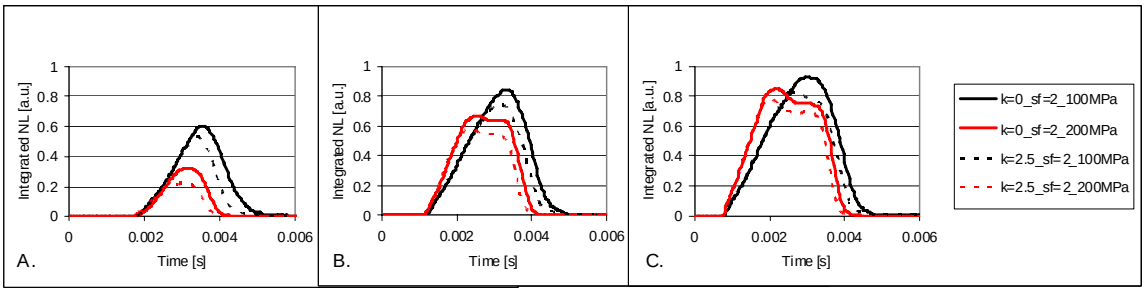

Figure 1.3.9. Time resolved integrated combustion luminosity for the 2.0 kg/min steady flow nozzles at 100MPa and 200MPa injection pressures. The ambient conditions in the HTPV are 120bar for all three plots and the temperature was A. 785K, B. 819K, and C. 865K .

In addition to the penetration and lift-off length data, the NL high speed movies were processed for time resolved integrated soot luminosity. While this does not provide a quantitative measure of soot production, it does provide a qualitative comparison of the soot levels produced by the k-factor nozzles over the varying operating conditions studied. Figure 1.3.9 shows the normalized integrated natural luminosity intensity for the 2.0 kg/min k=0 and k=2.5 nozzles. The k=2.5 nozzle shows lower peak levels of soot luminosity, however, due to the large volume of air available within the HTPV, the soot oxidation rates are likely higher than what would be observed within the cylinder of an engine.

While the above results for the 2.0 kg/min nozzle may hint at a possible path towards reduced soot emissions with the application of k-factor nozzle orifice geometry, it isn't known how the changes observed for a free jet in the HTPV will impact in-cylinder combustion. And, the results for the 2.8 kg/min steady flow nozzles showed different trends in liquid lengths, plume penetration rate, and peak soot luminosity levels. Unfortunately, the limited ambient conditions, and k-factor nozzle combinations tested to date add as many questions as answers to the efforts to understand if k-factor nozzles can be applied to consistently reduce engine out soot emissions.

2: Enabling Component Technology Development

2.1: Advanced Fuel Injector Development

Under the program, two new injectors were designed to enable high efficiency combustion recipes. Both injectors were targeted to operate at an injection pressure of 300MPa. To achieve accurate control of pilot and/or post injections, both injectors adopted piezo actuators, which could deliver smaller minimum fuel quantity and shorter dwell between injections than those of solenoid type injectors.

Figure 2.1.1. Phase 1 Piezo Injector

Figure 2.1.1 shows the picture of the Phase I injector. The Phase I injector featured the ability to perform very small, close-coupled, pilot, and split injections at very high injection pressure. Pilot quantities of less than 5 mm^3 delivered at rail pressures up to 300 MPa with a dwell between injections of less than 200 micro-seconds were required. The Phase I piezo injector was used to perform much of the single cylinder engine tests in this program at high injection pressure higher than 200MPa.

The Phase 2 injector, shown in Figure 2.1.2, was designed to deliver the capability varying injection rate and performing pilot injections at lower pressure than main injections. The selected concept was an intensified design that amplifies rail pressure to a higher level for injection. Target maximum injection pressure was 280MPa with 160MPa rail pressure and 2.0 area ratio. An intensifier built in the injector could boost fuel injection pressure from 160MPa to 280MPa.

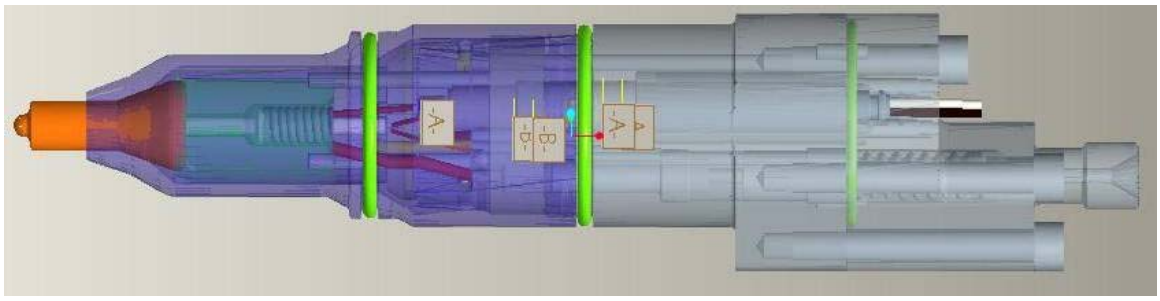

Figure 2.1.2. Image of the Phase 2 injector

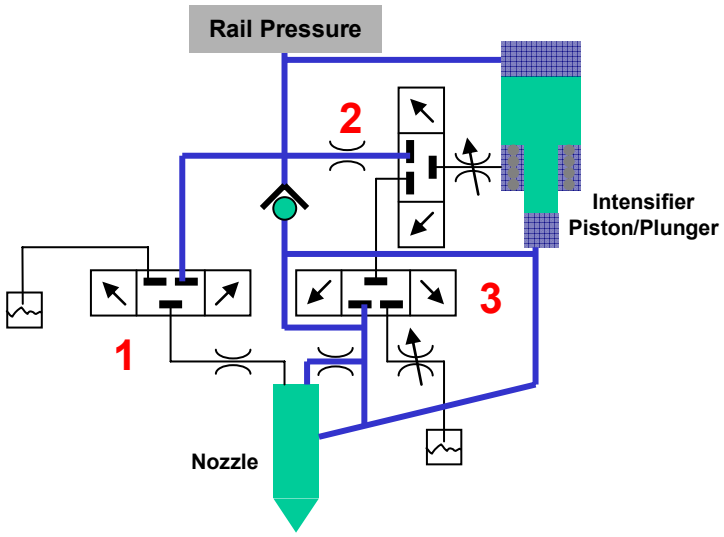

Figure 2.1.3. Phase 2 Injector Schematic Diagram

Figure 2.2.3 shows a schematic diagram of the design. The red numbers in Figure 2.2.3 represent three separate subsystems. Subsystem **1** is the nozzle check valve control. This piezo actuator is identical to the one employed in the Phase 1 injector. Subsystem **2** is a hydraulically operated valve that allows filling and emptying of the intensifier piston cavity. Subsystem **3** is the intensifier control. It also employed a piezo actuator. The injector could be capable of performing small (pilot) injections at either rail pressure or intensified pressure levels.

Figure 2.1.4 and Figure 2.1.5 show examples of the performance of the Phase 2 injector evaluated at a system simulation. Shown in Figure 2.1.4 is a square injection that emulates a single stage common rail system, a ramp injection that emulates a mechanically driven injector, and two boot injections in which the injection pressure is introduced at two separate levels. Ramp injections could be executed at various slopes. Figure 2.1.5 shows an example of pilot and post injections of the Phase 2 injector. The design of the Phase 2 injector has been validated at a system simulation under the program.

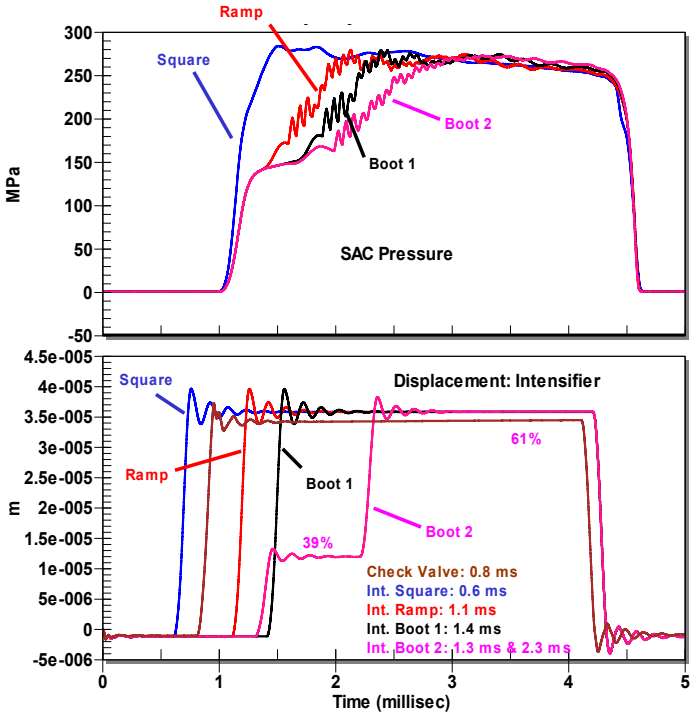

Figure 2.1.4. Examples of rate shaping capability of the Phase 2 Injector (simulation)

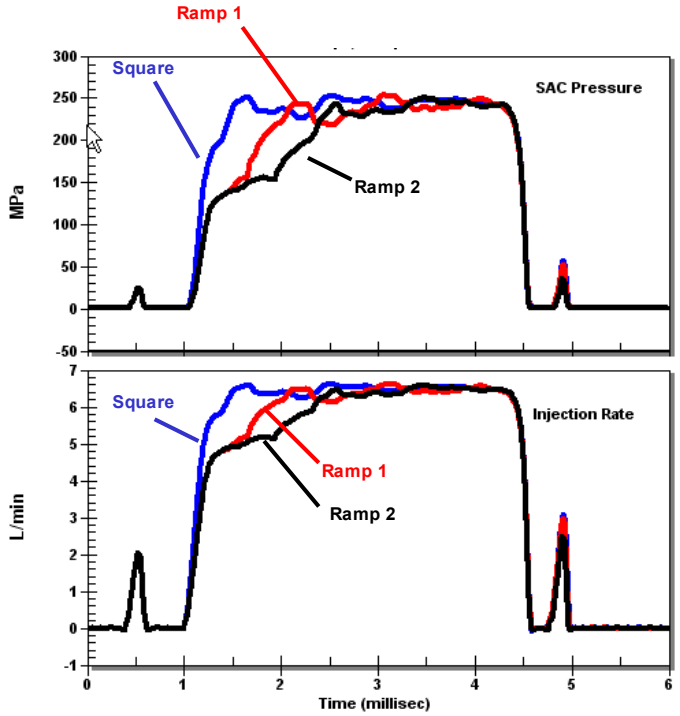

Figure 2.1.5. Examples of pilot and post injection capability of the Phase 2 Injector (simulation)

2.2: Variable Compression Ratio (VCR) Engine

A variable compression ratio (VCR) engine was designed under the previous DOE Heavy Truck Clean Diesel Program. This engine was built and tested under the current program. A schematic of the engine is shown in Figure 2.2.1. The VCR engine utilized a mechanism that allowed the distance between the crankshaft centerline and the bottom of the cylinder head to be varied by rotating the eccentric crankshaft carrier. The compression ratio could be varied between 8:1 and 18:1.

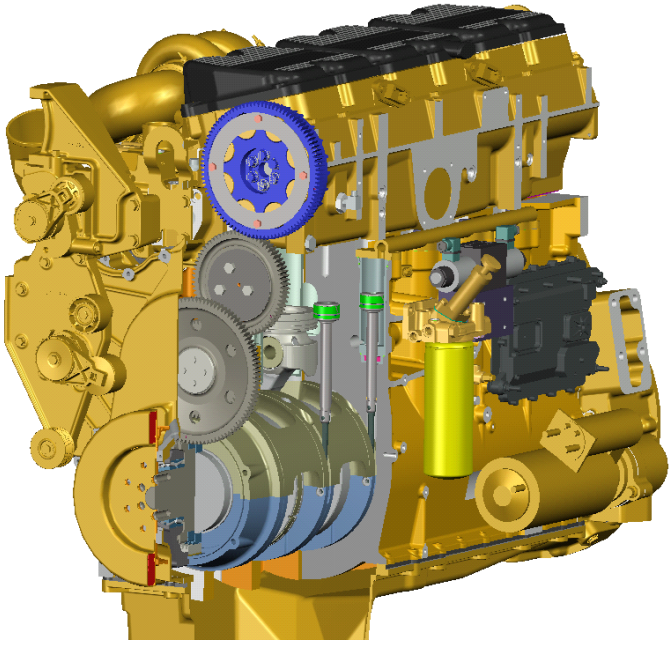

Figure 2.2.1. Schematic of variable compression ratio engine

The results of the testing performed with this engine were reported earlier in section 1.1.3:. At the conclusion of the testing, inspection of the VCR engine bearings revealed failures of the front and rear crankshaft carrier bearings. A failure analysis was completed and design changes to improve the durability of the crankshaft carrier bearings were investigated Short term fixes included changing the bearing material, coating, and surface finish. While these fixes would have a positive impact on durability, they were not considered sufficient for a long-term solution. Significant design changes would be required to alleviate the problem.

After several design iterations and several meetings with suppliers, a solid path for the crank carrier bearings was determined. This included single row needle bearings for the front and the rear bearings, and also a new oiling scheme. Although dual row needle bearings would have been ideal for a longer engine life, some additional analysis revealed that single row bearings would be sufficient for the 1000 hour estimated lab requirement. Going from a dual to a single row design greatly reduced the complexity of the required design modifications.

New front and rear housings, shown in Figure 2.2.2 and Figure 2.2.3, were designed and other parts modified to adapt the bearings to the existing carrier. Implementing the new bearing designs required only four new parts, and five existing part modifications. A separate oiling system for each bearing was also incorporated into the new bearing housings. This was important

to ensure that each bearing receives sufficient oil flow and pressure. The new oil system for the rear bearing housing is shown in Figure 2.2.4. A new oil supply to the front bearing housing via a hose was also added to ensure a sufficient supply of oil to the front bearing as shown in Figure 2.2.5. Another benefit of the new oiling setup is that clean oil can be provided to each new bearing. It was suspected that the sleeve bearings utilized in the original design were not only receiving insufficient oil, but the integrity of the oil was also in question.

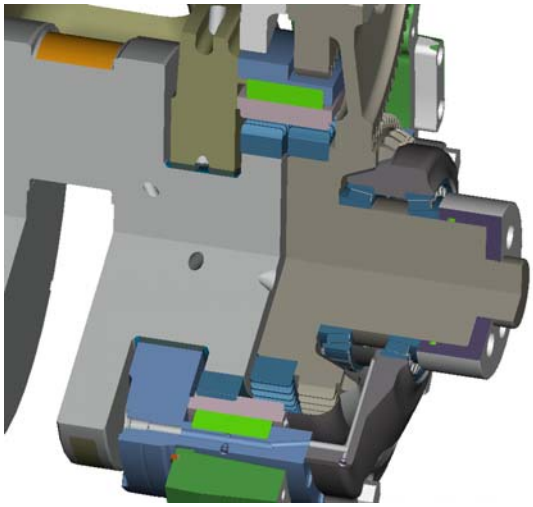

Figure 2.2.2. Cross Section of Front Bearing Housing Design with Needle Bearings.

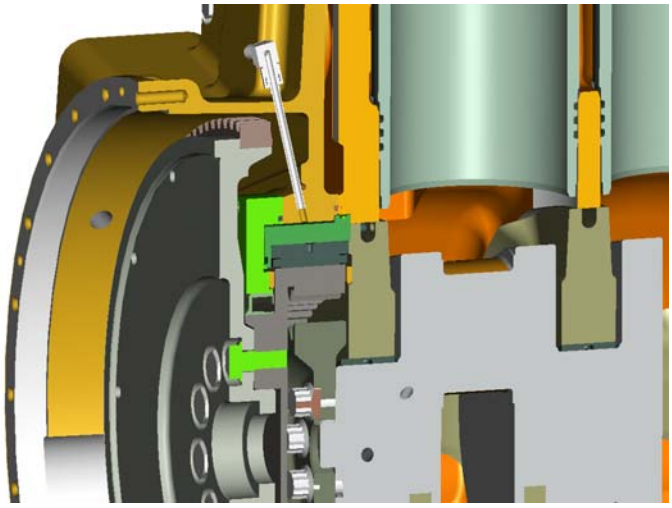

Figure 2.2.3. Cross Section of Rear Bearing Housing Design with Needle bearings

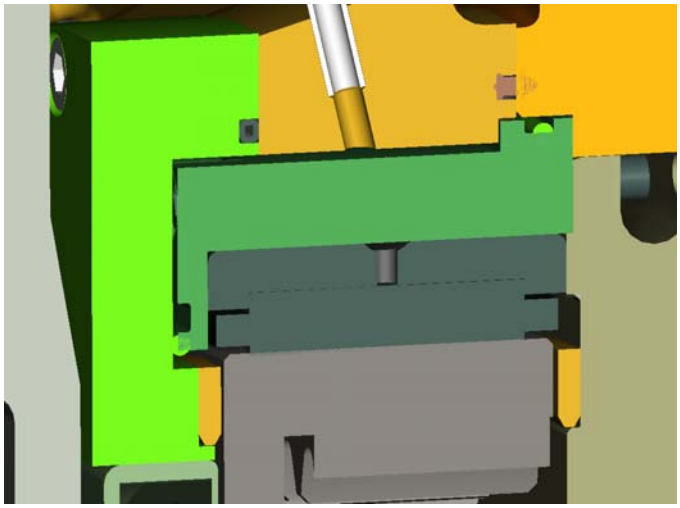

Figure 2.2.4. Detail view of Rear Bearing, Oiling system and seals.

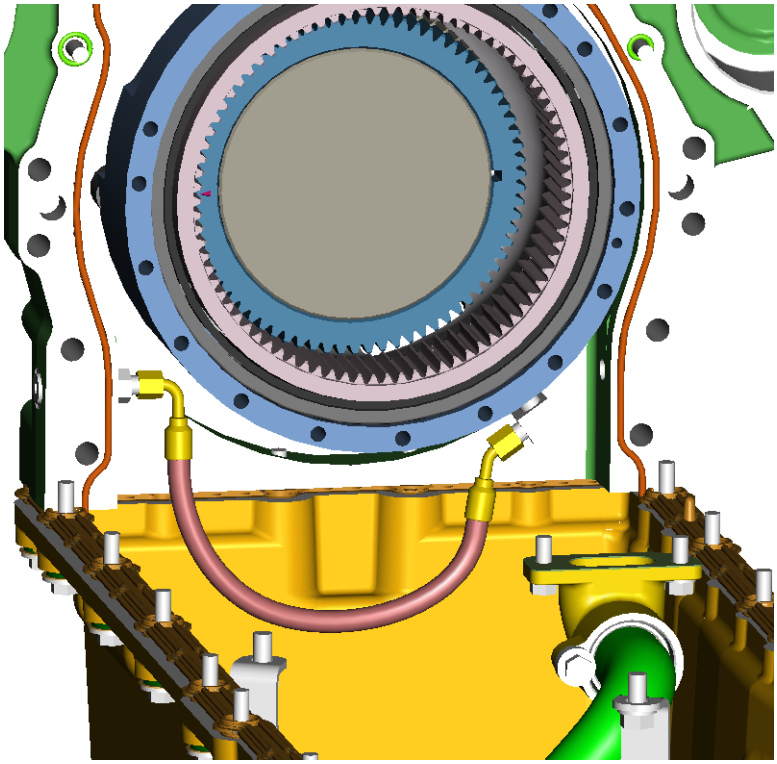

Figure 2.2.5. Front Bearing oil supply hose

An FEA model was built of the modified rear ring gear bearing and support housing system. Efforts focused on determining if rolling element bearing carrier deformations under load would still result in a predicted bearing life greater than the 1000hr lab target. The 1/16 model of the rear ring gear bearing outer race, housing and carrier, boundary conditions and loading are in Figure 2.2.6.

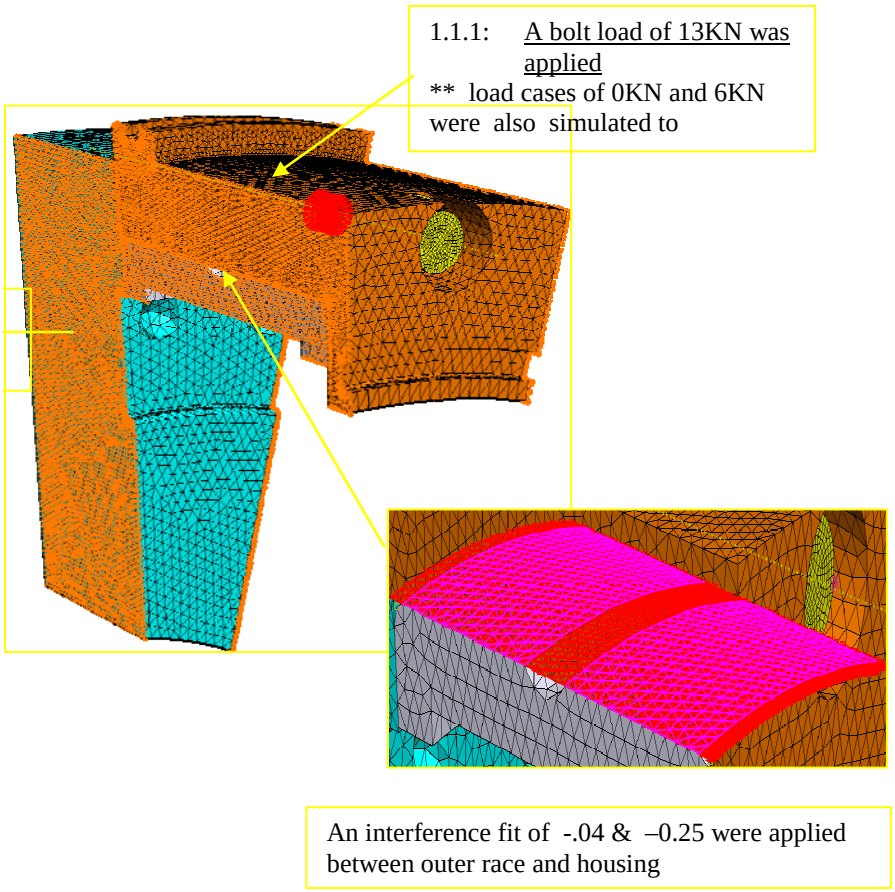

Figure 2.2.6. Model of rear ring gear bearing outer race, housing and bearing carrier.

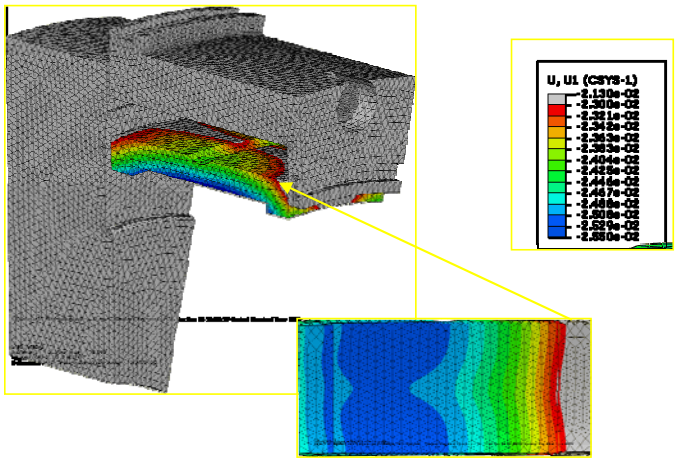

Figure 2.2.7. Radial displacements with 6kN bolt load and -0.41 mm press fit.

Outer race inner surface radial distortions, locations of housing maximum VonMises and maximum Principal stresses were predicted for several combinations of housing bolt load and race to housing press fits. Contour plots of results for a 6KN bolt load and -.041 diametral press are illustrated in Figure 2.2.7.

Results were reviewed with technical personnel from a bearing supplier. Predicted bearing outer race assembly displacements were acceptable. The assembly stresses on the bearing retainer were high at the FE model notched areas, but filleting and grinding of those areas would greatly reduce these notched stresses. The gross section assembly stresses were low and should not present a fatigue or yielding issues of the bearing retainer. Bearing lives were based on loads predicted during the original VCR design phase.

The design modifications proposed in this work were not implemented. Due to the cost and complexity of the VCR engine design, the high uncertainty of its durability and the lack of a sufficient benefit, the VCR engine was deemed too risky to be considered a viable production engine. Thus work on the concept engine was halted.

2.3: Precision Cooling

The goal of this work is to mitigate the increase in jacket water heat rejection (JWHR) through the liner and cylinder head associated with advanced combustion strategies by developing a process utilizing analytical tools which accurately predict heat transfer inside the engine. Once predictive capability is achieved, the cooling circuit passages can be designed to minimize heat transfer, while still maintaining structural life of the engine due to thermal cycling. The benefit of reduced heat rejection is a smaller frontal area cooling system and/or reduced fuel burned for cooling fan parasitic power. Reduced cooling system parasitic also supports goals of reduced imported oil dependency and global CO2 footprint. The reader is referred to the 4th quarter HECC report in 2008 for more detail.

Typically all jacket water (JW) pump flow is forced through the block and liner, even if not required, resulting in overcooling of much of the iron and absorbing more JW heat than is necessary. A reduction in jacket water heat rejection (JWHR) from the hot cylinder and exhaust ports, not including oil heat rejection, could be accomplished by reducing velocities of coolant in overcooled areas - hence the term 'Precision Cooling'.

Success is only achieved by the integration of analytical prediction of:

- engine performance in cylinder hot side conditions
- JW coolant total flow & internal distribution
- core engine thermal resistance & conjugate heat transfer (including the prediction of boiling)
- FEA stress & structural life analyses.

If we successfully reduce fuel energy rejected to the JW, a secondary benefit will come from recovering as much of that energy as useful work to improve overall engine thermal efficiency. This energy should be seen in the form of increased flywheel power (BMEP) and/or exhaust enthalpy to the turbine side of the turbo applied towards charge air pumping loss. Heat recovery beyond this point is out of scope.

2.3.1: Thermal Modeling of Jacket Water Heat Rejection in Block, Liner, and Head

Prediction of heat transfer from the hot in-cylinder combustion required looking at the interface surfaces between combustion and coolant as a heat exchanger as illustrated in Figure 2.3.1. Assuming the internal heat transfer surfaces of the engine, and walls separating them, can be meshed, then local heat flux can be determined by calculation of the three thermal resistances, and hot gas bulk coolant temperatures. The following sections describe how the hot side h_{fluid} or gas coefficient, iron thermal conduction k_{wall} *x, and $h_{coolant}$ are determined. The final section will cover the solution of summing all the heat flux into the coolant from entering the block to exiting the head.

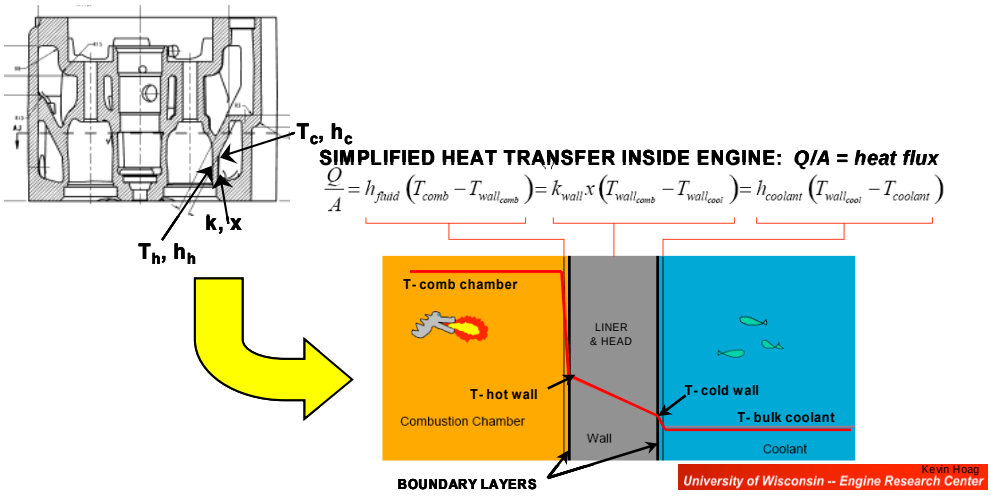

Figure 2.3.1 Cross section of cylinder head and illustration as heat exchanger

Prediction of Hot Side Gas Temperature & Heat Transfer Coefficient

Due to the large thermal mass of the cylinder head, liner and piston, and the relatively high speed of the four stroke combustion cycle transient values were not considered necessary for simulation in this study. Instead, cycle average values were used over the 720^{O} crank angle duration. A basic combustion simulation program first predicted these cycle-averaged bulk gas temperatures and heat transfer coefficients, which were applied to the entire in-cylinder surface. Based on previous test work and engineering judgment, the surface heat transfer coefficient distribution was modified for the given combustion recipe and BMEP rating. Straight-line approximations of the liner heat transfer coefficient data shown in Figure 2.3.2 were assumed, and the average and/or slopes were varied to achieve a better correlation between predicted and measured values.

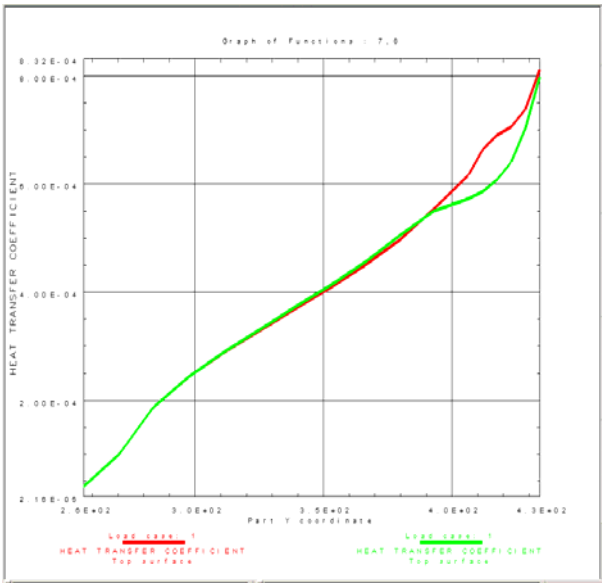

Figure 2.3.2 Heat transfer coefficients for liner as function of length

A similar method was also used for the radial distribution of heat transfer coefficient on the cylinder head. The heat transfer coefficient data is Figure 2.3.3 as function of distance from cylinder centerline.

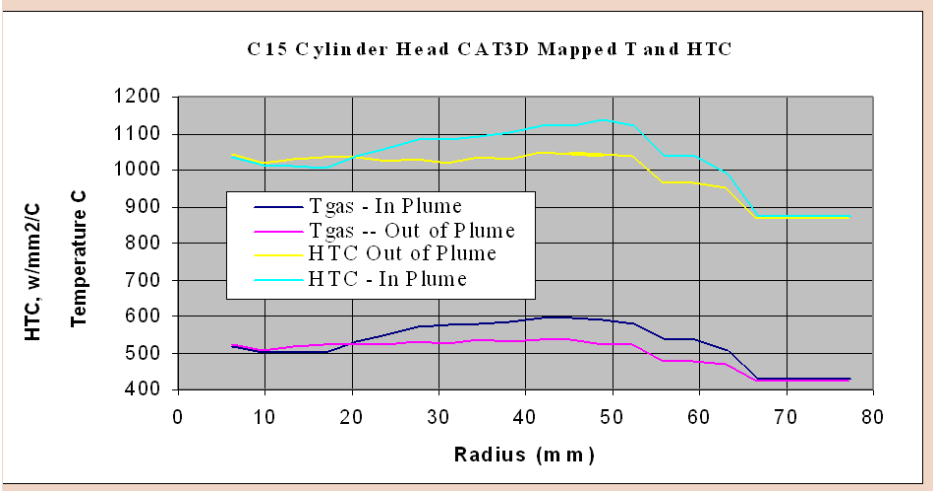

Figure 2.3.3 Gas temperature and heat transfer coefficients (HTC) for the cylinder head as a function of radius

Prediction of Jacket Water Heat Rejection – Forced Convection Heat Transfer

At this point all the heat transfer coefficients at the hot and cold side metal surfaces, the localized wall thickness, localized thermal conductivity and hot gas bulk temperature were known or calculated in the conjugate heat transfer process. The iron and coolant volumes were meshed, and combined into a single model consisting of around 20M cells, as illustrated in Figure 2.3.4. Since the engine oil and CGI coolers were modeled as porous media for pressure drop purposes, the heat loads measured from tests were added to the model at each cooler to raise the coolant temperature the appropriate amount before moving downstream. Exhaust gas and charge air pre-cooler heat loads were considered to be accurately calculated using the gas side mass flow and temperature delta. While the charge air pre-cooler heat load was used in the total heat balance results reported later, it is out side of the control volume of the conjugate heat transfer analysis. An accurate lube oil cooler heat load was not obtainable, so what was measured accurately was a combination of oil cooler heat transferred into the water estimated at 23.4 kW.

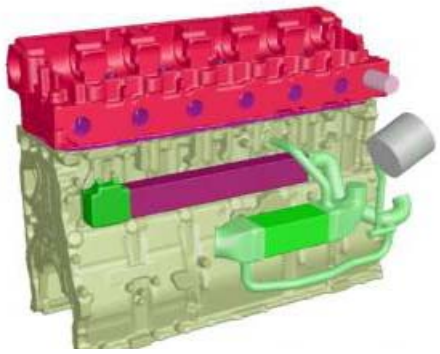

Figure 2.3.4 Computation mesh for prediction of jacket water heat rejection

Total engine JW heat rejection (including exhaust gas, charge air cooler, and engine oil cooler) was accurately measured using RTD thermocouples in and out of the engine and a micro-motion flow meter. An accurate comparison of energy transferred from the hot side surfaces directly into the coolant were not expected to correlate well to test values. However, changes in the prediction with or without boiling, or changes due to different boundary conditions were considered accurate.

2.3.2: Correlation of Jacket Water Conjugate Heat Transfer

The first conjugate heat transfer run shown was iteration #13 with a given set of boundary conditions using forced convection only (e.g. no boiling). This will be followed by results that used the same boundary conditions, but employed the boiling model for generating heat transfer coefficients when superheat (wall temperature in excess of bulk saturation temperature) exceeded 10^{O}C. This is accomplished with a user defined subroutine (UDF) in Fluent. Correlation with coolant and metal temperature will then be made.

To achieve closer correlation with test results an additional set of runs will be shown using directionally correct changes in hot side boundary conditions. Again, correlation with temperature will be made, but this time with metal temperatures only, since bulk coolant temperatures correlated well on earlier runs.

.

Conjugate Heat Transfer Prediction Using Forced Convection Only

Figure 2.3.5 shows boundary conditions for Run #13. These come from the initial combustion simulation, with some added engineering judgment. Note that later analysis in Run #14 using the boiling model also used the same initial boundary conditions.

Conjugate Heat Transfer Boundary Conditions & Inputs		
Surface Ambient Conditions:		
T-ambient outside block:	25.0	^{O}C
Block/Head Control Volume Surface HTC:	20.0	W/m^2/^{O}K)
Coolant Fluid Conditions:		
Coolant Flow Rate From JW Pump after Pre-Cooler:	229.2	kg/min
Coolant Temp from JW Pump:	88.5	^{O}C
Engine Oil Cooler Heat Load	23.4	kW
CGI Cooler Heat Load:	33.9	kW
Oil Cooler Coolant Mass Flow	140.7	kg/min
Coolant Pres From Engine:	40.0	kPa
In-Cylinder Hot Side Conditions:		
T-gas bulk in cyl.	570.0	^{O}C
Cylinder Head Surface HTC	962-1188	W/m^2/^{O}K)
Liner Top Surface T-gas	410.0	^{O}C
Liner Top Surface HTC	770.0	W/m^2/^{O}K)
Liner Bottom Surface T-gas	230.0	^{O}C
Liner Bottom Surface HTC	21.6	W/m^2/^{O}K)
Exhaust Port Surface T-gas	674.0	^{O}C
Exhasust Port Surface HTC	132.9	W/m^2/^{O}K)
Intake Port Surface T-gas	57.6	^{O}C
Intake Port Surface HTC	19.8	W/m^2/^{O}K)

Figure 2.3.5 Run 13 & 14 boundary conditions

Measurement & Correlation of Total Engine Heat Balance

The first energy balance looks at the outer control volume in Figure 2.3.7 marked by large red arrows. The energy entering the control volume included only the fuel energy rate. The energy leaving the control volume included: the flywheel power out, the exhaust enthalpy out, the net change in enthalpy rate of the fresh charge air from intake to exhaust (charge air heat rejection is broken down into narrower categories below), the net change in enthalpy rate of the coolant (the jacket water heat rejection including lube oil heat absorption which was transferred to coolant in the engine oil cooler), and the engine surface convection loss calculated as a remainder term. This does not include radiation loss from the exhaust manifold or turbo, as this is a manifold-to-manifold energy balance. It is depicted in both pie graph and tabular form below as Figure 2.3.6.

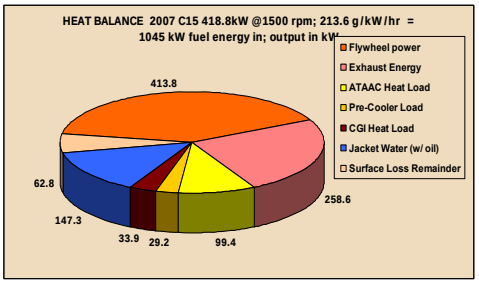

ENGINE ENERGY BALANCE		kW	%
Energy Input:	fuel	1045.0	100.0%
Energy Outpu	wheel power	413.8	39.6%
	Exhaust Energy	258.6	24.7%
	ATAAC Heat Load	99.4	9.5%
	Pre-Cooler Load	29.2	2.8%
	CGI Heat Load	33.9	3.2%
	Jacket Water (w/ oil)	147.3	14.1%
	Surface Loss Remainder	62.8	6.0%
	TOTAL	1045.0	100.0%

Figure 2.3.6 Total energy balance: intake manifold to exhaust manifold

The predictive heat rejection analysis study was pertinent to the second and inner control volume shown in Figure 2.3.7. The inlet boundary began at the water pump outlet and ended at the thermostat. It also included heat transfer off the surface of the block and head. Note that the pre-cooler was outside of this control volume. The energy exchanged within this control volume

still must be consistent with the larger control volume and agree with the total energy balance measurements in the test cell based on fuel energy.

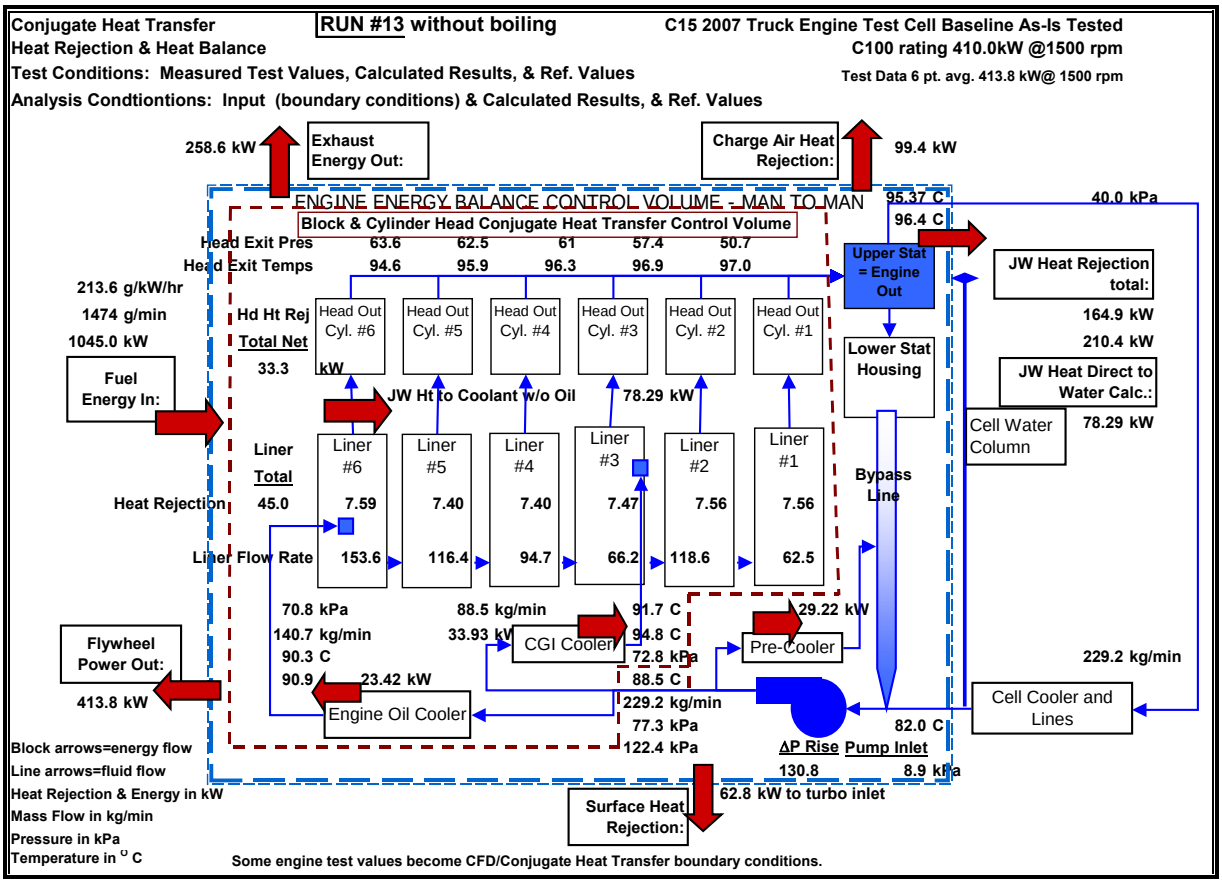

Figure 2.3.7 Conjugate heat transfer control volume with results and measurements w/o boiling

Figure 2.3.8 below looks at the inner control volume, referenced in Figure 2.3.7, which is what was analyzed in all following conjugate heat transfer models, both with and without boiling. Here the energy into the control volume was defined by the hot side boundary conditions, accurately measured values of exhaust cooler heat, and our best estimate of lube oil heat. Note the pre-cooler was outside of this control volume. Energy leaving the control volume was the increase in enthalpy rate of the coolant and the surface loss off the engine – again manifold to manifold (intake port inlet to exhaust port exit). One major challenge in this project was the amount of book keeping required to insure that the same energy values were congruent in both control volumes.

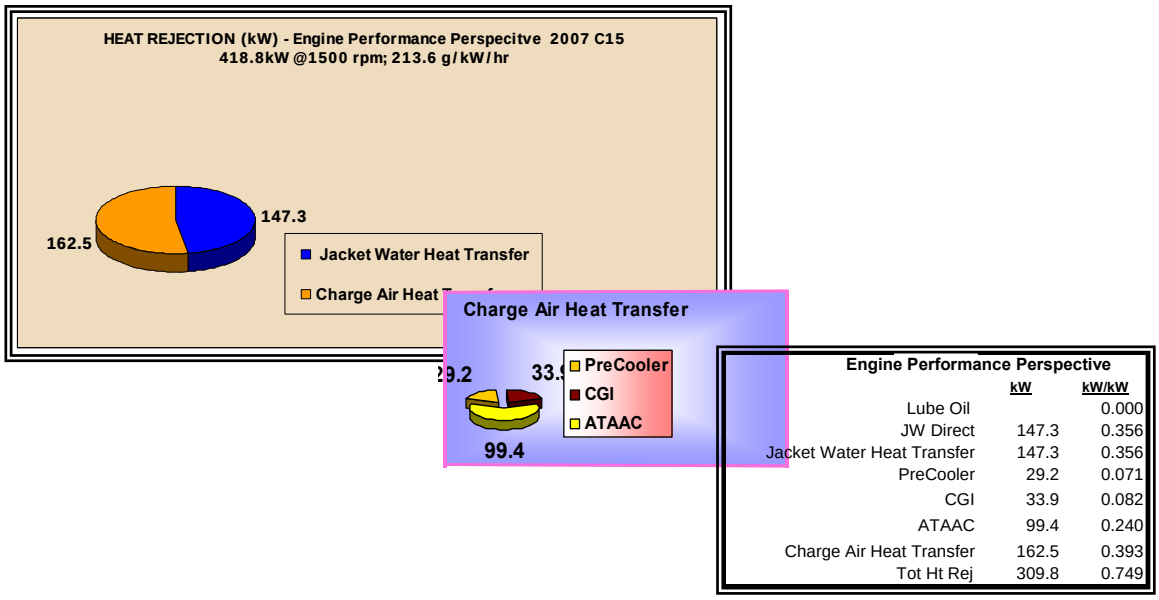

Figure 2.3.8 Reconciled energy balance between both control volumes

Comparison of temperature predictions with and without boiling

While prediction of heat rejection in total did not significantly change, the implications for localized temperatures were more pronounced. Coolant temperature comparisons are made first. As shown in Figure 2.3.9 below, some coolant temperatures already known to be boundary conditions, such as JW pump out, and the heat exchanger temperatures using heat loads based on measured values. No effects of boiling were expected or were seen here.

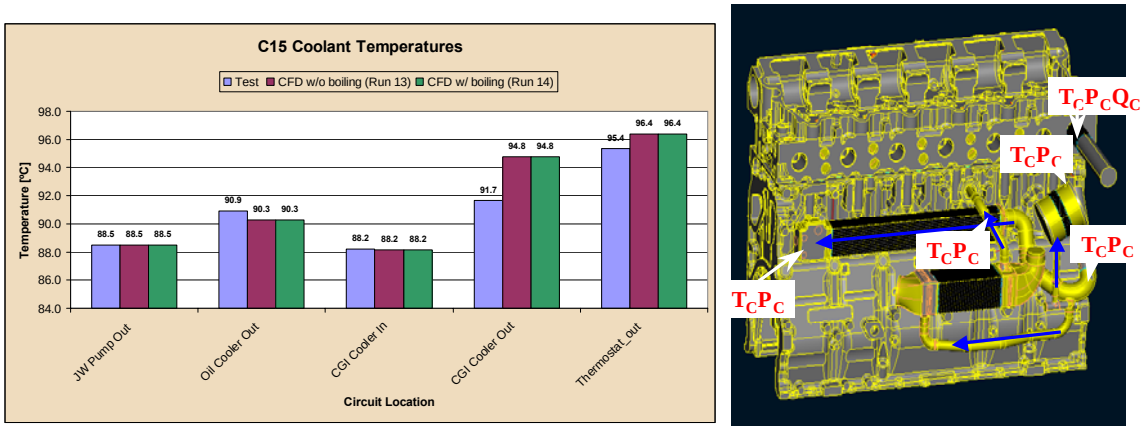

Figure 2.3.9 Conjugate heat transfer cooling system with results and measurements

Cylinder #6 Results

Measured vs. predicted results for cylinder #6 are shown below in Figure 2.3.10. The location labeled as flange outside actually was measured just below the o-ring on the gas side. In general liner temperatures were in fair agreement with the test for cylinder #6, considering that measurement accuracy was +/- 1^{O}C; and predictive accuracy with mesh size and thermal gradients was about another +/- 2^{O}C. Ignoring the flange area, the temperature error at and below the o-ring averaged 6.7 ^{O}C on the left side, and 12.0 ^{O}C at the hotter front side. In every case the temperature was hotter towards the top of the liner; gas side was hotter than the coolant side; and when the boiling function was used in the conjugate heat transfer model temperatures were lower as expected and came closer to measured values. The exception is the flange location which is far from any coolant passage and thermal gradients were expected to be higher as well as predictive accuracy.

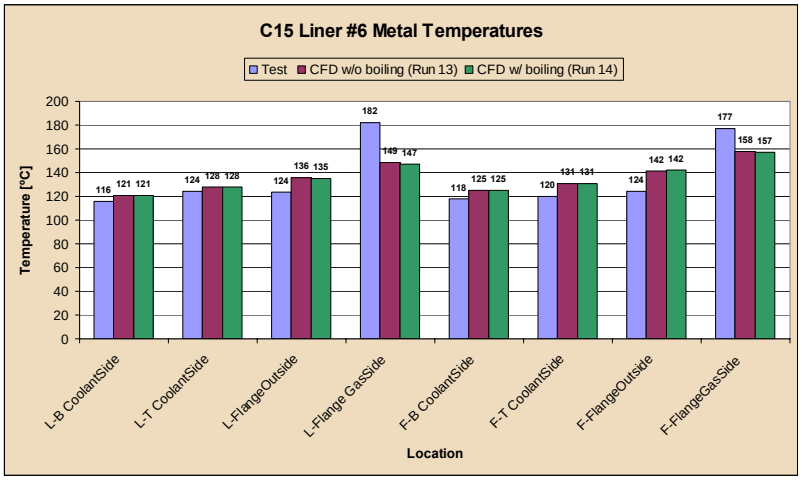

Figure 2.3.10 Comparison of Cylinder #6 liner metal temperatures (predicted vs. measured)

Cylinder #4 Results

Measured vs. predicted results for cylinder #4 are shown below in Figure 2.3.11. Again, the location labeled as flange outside actually was measured just below the o-ring on the gas side. In general liner temperatures were in fair agreement with test for #4. Ignoring the flange area, the temperature error at and below the o-ring averaged 1.3 ^{O}C on the left side, and 17.0 ^{O}C at the hotter front side. Again temperature was hotter towards the top of the liner; gas side was hotter than the coolant side; and when the boiling function was used in the conjugate heat transfer model temperatures were lower as expected and came closer to measured values. Cylinder #4 indicated fairly significant boiling at the front location where it was hotter than on the left. The #4 liner will later be shown, using CFD results, to have the lowest flow of the six cylinders. Again the flange location gradient is expected to be higher as well as predictive accuracy.

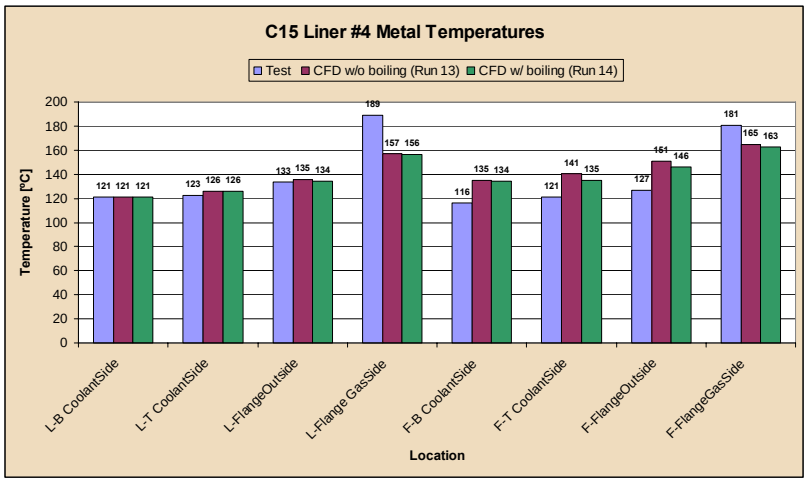

Figure 2.3.11 Comparison of Cylinder #4 liner metal temperatures (predicted vs. measured)

2.3.3: Precision Engine JW Cooling Process Applied

This absolute heat rejection and correlation with measure metal temperatures is not claimed due to use of the same boundary conditions with low bulk gas temperature. The purpose is to study, given the same boundary conditions (including gas temperature), how does this heat rejection with balanced liner flow compare with the base line design output shown in Figure 2.3.12, both run with boiling prediction. Intuition is proven out in the analysis with very little change in heat rejection. It is left to the reader to make as detailed a comparison as desired. But in summary the important heat rejection impact is summarized below.

	Run 14	Run 15
Liner Flow Distribution	base line	equal
Heat Rejection (kW)		
Liner #1	7.56	7.38
Liner #2	7.46	7.43
Liner #3	7.39	7.49
Liner #4	7.31	7.47
Liner #5	7.53	7.50
Liner #6	7.54	7.61
Net Cylinder Heat Transfer	33.35	33.47
Total Calculated JWHR to Coolant	78.14	78.35

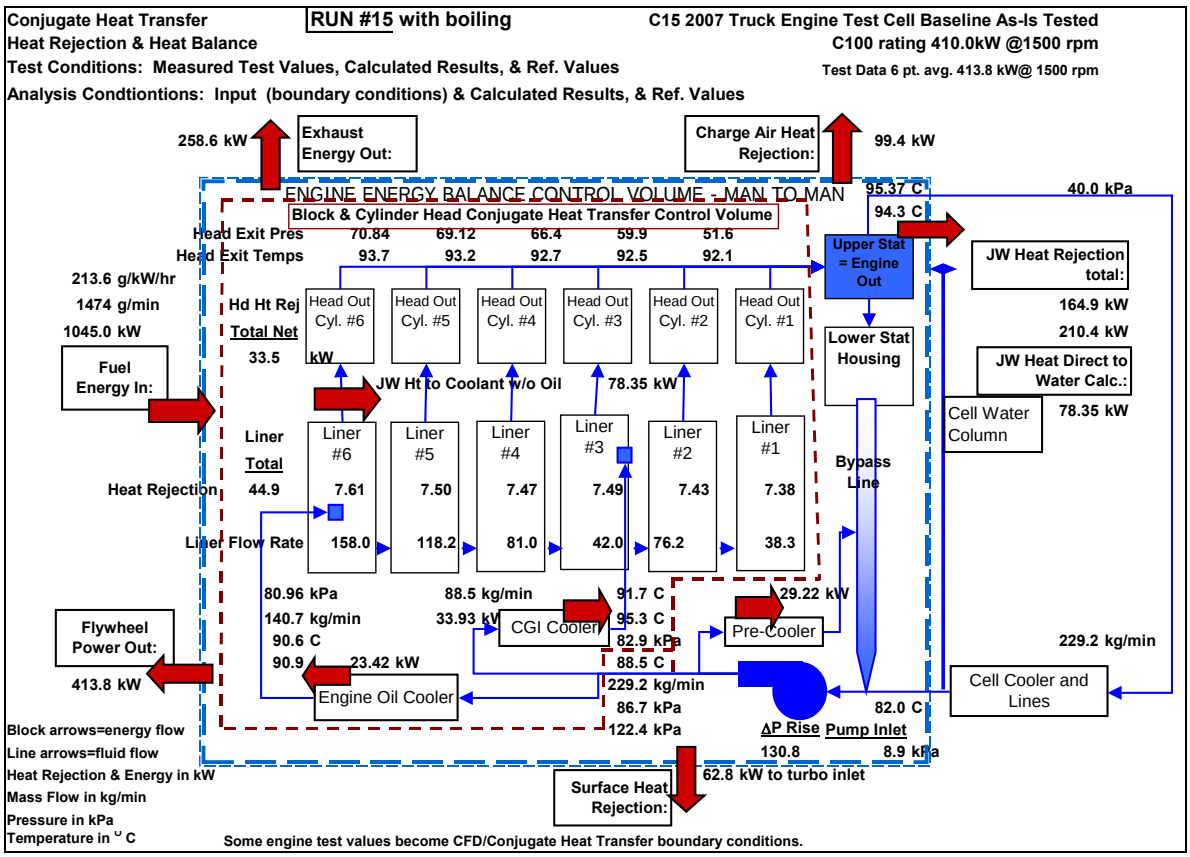

Figure 2.3.12 Conjugate heat transfer control volume with results and measurements without boiling

Conclusions

The conclusion would be that flow rate has little impact on heat transfer coefficients around the liner when the entire liner surface area in included. Most likely the greatest amount of heat transfer is occurring at the top land where velocities are very high in a narrow area. But the impact on structural life of the cylinder head may change drastically. That work remains to be done. The above exercise should again increase confidence that the conjugate heat transfer model does work and is viable.

2.4: Combustion Controls

The development of advanced engine control systems is focused on delivering sensor technologies and control strategies necessary to meet the requirements of a production viable, high-efficiency, clean combustion engine. This involves developing strategies, advanced algorithms and sensors for controlling the combustion process, understanding the interactions between systems and controlling the entire engine system. The task was divided into two major tasks; one developing a real time high speed data acquisition system that can be used in conjunction with engine controller and second to develop control algorithm for transient engine control of a multi-cylinder HCCI engine.

The purpose for the High Speed pressure DAQ system is to sample in-cylinder pressure sensor data at 1 crank degree resolution and transmit it (over CAN at 1Mbaud, the fastest available transmission rate) to an xPC based real time engine controller to enhance/enable HCCI controls. The in-cylinder pressure data is critical in order to implement feedback control on rate of pressure rise and combustion phasing (defined as the crank angle at which maximum rate of pressure rise happened) in a HCCI engine controller. The DAQ system should be sophisticated enough to perform fast and robust pressure data sample and at the same time perform calculations on the acquired pressure data to determine parameters of interest (maximum rate of pressure rise, crank angle of maximum rate of pressure rise, peak pressure and crank angle of peak pressure).

The first device used to accomplish high-speed sampling of in-cylinder pressure sensors was based on FPGA chips. A rapid prototyping system was developed for controls development using Matlab/Simulink software for model building and code generation. The rapid-prototyping hardware consisted of an XPC target box equipped with CAN cards and a Caterpillar designed programmable FPGA card enabling processing of speed-timing pulses from the crank/cam targets and generation of the output pulses needed for the various engine sub-systems such as fuel injection. This data acquisition system had robustness issues resulting in an occasional dropped data point or a corrupted crank angle measurement. Moreover, it was limited in its functionality. Its only purpose was to transfer the pressure measurements to the xPC, which then performed all of the required calculations for desirable parameters (Maximum pressure, Crank-angle for maximum pressure, Maximum pressure rise rate, Crank-angle for maximum pressure rise rate).

Hence a new, microcontroller-based data acquisition system was developed in which, all such calculations will be performed within and only the desired parameters will be passed to the real-time controller (xPC) ensuring significant reduction in overhead on the real-time controller.

The micro-controller based pressure data sensing system was setup in cell running the HCCI engine. After synchronizing with the speed-timing signal from the engine, the pressure trace was fast sampled in a window at crank angle from -60 degree to 60 degree, as shown in Figure 2.4.1. The micro-controller also performed calculations for the acquired pressure data to find the peak pressure ($P_{\max}$) and maximum rise rate ($\Delta P_{\max}$) and their corresponding crank angles (θ_{peak} and $\theta_{riserate}$) respectively. The processed results were packed in CAN messages and transmitted to target PC through CAN bus.

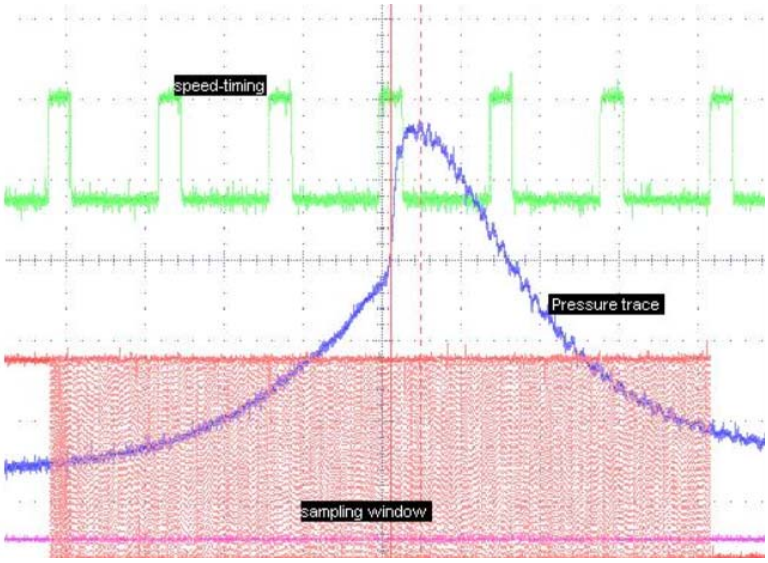

Figure 2.4.1. Pressure data sampling

Results and discussion

The AVL™ Indimeter results are used as a benchmark to compare the results obtained using the micro-controller. It should be noticed that the sample rate of the AVL™ data acquisition system is crank angle based and is fixed at 5 samples per degree. So for different engine speeds, the time-based sample frequency will be different. For example, at 1000rpm engine speed, the time-based sample frequency for AVL™ is 12kHz. For the microcontroller based DAQ, the sample frequency is time-based and fixed at 60kHz. Therefore, the total number of samples collected will be different at different engine speeds.

It is noted that in AVL™ data acquisition system, the algorithm to search crank angle of maximum rate of pressure rise is set up such that the heat release is first calculated and the location of heat release is used as a reference to locate the maximum rate of pressure rise. The searching for the maximum rate of pressure rise stops at 2 crank angle degree after the crank angle at which maximum heat release occurs. In microcontroller based data acquisition system, however, the searching for the peak pressure and maximum rate of pressure rise are conducted in the whole sample window, which is from –60 crank degree to 60 crank degree.

Experimental Results

Results were obtained from a single cylinder engine running in HCCI combustion mode for engine speeds at 800, 1000, 1200, 1400, 1600 and 1800 rpm. Typical pressure trace as acquired by the DAQ is shown in Figure 2.4.2. As can be seen, substantial ringing is observed in the raw pressure signal. The ringing noise is treated as an artifact of pressure transducer location and response characteristics and not as a physical phenomenon happening inside the cylinder. Hence before calculating the parameters of interest, the ringing noise needs to be removed from the pressure data. The results before and after the filtering are also compared in Figure 2.4.2.

.

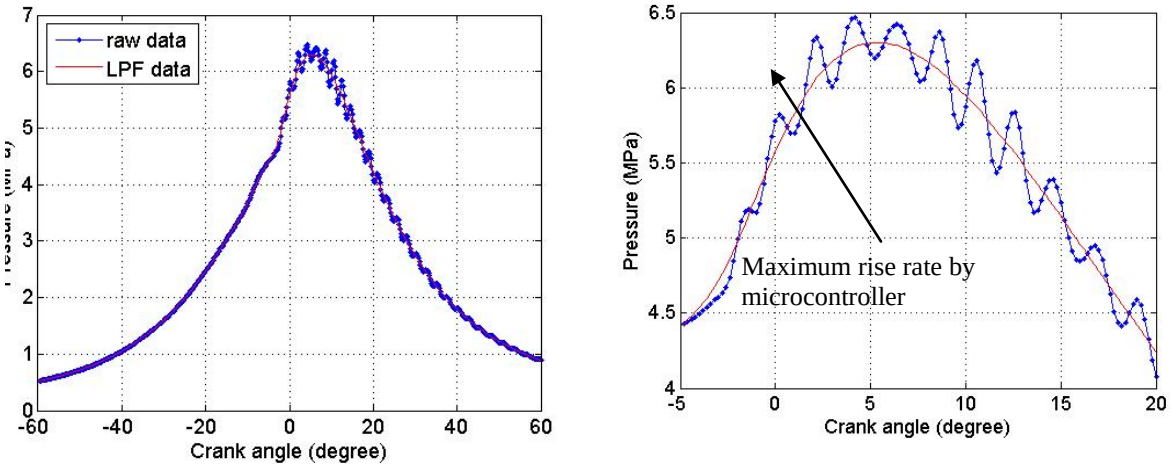

Figure 2.4.2. Offline test of a low pass filter at 1200 rpm

A bidirectional filtering technique is applied to make the recursive low pass filter (LPF) with zero phase shift. The results of maximum rise rate versus its crank angle for 100 cycles are plotted in Figure 2.2.3. The figure clearly illustrates that the microcontroller results fit with the AVL results. Histogram plots of the distribution of maximum pressure rise rate and the distribution of crank angle at which maximum pressure rise rate occurred are shown in Figure 2.4.4. For each engine speed, the left part of the figure is the distribution of rise rate at that engine speed and the right part of the figure is the distribution of crank angle.

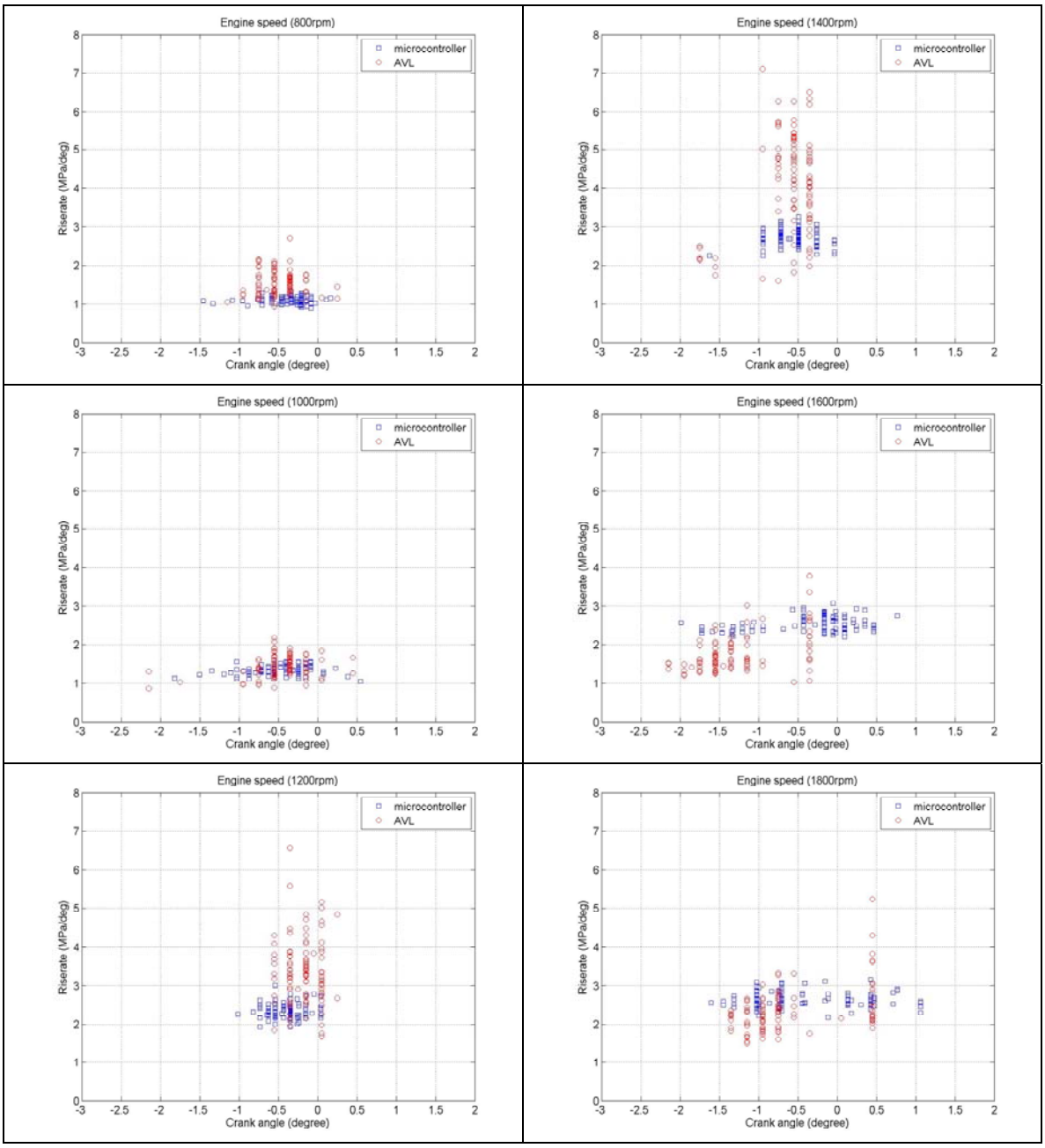

Figure 2.4.3. Comparison of the maximum rate of pressure rise and its crank angle for 100 cycles with low pass filter.

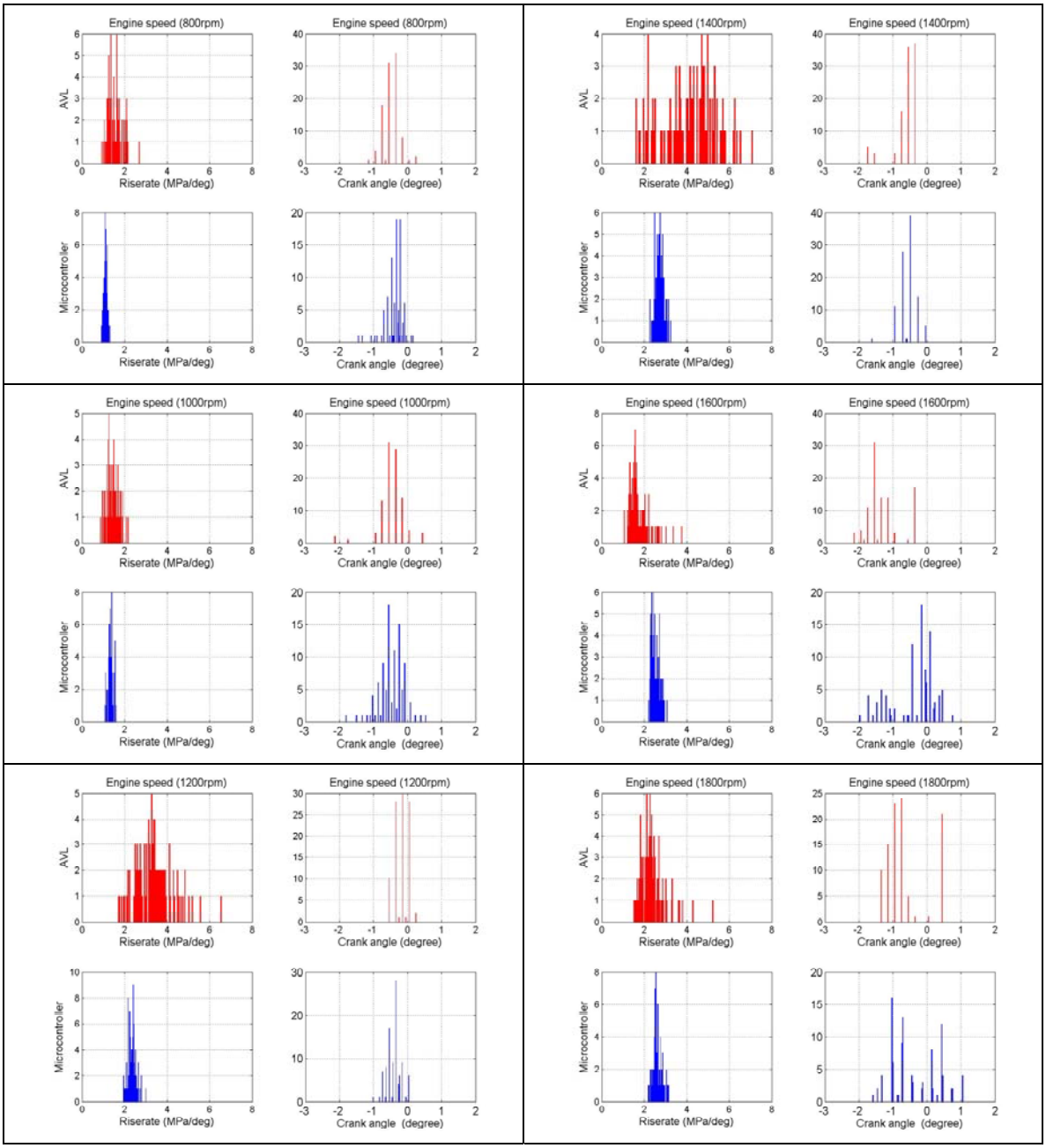

Figure 2.4.4. Histogram plot of the distribution of maximum rate of pressure rise and its crank angle for 100 cycles; red: AVL™ results; blue: microcontroller results with low pass filter.

With the LPF, the crank angle found by the microcontroller has similar distribution with that found by the AVL™. The averaged results of the crank angle for 100 cycles are also plotted in Figure 2.4.5. As shown in the figure, the crank angle from the microcontroller is almost constant for different engine speed. Figure 2.4.4 shows the maximum rise rate found by the microcontroller is located in the range of that by AVL™. The variation of the microcontroller result is smaller than that of the AVL™ result, which is quantitatively shown by the standard deviation in Figure 2.4.6. From the figure, the rise rate is proportional to the engine speed at this running condition. The higher engine speed results in larger rise rates. The AVL™ result, however, did show this change.

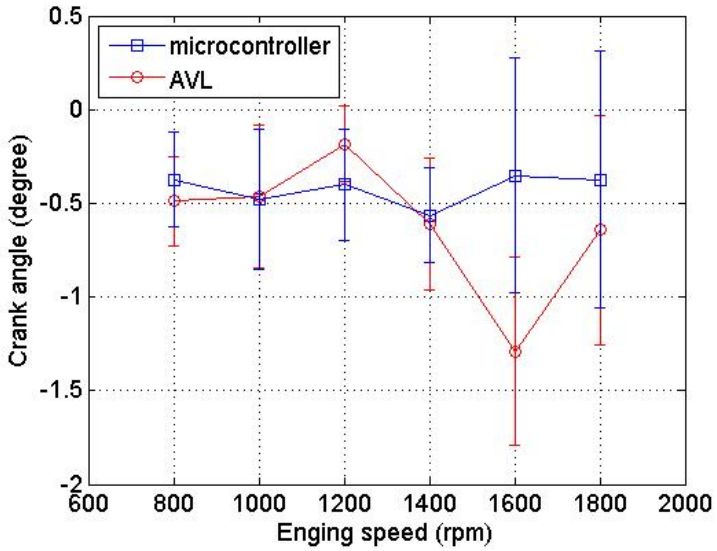

Figure 2.4.5. Averaged crank angle for different engine speed; error bar is the standard deviation.

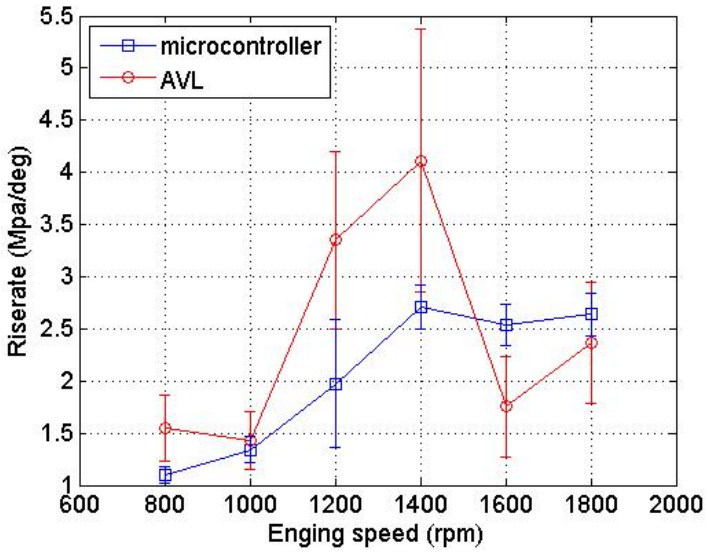

Figure 2.4.6. Averaged rise rate for different engine speed; error bar is the standard deviation.

The DAQ system is then coupled with the xpc based feedback controller to control combustion phasing at a desired crank angle while other control factors (like EGR, injection timing etc) are varied. One such experimental result is shown in Figure 2.4.7. Excellent control of combustion phasing is obtained at the desired combustion-phasing angle of 1 crank angle degree before top-dead-center (dBTDC) while the fuel injection timing is varied.

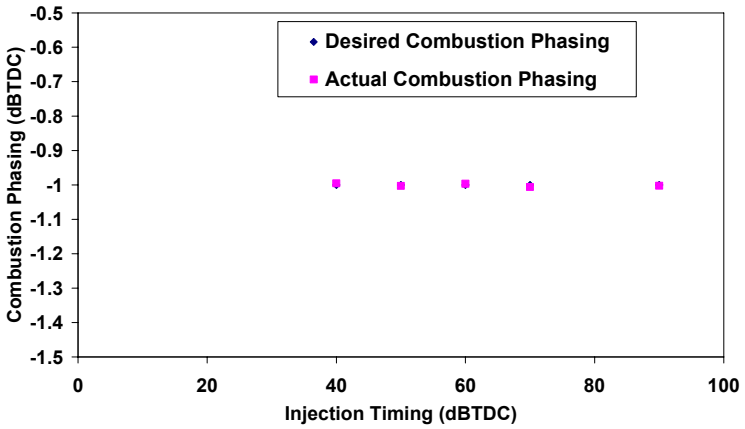

Figure 2.4.7. Utilizing the micro-controller based DAQ system and xpc based controller, the combustion phasing is controlled at desired combustion phasing while injection timing is varied.

The microcontroller based data acquisition system is sophisticated enough to perform fast and robust pressure data sample and at the same time perform calculations on the acquired pressure data to determine parameters of interest (maximum rate of pressure rise and its crank angle). By applying a software low pass filter, the microcontroller based data acquisition system can successfully find the maximum rate of pressure rise and its crank angle, no calculation of heat release is performed.

Transient Control

The second challenge in the advanced control algorithm development task is to develop a control algorithm for transient engine control of an HCCI engine. Demonstration of satisfactory transient operation of an HCCI engine is imperative. Transient response of an engine depends on the maximum rate at which fuel can be added into the combustion chamber without causing undesirable operation (based on emissions and performance). For a HCCI engine the two parameters that limit the maximum fuel rate is rate of pressure rise and emissions. The rate of pressure rise in a HCCI engine primarily depends on the amount of EGR and the combustion-phasing angle. The emissions primarily depend on air/fuel ratio, amount of EGR, fuel injection pressure and the combustion-phasing angle. Hence 5 different control inputs are identified that can affect the transient operation of the HCCI engine. These are compression ratio (CR), intake valve actuation (IVA, for the purpose of this report it is the crank angle at which intake valve is closed), exhaust gas recirculation (EGR), fuel injection pressure and end of fuel injection angle (EOI). All of these parameters can be controlled in real time using our existing control architecture. Utilizing the Variable Compression Ratio (VCR) engine, compression ratio is an additional control knob that was not available in our previous transient testing on the fixed compression ratio engine. Real time control of compression ratio (CR) is achieved using a

feedback from position sensors on the hydraulic pistons that are used to change CR. In addition, oxygen sensors are installed in the intake and exhaust manifold to provide real time information on amount of EGR flowing into the cylinder. The oxygen sensors have a response time of ~150ms, which is, fast enough to provide real time EGR control. Intake valve closing angle, as explained in previous reports, is primarily used for combustion phasing control. Solenoid control injectors are used to control the fuel injection pressure and injection angle in real time.

IAV Automotive Engineering Inc. has teamed with Atkinson LLC to develop optimized control maps for Caterpillar Inc. using their proprietary neural network based approach. In order to best simulate the system for controls optimization efforts, engine models must be developed that account for multiple inputs and non-linear behavior. Artificial neural networks were chosen as the best candidates to provide the level of accuracy and computational efficiency required. A neural networks based approach requires collecting a diverse set of output data (emissions and performance) for a widely varying range of input parameters (the 5 parameters identified above). Hence a map-based approach is followed to accommodate different set of input maps for a widely varying range of input parameters. A key requirement in successfully capturing the system response in a data driven approach (like neural network based modeling) is to collect output data for almost all possible input parameters combinations. Since it is not realistically possible to exploit all possible input combinations a large number of maps (~35) are generated to accommodate sufficient combinations of input parameters. An important consideration is to ensure the randomness in the input choices. Any biased (based on previous test experience) set of input parameters will provide outputs that are not reflective of complete dynamics of the system. Ideally the inputs should be randomly varied (along a reasonable mean value) as of representing white-noise signal. For the transient data presented in this report, due to safety considerations (a steep drop in CR can cause the HCCI engine to misfire and not run), maps for certain input parameters (like CR) are generated with very little variations along a mean. However, the choice of mean was totally random (within the limits).

Transient operation of a multi-cylinder HCCI engine within two points in the engine operation condition was demonstrated. Various control maps are generated for different control inputs (IVA, EGR, CR, EOI and Injection pressure) and these maps are then loaded into engine control software to perform a specified speed-load transient. These transients provide understanding of the effects of different control parameters on performance parameters during transients. This understanding helped in developing better maps for different control parameters, which allowed transients to be performed with much higher speed load ramp values. The input-output data recorded during these transients are also utilized to develop NN-based model for the engine. These models can be used to perform multi-variable optimization on different input parameters and can be instrumental in developing optimum transient control strategies for the HCCI engines. Moreover, response time characterization of some control parameters is done to identify limitations of the current engine hardware.

3: Engine System Efficiency Analysis

3.1: Well-to-Wheels Analysis

A thorough analysis approach on evaluating system efficiency and its environmental impact is known as the Well to Wheels analysis. It has emerged as one of the most powerful analytical tools to provide comprehensive estimates of environmental impact (green house gas, GHG, footprint) of full-fuel-cycle including contributions from each step i.e. extraction, processing, transport and end use of the fuel. The analysis consists of two major portions, one including extraction, processing and transportation of the fuel (called as Well to Tank portion) and second including the end use of the fuel (called as Tank to Wheel portion) in automobiles, machines, power generation etc. Such an analysis can provide estimates of where the opportunities for improvement exist to reduce the GHG footprint of a given fuel/vehicle system.

Well – to- Wheels Tool Development

First law of thermodynamics (referred as first law) is an energy accounting principle, which provides quantitatively energy in processes like heat transfer, work transfer, energy flow and energy generation. The first law in its simplest form can be written as

$$\Delta E_{CV} = E_{in} - E_{out} + Q - W + E_{gen}$$

where ΔE_{CV} is change of Energy in the control volume
E_{in} is Energy flowing into the control volume
E_{out} is Energy flowing out of the control volume
Q is heat transfer to the control volume
W is work done by the control volume
E_{gen} is Energy generated in the control volume.

First law analysis can be used to provide first law efficiencies of various components in the system. First law efficiency is defined as the ratio of desired energy outcome (for e.g. work in case of engines) to the total energy input (for e.g. total fuel energy input in case of engines). First law analysis can be performed on overall system as a control volume or it can be performed on each component of the system. When done on system level, the analysis provides overall system efficiency and an estimate of total loss in the system. When done on component level, the analysis can identify inefficient components and provide a systematic approach for improved energy utilization. However, an important shortcoming of first law analysis is that it treats all forms of energy equally irrespective of the ability of the system to utilize the energy to perform useful work.

The Second law of thermodynamics (referred as second law) provides information on the potential for energy to produce useful work. Second law defines the concept of availability or exergy, which is defined as the maximum useful work that can be obtained from the system due to physical and chemical differences between the system and its surroundings. Availability, unlike energy is not conserved. Second law in its simplest form can be written as:

$$dA_{CV} = \sum_{in} dA_{in} - \sum_{out} dA_{out} + \sum_{i} \dot{dQ}_i \times \left(1 - \frac{T_o}{T_i}\right) - dW_{cv} + P_o dV_{CV} + dA_{des}$$

where dA_{CV} is change of availability in the control volume
dA_{in} is availability flowing into the control volume
dA_{out} is availability flowing out of the control volume
dQ_i is heat transfer to the control volume from ith boundary at temperature T_i
dW_{cv} is work done by the control volume
dA_{des} is availability destroyed in the control volume
T_o,P_o represents dead state temperature and pressure respectively.

Availability is a state property and for systems with same composition as its surroundings availability is defined as

$$A_{Physical} = (U - U_o) + P_o(V - V_o) - T_o(S - S_o)$$

where U and U_o are the internal energy of the system and the dead state
V and V_o are the volume of the system and the dead state
S and S_o are the entropy of the system and the dead state

If the system composition is different than its surroundings then additional work can be obtained from the system by bringing the system composition in chemical equilibrium with the surroundings. This portion of availability is called chemical availability and is defined as

$$A_{Chemical} = -\Delta G = \sum_{i} m_i \left(\mu_i - \mu_i^o\right)$$

where ΔG is Gibbs free energy of the equilibration process
m_i, μ_i are the mass and chemical potential of the species i in the system
μ^o_i is the chemical potential of the species i at dead state.

Total availability is the sum of physical availability and chemical availability. Second law or availability analysis provides significant insight into identifying processes that are detrimental to the potential of energy to do useful work. Similar to the first law, second law analysis can be performed either on the complete system or on each component of the system.

Development of a first and second law analysis tool was completed that can be used as a post processor on the Cat 1-D engine cycle simulation code (known as 973). The tool allows both system level and component level analysis and allow the user to choose components for which the user want to output the results. The tool output results in both plots and tabular format. One sample result is shown in Figure 3.1.1.

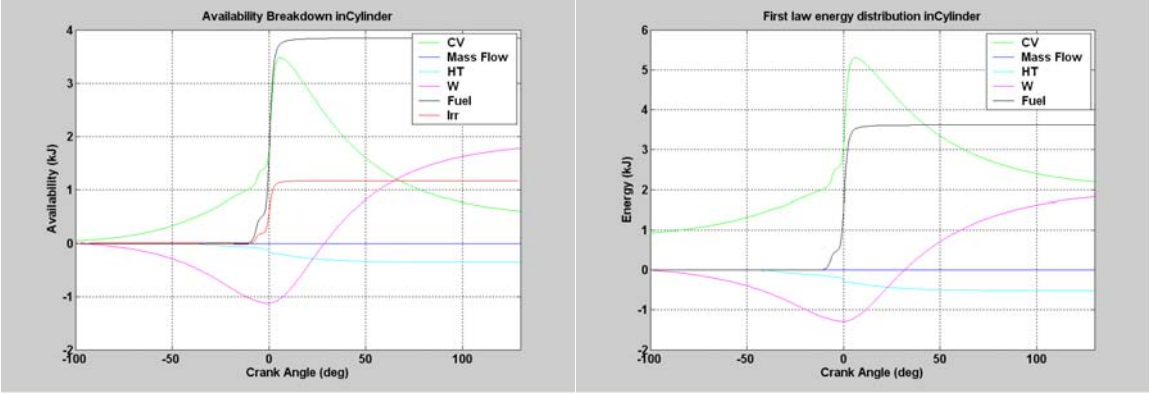

Figure 3.1.1. Sample plot output by the post processing tool for a component.

A detailed component level analysis of the system using this tool will help in determining where thermodynamic losses are occurring and will help in prioritizing the opportunities available for recovery of those losses. A thorough first law analysis on experimental data of a multi-cylinder HCCI engine is completed. The results are compared to a similar analysis done on the experimental data of a multi-cylinder conventional diesel engine. The purpose behind such a comparison is to identify the advantages and the disadvantages of HCCI combustion over conventional diesel combustion from the perspective of thermal efficiency.

A literature review was completed on existing Well to Wheels studies. The existing studies primarily focused on light duty vehicles. Various fuels including bio fuels, alcohols and even non-carbon based fuels (like H_2) were included in previous analysis. The literature review provided an idea of the framework required and the existing models (especially for the Well to Tank (CONCAWE / EUCAR / EU Joint Research Council Study (V2c), GREET Model (V1.8b)) portion of the study) to do such an analysis. Similar framework can be replicated, however the focus now is going to be on heavy-duty engines for both on-road vehicles and off-road vehicles/machines.

Different machines, due to the inherent nature of the task they perform, utilize the engine differently. Some machines keep the engine in the close vicinity of an operating point (desired engine speed and desired engine load defines an engine operating point) for most of its operation. Other machines shift the engine operating point considerably over short periods of time and thus operate the engine through transient operation for most of its operation. The engine performance depends on whether the engine is run close to steady state or run through transient.

From the Tank to Wheels perspective, the first step is to consider various machines operation histograms and select at least one machine of both steady state type engine operation and transient type engine operation. Once the machines are identified, an energy audit on the complete machine (including engine, transmission, implements and the lower powertrain) will be performed with current configuration. A step further would be to consider possible technological advancement in various subsystems like engines, transmissions etc and carry out an energy audit on the machine with future possible configurations. The analysis will be repeated for various different fuel options to capture the effect of both Well to Tank and Tank to Wheels efficiency.

Machine application selection will be targeted in coming months along with gathering required performance data for different engines (with different fuels).

A complete energy audit on various (on-highway and off-highway) applications is critical in understanding the energy flow through the system and thereby identifying the opportunities for future improvements in thermal efficiency of the system. The efficiency improvements are possible both by improved component efficiencies and by improved system integration.

A tank to wheels (TTW) energy audit was performed on 3 different applications, namely an off-highway hauling application, an off-highway cyclic application and an on-highway truck application, all of them powered by a Cat heavy-duty engine. For each of these applications, 4 different sources of energy supply are considered. Those were; diffusion combustion (conventional) based heavy-duty diesel engine, an engine based on premixed Charged Compression Ignition (PCCI) combustion using a low cetane fuel, lean burn heavy-duty natural gas engine and stoichiometric gasoline combustion based heavy-duty engine. The diesel based diffusion combustion was defined as the baseline case and the other 3 concepts of power generation were evaluated with the assumption that the engine was run in the exact manner as in the baseline diesel case, i.e. the PCCI, natural gas and gasoline cases had the same engine speed/load to compare tank to wheel efficiencies for each case.

Analysis Approach
The analysis was done using combination of engine data, application field data and Caterpillar proprietary cycle simulation tools. The overall analysis process followed is shown in the flow-chart in Figure 3.1.2.

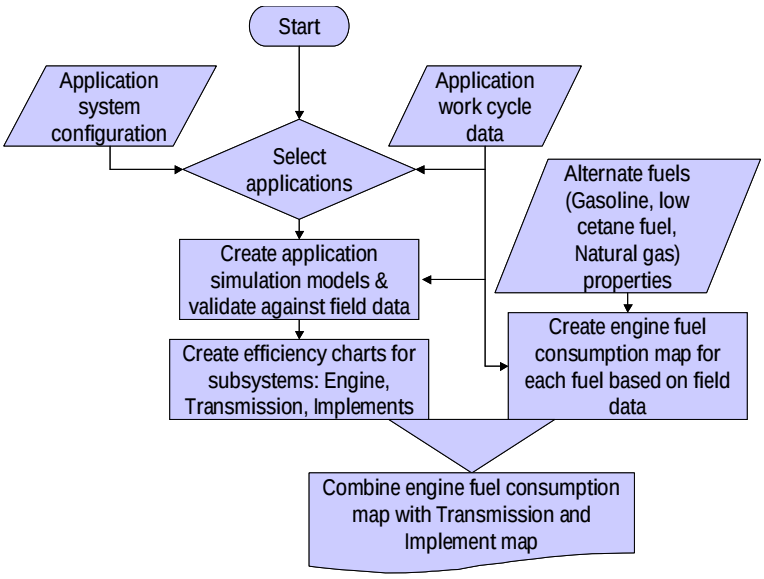

Figure 3.1.2. Flow chart showing Well-to-Wheels analysis approach

The assumptions made during the analysis are as follows

- Application histogram data is a reasonable representation of field operation
- Effect of different fuels on engine transients neglected

- Engine operating points (Speed/Load) are the same for different fuels
- Reduced heat release durations represent full-load PCCI operation
- Technologies (low-cetane fuel) exist that could be used to control the heat release as desired in full load PCCI operation
- PCCI combustion evaluated for both part load and high load cases.
- Natural gas engine was a lean burn engine having a compression ratio in the range of about 13:1
- Port injected gasoline engine, operating stoichiometric with a 3-way catalyst with a compression ratio of 10:1.
- Drive train efficiency was same as the baseline diesel case for all other technologies

Results for Off-Highway Applications

Figure 3.1.3 shows the typical lug curve for a heavy-duty hauling application and Figure 3.1.4 shows the % of the diesel fuel that is burnt at different points of the engine power-speed map during the course of a hauling cycle, which is depicted in Figure 3.1.5. It is clearly seen that that most of the fuel is burnt at the higher loads indicating little part load operation for the hauling application.

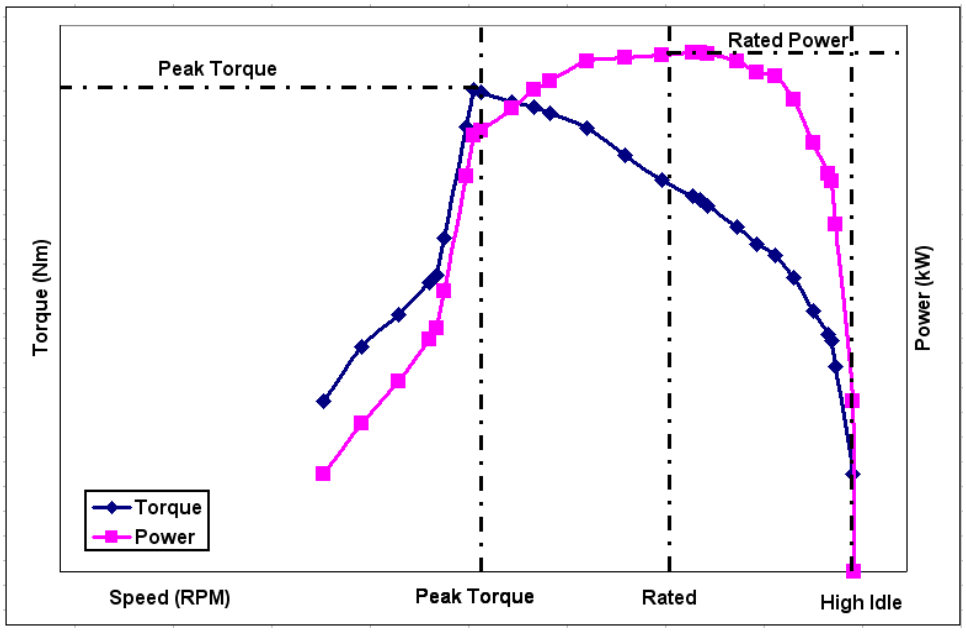

Figure 3.1.3. Speed-Torque & Speed-Power curve for the chosen hauling application

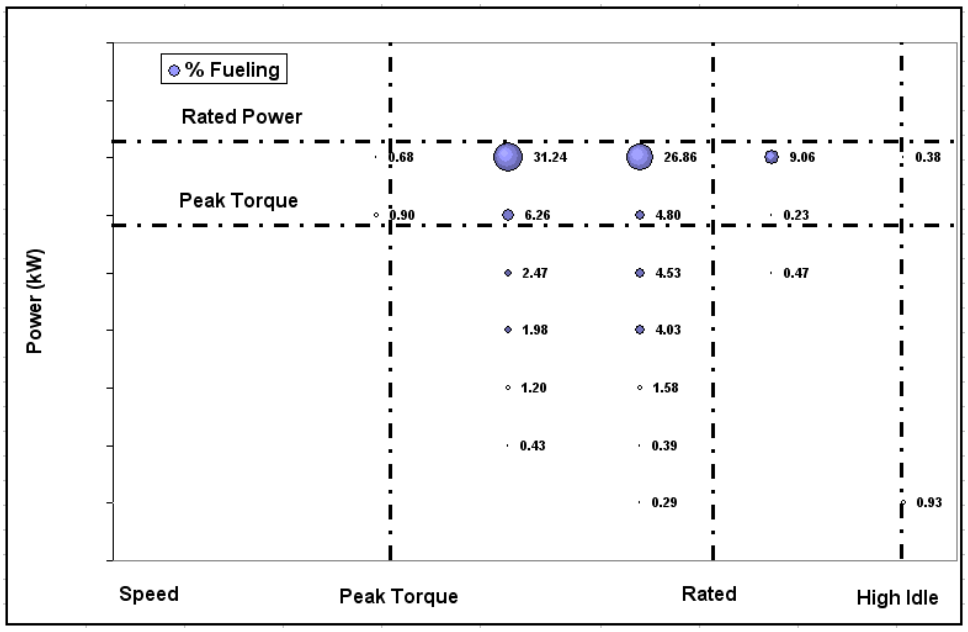

Figure 3.1.4. Histogram of fuel burnt at different operating conditions for the hauling application

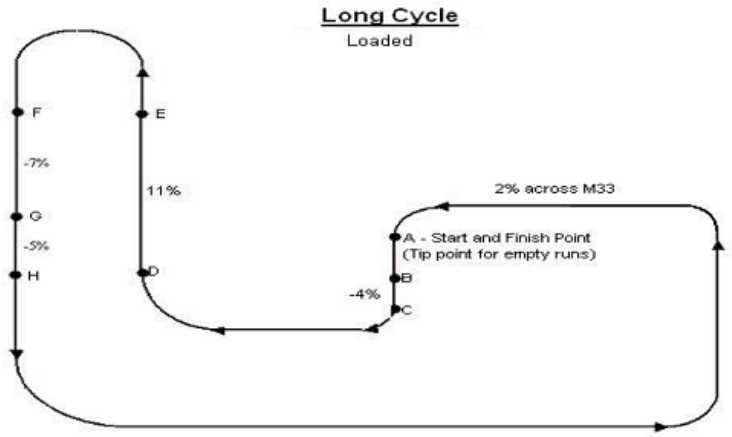

Segment	A-B	B-C	C-D	D-E	E-F	F-G	G-H	H-A
Distance - meters	97	48	525	479	493	438	278	1320
Grade - %	0	-4	0	11	0	-7	-5	0

Figure 3.1.5. Typical path through which the application cycle was generated for hauling application

Figure 3.1.6 depicts the various (engine, non-engine, overall system) efficiencies for the 4 energy source technologies being evaluated on this application. Performance histogram data suggest that most of the fuel is burnt at the higher loads for this application; hence any technology that improves only part load fuel consumption will not be of great advantage on this application. The part load PCCI (low cetane number fuel) operation does not result in any brake thermal efficiency improvement for the engine when compared to the baseline diesel case. If the PCCI operation can be extended to the higher loads by the means of load extension technologies that

allow control of rises rates or combustion phasing, there is an improvement in the engine brake thermal efficiency of about 3 %. Figure 3.1.7 shows the percent fueling decrease as the PCCI operating load is increased. At the higher loads there can be as much as a 6% benefit in fuel consumption if the engine operates with a PCCI form of combustion having a narrow heat release near TDC.

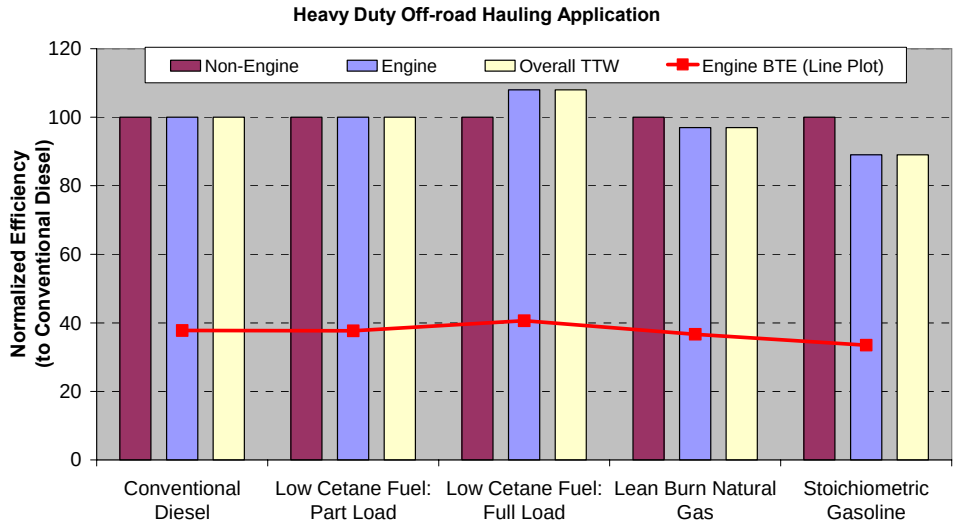

Figure 3.1.6. Efficiencies normalized to baseline diesel engine in hauling application

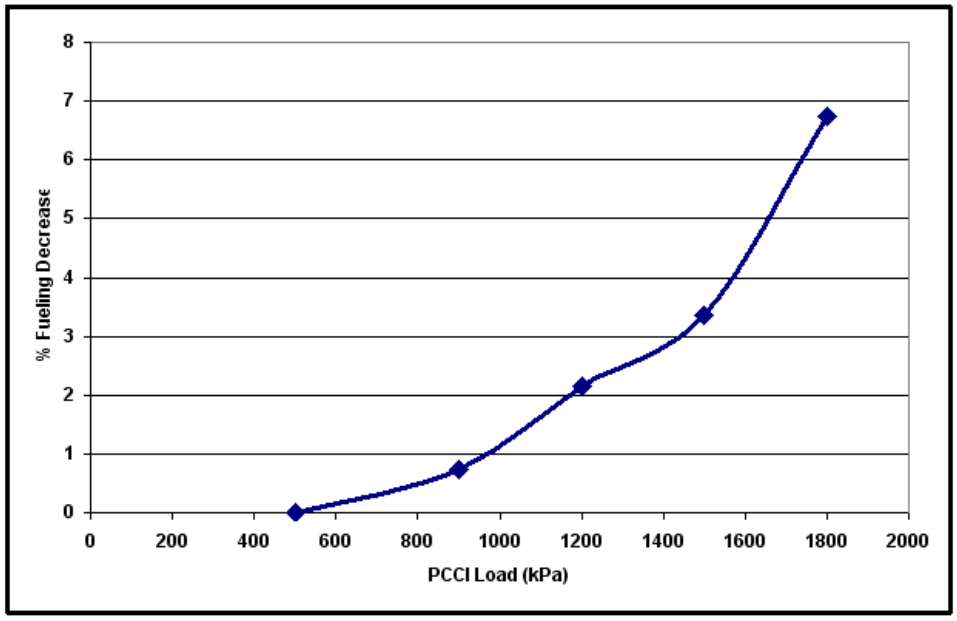

Figure 3.1.7. Fuel benefit of increasing PCCI load range for hauling application

The lean burn natural gas engine was about 1% less efficient than the baseline diesel engine. The fact that most of the operation for this application happens at the higher loads makes the natural gas engine a lot closer in efficiency to the baseline diesel engine. The high levels of part throttling losses are lower in this case as the application loads over the cycle are high. The lower

compression ratio with throttling losses makes the natural gas engine less efficient than the baseline diesel (~ 1, 1.5 % Lower). The stoichiometric gasoline engine with an even lower compression ratio of around 9-10:1 due to the lower knock margin of gasoline has much lower engine thermal efficiency (3, 4% Lower) when compared to the baseline diesel.

Results for Off-Highway Cyclic Application

Figure 3.1.8 shows the typical lug curve for a typical heavy-duty cyclic application and Figure 3.1.9 shows the % of the diesel fuel that is burnt at different points of the engine power-speed map during the course of a typical application cycle for the cyclic application. The application work cycle is depicted in Figure 3.1.10. It is clearly seen that a cyclic application certainly has significantly different fuel consumption distribution. Where as most of the fuel is burned at the higher loads indicating little part load operation for the hauling application, in case of a cyclic application part load fuel consumption is more significant. This is very important for assessment of thermal efficiency building blocks.

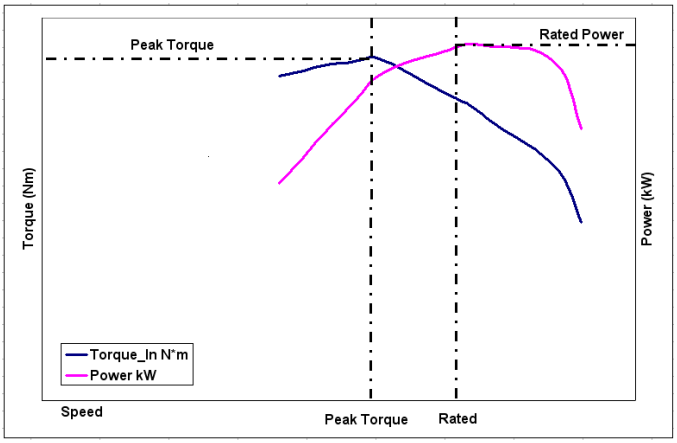

Figure 3.1.8. Speed-Torque & Speed-Power curve for the chosen cyclic application

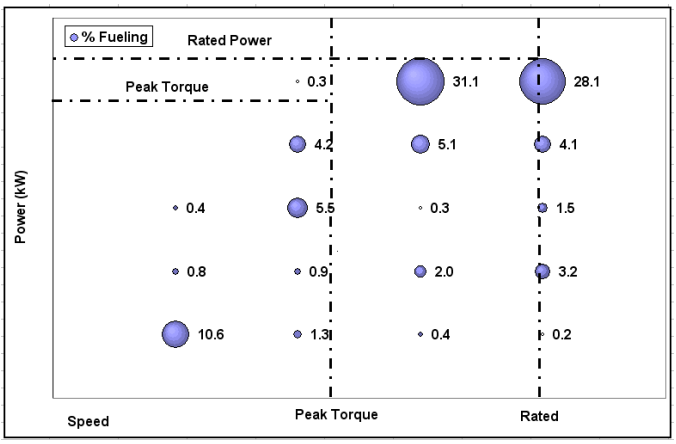

Figure 3.1.9. Histogram of fuel burnt at different operating conditions for the cyclic application

Figure 3.1.11 depicts various (engine, non-engine, overall system) efficiencies for the 4 energy source technologies being evaluated for this application. Since there is a significant amount of

part load operation for this application, the part load PCCI operation does result in a much more significant brake thermal efficiency improvement for the engine when compared to the baseline diesel case unlike the hauling application (~ 3% higher). This does make the cyclic off road application a much more attractive candidate for PCCI application with the current level of maturity of the technology when compared to hauling application. If the PCCI operation can be extended to the higher loads by the means of load extension technologies that allow a control on combustion pressure rises rates or combustion phasing, the improvement in the engine brake thermal efficiency can be of the order of 4-5%.

The lean burn natural gas engine was a lot less efficient (~ 3%) than the diesel engine primarily due to the larger throttling losses courtesy the longer part-load operations for the cyclic application and the lower compression ratio. The stoichiometric gasoline engine with an even lower compression ratio of around 9-10:1 due to the lower knock margin of gasoline has much lower engine thermal efficiency (4, 5% lower) when compared to the baseline diesel.

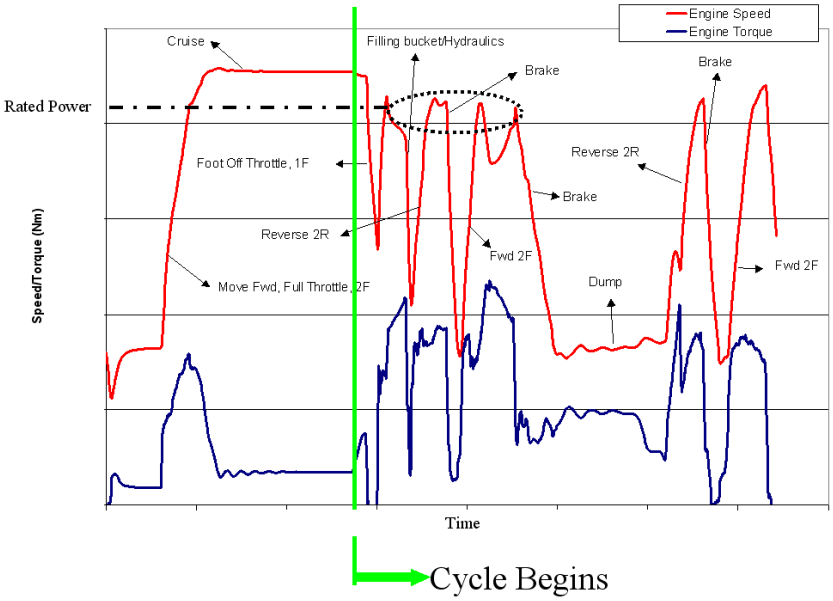

Figure 3.1.10. Typical speed-load time history for application cycle that was generated for cyclic application

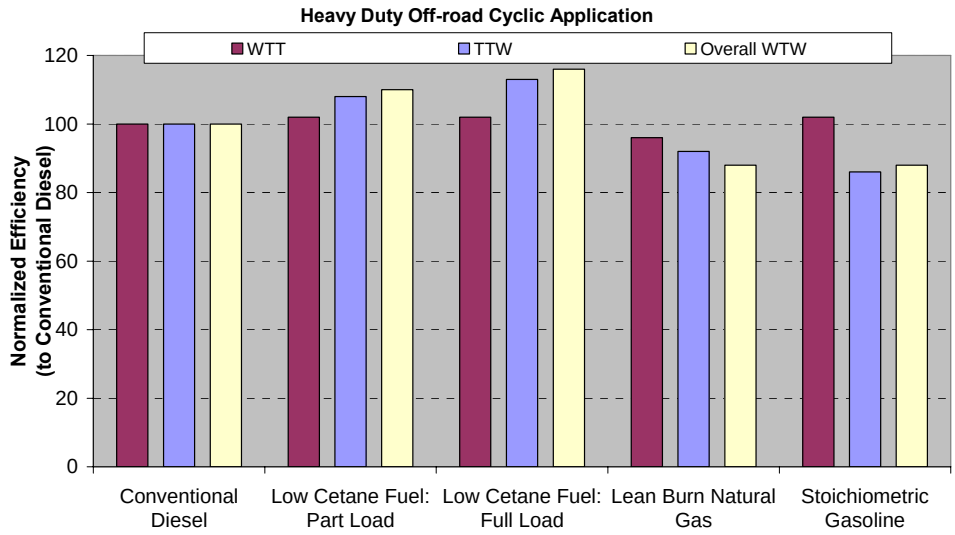

Figure 3.1.11. Efficiencies normalized to baseline diesel engine in cyclic application

Results for On-Highway Truck

3 different circuits were analyzed for the on-highway truck, namely a cruising circuit along the I-80 at a fairly constant speed of 60 MPH, a cross country circuit from Joliet, IL to San Francisco, CA which is a combination of highway and city driving and lastly a congested city driving circuit. For each circuit the total resistance was split into sub components of tire resistance, wind resistance, braking and grade.

Figure 3.1.12 shows the baseline diesel power/torque curves for the engine. The on highway truck engine fuel consumption is optimized for operation around the 1000-1500 RPM and peak torque operating point (~ 250-400 kW Power).

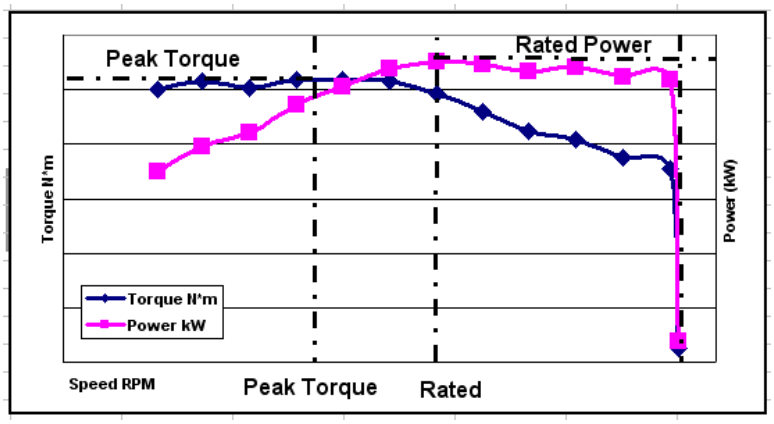

Figure 3.1.12. Speed-Torque & Speed-Power curve for on-highway truck application

The results for the overall truck efficiency for the I-80 circuit and the Joliet to San Francisco circuit shown in Figure 3.1.13 and Figure 3.1.14 are fairly similar since most of the driving even in the cross country circuit happens along the interstate where the engine is essentially maintaining a constant speed of around 60 MPH (Road Load operation and not operating near

the full load) with occasional acceleration/deceleration events depending on changes in grade and wind resistance. The benefits of full load PCCI combustion in both the cases are about 2-3 % when compared to the baseline diesel case. The natural gas and gasoline powered engines turn out to have ~ 2 to 4 % lower thermal efficiencies primarily due to the lower compression ratio and the higher throttling losses. The fact that the truck essentially sits at a constant speed means that the engine stays at part load operation for the most part and hence the throttling losses do become significant.

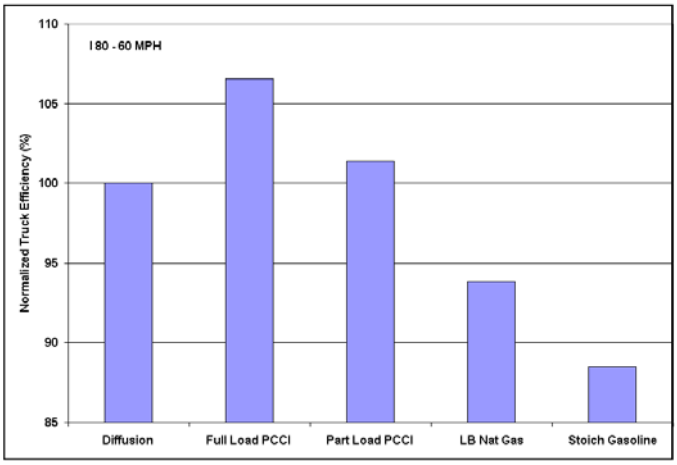

Figure 3.1.13. Overall efficiency normalized to baseline diesel engine for the I-80 circuit

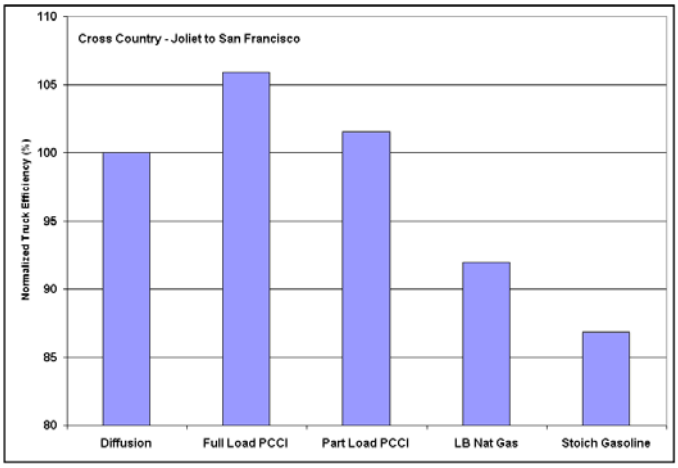

Figure 3.1.14. Overall efficiency normalized to baseline diesel engine for the Joliet to San Francisco circuit

Figure 3.1.15 depicts the overall truck efficiency for the congested city driving circuit. It is clearly seen that the stop and go nature of the circuit essentially involves a large extent of cycling between part and full loads leading to a much lower baseline diesel efficiency. The improvement for the part load PCCI case is marginally higher when compared to the I-80 and the cross-country circuits due to a larger amount of part load operation within the city driving circuit. Also the thermal efficiencies of the natural gas and the gasoline engines are lower when compared to the other 2 circuits again due to the larger degree of part load operation and its associated losses as mentioned before.

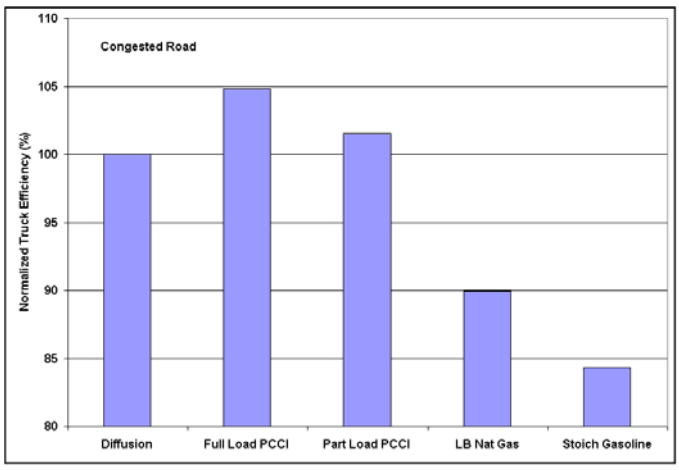

Figure 3.1.15. Overall efficiency normalized to baseline diesel engine for the congested city driving circuit

Figure 3.1.16 depicts the total drag (resistance) as a percent of the input fuel energy for the baseline diesel case and also the split up of the total drag into the various sub components for the 3 circuits. It is clearly seen that the total drag is a more significant portion of the input fuel energy for the circuits involving highway driving. In the city driving circuit, the engine itself being much less efficient requires a much larger fuel energy input and hence the total drag as a percentage of the higher fueling is lower. Also the significantly higher wind drag and tire rolling resistance is noticeable in the highway driving circuits. The constant stop and go nature of the city circuit adds a significantly higher portion of braking resistance.

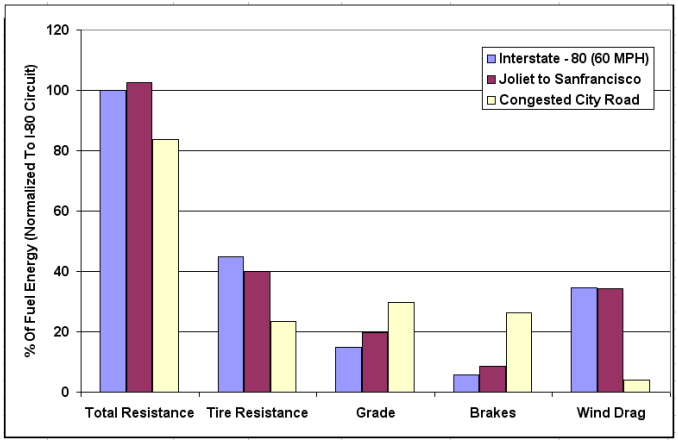

Figure 3.1.16. Total drag (resistance) as a percent of the input fuel energy for the baseline diesel case and also the split up of the total drag into the various sub components for the 3 circuits

Figure 3.1.17 depicts the different losses as a percent of the input fuel energy for the 3 different circuits. The engine losses are more significant for the city circuit, which is heavily, weighted towards a part load operation where the engine is less efficient. The drive train losses are

assumed to be constant over the 3 circuits. The total resistance as a percent of the input fuel energy is lower for the city driving case as shown before due a lesser efficient engine and also due to lower tire and wind resistances. The acceleration component essentially tracks the energy required to accelerate initially and also for transients (Wheel Energy Out – Total Resistance to be overcome).

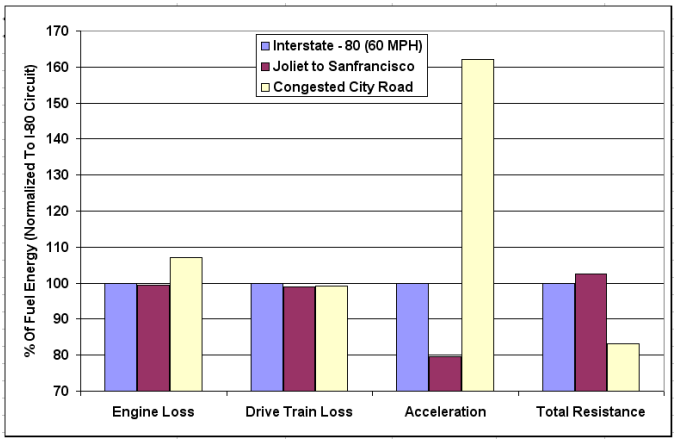

Figure 3.1.17. Losses as a percent of the input fuel energy for the 3 different circuits

3.2: 2nd Law Efficiency Analysis

Engine analysis tools based on the first law of thermodynamics have proven themselves as part of the design and development process and are in use today by every engine manufacturer. The increasing pressure to achieve significant reductions in fuel consumption have created a need for more detail on engine efficiency and performance so that designs can be better optimized. Adding an analysis based on the second law of thermodynamics can provide this necessary detail and has been used to reveal valuable information on losses within engines as well as to guide the development of efficiency-improving technologies. This report describes the present state of the art in engine simulations, a successful implementation of a second-law analysis into a common simulation code, and several notable results from the use of second-law modeling.

Introduction

While engine efficiency has always been an important concern, recent attention on future fuel-supply security and environmental concerns has further increased focus on achieving significant improvements in engine efficiency. Numerous thermodynamic studies of internal combustion engine performance have been conducted over the last several decades. These studies have shown that typically less than 50% of the energy content of the supplied fuel is converted to brake work. The remaining fuel energy is either consumed by system inefficiencies (such as combustion irreversibility and friction) or leaves the engine through various waste energy streams (including the exhaust, engine coolant, oil, and heat loss to the ambient environment). Incremental improvements in engine efficiency continue to be made using various techniques such as refining combustion timing, using advanced lubricants, and improving the efficiency of turbochargers, fuel and water pumps, and other auxiliary components. However, significant advances in engine efficiency will require reducing these major losses and recovering energy that would otherwise be lost to the environment.

The first law of thermodynamics (i.e., the conservation of energy) provides an accounting of fuel-energy usage within the engine and auxiliary systems and quantifies the energy contained in the various waste energy streams. But to determine the potential for reducing losses or recovering work from the waste energy streams, one must also consider the second law of thermodynamics. Whereas the first law is quantitative in nature, the second law assesses the thermal quality of energy streams and their potential to perform useful work. In the classic example, the atmosphere contains an enormous quantity of energy, but the quality of that energy is very low, making it extremely difficult to use that energy to do useful work. As another example, from a first-law basis, the quantity of energy removed from a particular engine through the charge-air cooler may be similar, or even greater than, the quantity of energy transferred through the EGR cooler of that engine. However, from a second-law basis, because of the significantly higher temperature of the EGR stream, the energy removed through the EGR cooler is of a much higher quality and has more potential to perform useful work.

A complete first- and second-law thermodynamic analysis of engine performance may be conducted using experimental data, engine simulation results, or a combination of the two. Analyses performed using experimental data alone are often limited by what information can be measured, resulting in much of the fuel energy remaining unaccounted for. Results from engine simulation tools can supplement the experimental data to provide greater insight into system performance. Commercial simulation tools such as GT-Suite® and WAVE® use conservation

equations for mass, energy, momentum, and chemical species to develop a solution without performing entropy or exergy balances to insure the second law is satisfied. However, recent releases of these program suites do provide the option of performing the entropy and exergy calculations after the fact.

Overview of Engine Simulation Tools

Results from engine simulation software can be used to complement experimental data and better refine the thermodynamic analysis. The engine model can be used to provide information which may be difficult or impossible to measure such as ambient heat loss, flow losses across the intake and exhaust valves, combustion losses, etc. Simulation results also allow for a time-based analysis throughout the engine cycle.

Such simulation codes typically model the entire engine air system, crank-train, and combustion chamber. The simulation of any particular component is significantly less detailed than if only that component were under analysis. For instance, the combustion modeling is very simple relative to modern computational fluid dynamics (CFD) analysis. By simplifying the model details for each component, a short overall simulation time is possible. This makes cycle simulation tools fast enough to be a core part of the design iteration process. For instance, selecting the appropriate turbocharger for a given application may require consideration of many possible turbine and compressor combinations. With a fast turnaround time, all combinations can be quickly evaluated in the simulation and the optimum configuration selected without requiring extensive on-engine evaluation.

In the past, many engine companies developed their own internal codes for performing this kind of analysis, such as Caterpillar's 973 code. However, commercial modeling software such as GT-Suite® from Gamma Technologies, Inc., WAVE® from Ricardo, Inc., or Boost® from AVL are increasingly being used to minimize the internal expense of developing and supporting a specialized code. All of these codes share a common approach with one-dimensional flow simulation in ports and manifolds, measured performance maps for turbines and compressors, and simplified combustion models. The software may also allow modeling of engine controllers, mechanical components such as the crank and valve trains and transmission, and auxiliary systems such as the fuel delivery, engine coolant, and exhaust aftertreatment systems. There are significant differences in the implementation of the simulation details that may recommend one code over another for a particular use. However, the similarities in overall approach mean that the analysis techniques presented here are suitable for any of these codes.

A major advantage of these products in comparison with detailed CFD models is the reduced computational time required for each simulation which allows for multiple engine designs and/or speed-load operation points to be evaluated in a timely manner. The reduction in computational time is primarily achieved by treating the flow solution as one-dimensional and tracking only a small number of chemical species. While the one-dimensional flow approach is adequate for many parts of the intake and exhaust system, various tuning factors are required to model the impact of obstructions such as bends and junctions in ducts. Determining the best way to model a complex manifold geometry to achieve accurate flow prediction is somewhat of an art, but the resulting computation time is orders of magnitude shorter than what a full three-dimensional simulation would require. Commercial codes such as GT-Suite and WAVE typically only track

the fuel and eleven other chemical species: N_2, O_2, H_2O, CO_2, CO, H_2, NO, and the free radicals H, O, OH, and N. This approach limits the number of kinetic reactions which need to be considered when determining the equilibrium concentrations of the combustion products. As a result, it is possible to pre-solve the equilibrium reactions and store the solution in look-up tables as a function of temperature and air-fuel ratio. These look-up tables can then be used to determine the composition of the combustion products more quickly than by solving the equilibrium reactions at each time-step of the flow solution.

To obtain the flow solution, the plumbing network of the engine is divided into numerous small control volumes. Conservation equations for mass, momentum, and energy are then solved for each of these control volumes. Specific heat relations for each species (such as the nine-coefficient NASA relations or the Shomate equations provided by NIST) are used to relate thermophysical properties such as internal energy, enthalpy, and entropy with the temperature, pressure, and chemical composition of the working fluid. Typically, the flow solution is obtained using a finite-difference approach with an explicit scheme for marching through time.

Combustion modeling must be greatly simplified for reasonable computational times. As with the flow calculations, these codes effectively zero- or one-dimensionalize the combustion process in order to reduce computational time. The most common approach is to model the fuel heat release as a superposition of Wiebe curves. By appropriate selection of the Wiebe parameters, a reasonable representation of heat release can be created for many combustion strategies. Clearly there is no predictive capability with this approach, and experimental data are required to tune the model. For cases where some predictive modeling is desired, one-dimensional combustion models for SI and CI combustion can be used. These models attempt to describe some of the physics of the combustion process in a simplified way. Tuning is still required during model development, but it can then be used to approximately simulate how the combustion process will respond to changes in engine conditions.

Turbochargers and superchargers are treated in a very simple fashion in cycle simulation models. Performance maps of turbine and compressor performance are generated on gas stands, and these maps are used in the simulation code to predict turbocharger behavior by balancing the turbine and compressor speeds and pressure ratios. Despite this simplicity, the results for turbocharger performance are generally very good. Thanks to this capability, cycle simulations are extensively used for turbocharger matching to engines for performance development, altitude rating, and so on.

The overall utility of cycle simulation codes is great, and they are a core part of the engine design and development process. The further capability enabled by incorporating these simulations into vehicle models to perform drive cycle simulations allows rapid development of transmission specifications, shift point selections, and emissions compliance strategies. As will be discussed later in this report, there are still aspects of engine development that are not addressed by cycle simulations as they currently exist. It is through adding the ability to perform second law thermodynamic analysis of the engine that yet more opportunity for leveraging cycle simulation codes may be unlocked.

Thermodynamic Analysis of Internal Combustion Engines

A complete thermodynamic analysis requires performing balances for energy and exergy. The general form of the conservation of energy is given in differential form by

$$\frac{d}{dt}(me)_{CV} = \sum_{in/out} \dot{m}\left(h + ke + pe\right) + \dot{Q} - \dot{W} \qquad (1)$$

The terms in this equation represent the rate of energy storage in the control volume and the rate at which energy enters and exits the control volume due to mass transfer, heat transfer, and work. The storage term includes internal, kinetic and potential energies.

Exergy provides a measure of the potential to perform useful work due to thermophysical and chemical differences between the working fluid and the ambient environment. The specific exergy of the working fluid is given by

$$a = a_{chem} + \left(u - u_o\right) - T_o\left(s - s_o\right) + P_o\left(v - v_o\right) + ke + pe\,. \qquad (2)$$

For the thermophysical properties indicated with the subscript 'o', the working fluid composition is frozen, and the properties are evaluated at ambient temperature and pressure with the working fluid at rest with minimum (local) potential energy. For gaseous mixtures, all water is assumed to remain as a vapor for agreement with standard first-law analysis methods based on the lower heating value of the fuel.

The chemical exergy of the working fluid depends upon the relative abundance of its constituent species in comparison to the ambient environment and should be considered when chemical reactions occur. The most important role of the chemical exergy is in determining the available energy introduced with the fuel. For practical purposes, only reactive species such as CO and unburned or partially burned fuel need to be considered when determining the chemical exergy. For gaseous or liquid mixtures, the chemical exergy can be determined by

$$a_{chem} = \frac{1}{MW}\left(\sum_j y_j b^o_{ch,j} + R_u T_o \sum_j y_j \ln\left(y_j\right)\right) \qquad (3)$$

with the standard chemical exergies of each species, $b^o_{ch,j}$, taken from tabulations of values determined according to the method of Szargut [1-3].

Unlike mass and energy, exergy is not a conserved quantity, and inefficient, entropy-generating processes result in unrecoverable losses which destroy some of the working fluid's work potential. The general form of the exergy balance,

$$\frac{d}{dt}(ma)_{CV} = \sum\left(1 - \frac{T_o}{T_B}\right)\dot{Q} - \left(\dot{W} - P_o \frac{d}{dt}V_{CV}\right) + \sum_{in/out} \dot{m} a_f - \dot{I}\,, \qquad (4)$$

is obtained by combining the first law with an entropy balance for the system. The terms in this equation represent the rate of exergy storage in the control volume, the rate of exergy transfer to or from the system due to heat transfer, work, and mass transfer, and the rate of exergy destruction (or irreversibility). The mass flux term in Equation 4 includes the exergy transported in or out of the control volume with the mass as well as the flow work required. For simplicity, these two contributions are typically combined as flow exergy

$$a_f = a_{chem} + \left(h - h_o\right) - T_o\left(s - s_o\right) + ke + pe\,. \qquad (5)$$

Flow exergy should not be confused with the exergy stored within the control volume.

The general forms of the energy and exergy balances given in Equations 1 and 4 may be applied to analyze the engine as a whole or individual components such as the engine cylinder, turbocharger, etc. When using time-based simulation results to perform a detailed analysis of energy usage throughout the engine cycle, few simplifications can be made to the general forms (other than neglecting changes in potential energy). The rate-of-storage terms on the left-hand side of Equations 1 and 4 cannot be neglected due to the unsteady flow solution provided by time-based simulation results. Changes in kinetic energy are generally small and could be neglected throughout the engine except at the intake and exhaust valves where flow velocities can be quite high. However, simulation tools such as GT-Suite®, WAVE®, and 973 provide values for total energy and total enthalpy which combine the kinetic energy term with internal energy and enthalpy, respectively. Thus it would require more effort to neglect kinetic energy from the analysis than to include it. Note, however, that the terms u_o in Equation 2 and h_o in Equation 5 must be evaluated with the working fluid at rest.

To avoid accounting for friction multiple times, it can be assumed that all friction losses are converted to heat. Brake engine power (as opposed to indicated power) should then be used in the work terms in Equations 1 and 4. This approach also eliminates the need for the work term related to volume change in Equation 4. The work term must also include any additional power inputs or outputs such as turbo-compounding power output or power supplied to/by any auxiliary equipment not included in the analysis.

The heat transfer term in Equation 4 represents the portion of heat transfer which may be recovered from the medium to which the heat is transferred (e.g., coolant, oil, etc.), where T_B is the temperature of that medium. The remaining portion of the heat transfer is lost due to entropy generation (because the heat transfer occurs across a finite temperature difference) and is included as part of the irreversibility term. For radiant and convective losses to the ambient environment, $T_B = T_o$, and all of the heat energy is lost. If the heat transferred to the coolant and oil is not recovered, it will also be lost to the environment through the radiator.

With these modifications, the energy and exergy balances for time-based analysis of the entire engine can be rewritten as

$$\frac{d}{dt}\left(m\hat{u}\right)_{CV} = \sum_{in/out} \dot{m}\,\hat{h} + \dot{Q} - \dot{W}_b \tag{6}$$

and

$$\frac{d}{dt}\left(m\,a\right)_{CV} = -\dot{W}_b + \sum_{in/out} \dot{m}\,a_f - \dot{I} \tag{7}$$

where, now,

$$a = a_{chem} + \left(\hat{u} - u_o\right) - T_o\left(s - s_o\right) + P_o\left(v - v_o\right) \tag{8}$$

and

$$a_f = a_{chem} + \left(\hat{h} - h_o\right) - T_o\left(s - s_o\right). \tag{9}$$

Here, all heat transfer is assumed to be lost to the ambient environment either directly or through the radiator, and brake engine work is the only work assumed to cross the control volume

boundary. For steady-state or cycle-based analysis, the energy and exergy balances can be further simplified by eliminating the rate-of-storage terms such that

$$\sum_{in/out} \dot{m}\,\hat{h} = \dot{W}_b - \dot{Q} \tag{10}$$

and

$$\dot{I} = \sum_{in/out} \dot{m}\left[a_{chem} + \left(\hat{h} - h_o\right) - T_o\left(s - s_o\right)\right] - \dot{W}_b\,. \tag{11}$$

All of the parameters required by the equations above (including exergy, chemical exergy, and flow exergy) can be obtained from the simulation output of a GT-Suite® model with the exception of irreversibility which must be determined using either Equation 7 or 11. The analysis can be performed for the engine as a whole or for individual components such as the engine cylinder, turbocharger, EGR cooler, etc. The latest release of WAVE® advertises to provide similar information (though we have not evaluated this release).

However, when working with experimental engine data, much of the required information must be determined or inferred, and analysis is limited to steady-state operation or long time-scale transients (such as over a driving schedule). Kinetic energy can be neglected (except perhaps at the intake and exhaust valves). Thermophysical properties of the working fluid such as the density (or specific volume), internal energy, enthalpy, and entropy must be determined based on measurements of pressure, temperature, and working fluid composition at locations of interest within the engine. Exhaust sampling provides an approximate composition for the exhaust gas which can be used to estimate enthalpy and entropy based on temperature and partial pressure using either the Shomate equations provided by NIST or the nine-coefficient NASA functions for each gaseous component. Heat losses to the coolant and oil can be approximately measured, but ambient losses must be inferred from the first law using Equation 10.

Applications for 2nd Law Analysis in the Engine Development Cycle

Second-law analysis has been increasingly used to understand the losses in engines and how to mitigate them. J. A. Caton of Texas A&M University has been particularly active in applying this approach to the study of engine efficiency [4-7]. This series of papers has evaluated various aspects of the operation of a spark-ignited engine operating across a typical light-duty speed/load range. The model used by Caton provides insight into combustion irreversibility, flow irreversibility, and the impacts of oxygen concentration and EGR fraction.

One outcome of interest from these papers is the issue of combustion irreversibility. In a properly functioning modern engine, the first-law combustion efficiency is greater than 98%, meaning that only a small fraction of the fuel remains unburned when the engine cycle is completed. However, the second-law analysis in [4] indicates that around 21% of the fuel exergy is destroyed in the combustion process, as can be seen in Figure 3.2.1. The large discrepancy between the nearly 0% loss indicated by the first-law analysis and the 21% loss from the second-law analysis comes from the difference in what the two measures reflect. The first-law analysis only indicates that the fuel was reacted, but the second-law analysis reflects that some of the fuel's ability to do work is lost in the chaotic combustion process. The size of this loss is sufficiently large that there is a strong desire to reduce it. For conventional combustion, Caton has shown that there is very little that can be done to reduce this particular loss. However, this kind of analysis has led C. S. Daw of Oak Ridge National Laboratory to probe how the

combustion process might be redesigned to reduce this loss [8]. The present approach is to use recuperation to prepare the combustion products prior to burning. This is a long-range approach to efficiency improvement. However, it would not be considered at all if the second-law analysis of combustion were not performed.

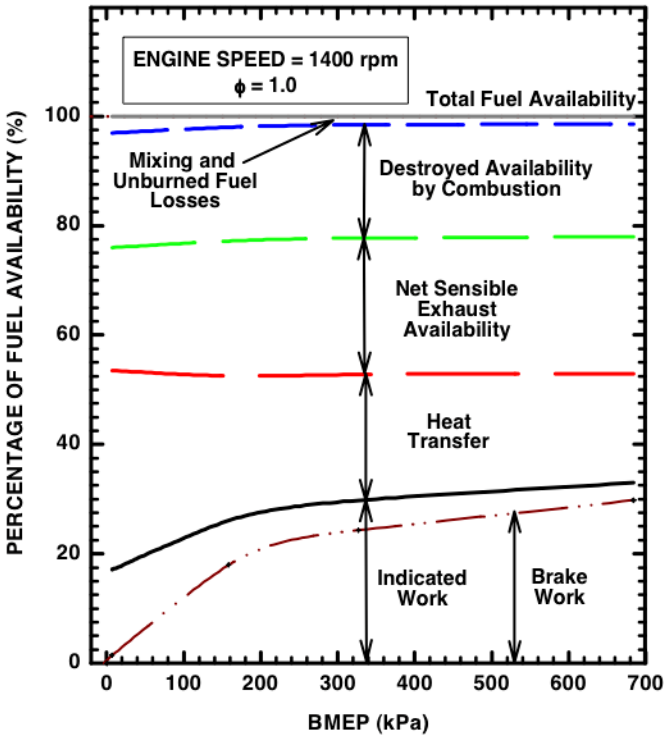

Figure 3.2.1. Fuel exergy as a function of load at a fixed engine speed, from Caton [1]

The second-law modeling performed by K. D. Edwards of ORNL has revealed aspects of engine design and operation that can be addressed more immediately [9]. This work has involved evaluating the impact of advanced combustion strategies on engine efficiency. The study explored the effect of increasing the effectiveness of the intercooler. This change increased heat loss in the intercooler, but lowered the heat losses to the block, head, and exhaust manifold and increased the overall engine efficiency. This change also lowered the exergy loss due to heat transfer in the engine. The effect of insulating the exhaust manifold was also examined, showing a increase of 4% in the exhaust exergy. This increase could be used to support aftertreatment needs or to drive a bottoming cycle.

The studies by Edwards have extended to evaluating the potential of various waste heat recovery system to improve light-duty engine efficiency. For this work the second-law analysis is invaluable. Not only does it fully quantify the energy and exergy flows in the various energy streams available (coolant, EGR, exhaust) but it quantifies the maximum amount of work that can be performed by any thermodynamic cycle using those streams as an energy input. These results have been used to guide the experimental waste heat recovery program at ORNL as well as to evaluate the results from that program [10-11]. This program evaluated the energy and exergy streams on a light-duty diesel engine to determine the most effective way to achieve an overall brake engine efficiency of 45%. The second-law analysis revealed that while the engine

coolant energy flow was nearly as large as the exhaust energy flow, the exergy was sufficiently low to make achieving the required efficiency difficult. The analysis also revealed that the EGR loop carries roughly the same exergy flow at part load as does the exhaust stream. While not directly useful for achieving the peak efficiency goal, this is a vital result for designing a system to operate at road loads where there is a significant EGR flow. To date the study has not been extended to evaluate the impact of low temperature combustion modes on the waste heat recovery system, but it is expected that a second-law analysis will again reveal key details that will guide the integration of such a system.

Implementation of 2nd Law Analysis in Caterpillar's 973 Code

An approach similar to that detailed in Edwards [9] was taken to implement a second-law thermodynamic analysis in Caterpillar's 973 cycle simulation code. The details of this implementation are fully documented in a separate report [12] and are simply reviewed here. For this implementation the output files from 973 were used to provide data for first- and second-law analyses of the engine. An ORNL-developed code calculated enthalpy, internal energy, and entropy for the engine flows and in-cylinder mixture. The results were shown to match the thermodynamic results from 973 well and provide details on irreversibilities in the engine that are not available from 973.

The model was used to examine the impact of coolant temperature increases and exhaust manifold insulation on the engine efficiency. Figure 3.2.2 shows the impact of coolant temperature on the engine power and energy flows. For this particular case the engine power is not significantly affected, but the increase in coolant temperature does increase the exergy in the exhaust and coolant flows. This is a useful trend if a bottoming cycle is to be employed.

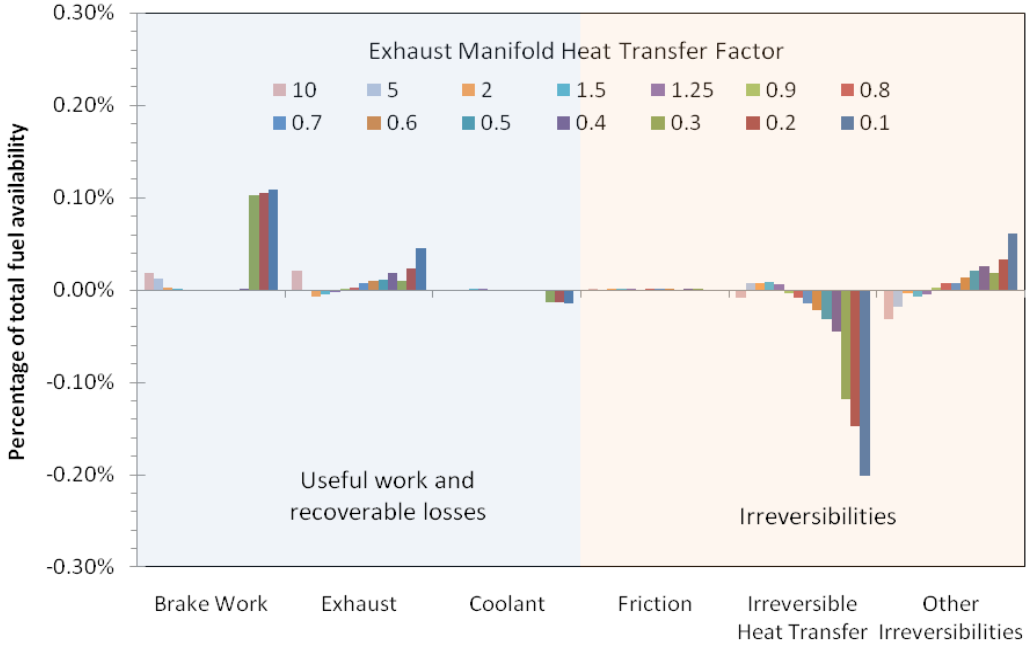

Figure 3.2.2. Impact of coolant temperature on exergy distribution

The use of the second-law code could be extended to other advanced R&D studies to guide engine optimization and powertrain system design. The exergy distribution over different operating cycles can vary widely, leading to different design choices depending on the particular engine application under study.

Conclusions

As more stringent carbon emission regulations come into play there will only be more need to extract maximum work from the fuel burned in the engine. The coupling of the combustion system, the aftertreatment system, and hybrid systems will demand having full thermodynamic information to create the best overall powertrain solution. Achieving significant gains in engine efficiency requires a full and quantitative understanding of the thermodynamic state of the engine. Adding second-law analysis to existing engine simulation tools can provide this understanding and reveal opportunities for engine improvement that would otherwise be missed.

This report has shown the details of implementing a second-law analysis for an engine simulation code and provided several examples of the results such an analysis can provide. Given the limitless range of engine designs, operating conditions, and applications it is impossible to address the full range of uses of this analysis. The presented results do indicate the utility of the tool though, and reinforce the value of making use of it.

REFERENCES

1. D. R. Morris, J. Szargut, "Standard chemical exergy of some elements and compounds on the planet Earth", *Energy*, 11:8, pp 733-755, 1986.
2. J. Szargut, "Chemical exergies of the elements", *Applied Energy*, 32:4, pp 269-286, 1989.
3. J. Szargut, A. Valero, W. Stanek, A. Valero, "Towards an international reference environment of chemical exergy", *Proceedings of 15th International Conference on Efficiency, Cost, Optimization, Simulation and Environmental Impact of Energy Systems (ECOS 2002)*, 2005, http://www.exergoecology.com/papers/towards_int_re.pdf.
4. J. A. Caton, *Operating Characteristics of a Spark-Ignition Engine Using the Second Law of Thermodynamics: Effects of Speed and Load*, SAE Technical Paper 2000-01-0952.
5. J. A. Caton, *Use of a Cycle Simulation Incorporating the Second Law of Thermodynamics: Results for Spark-Ignition Engines Using Oxygen Enriched Combustion Air*, SAE Technical Paper 2005-01-1130.
6. R. G. Shyani and J. A. Caton, *Results from a Thermodynamic Cycle Simulation for a Range of Inlet Oxygen Concentrations Using Either EGR or Oxygen Enriched Air for a Spark-Ignition Engine*, SAE Technical Paper 2009-01-1108.
7. J. A. Caton, *A Thermodynamic Evaluation of the Use of Alcohol Fuels in a Spark-Ignition Engine*, SAE Technical Paper 2009-01-2621.
8. V. K. Chakravarthy, C. S. Daw, J. A. Pihl, J. C. Conklin, *Study of the Theoretical Potential of Thermochemical Exhaust Heat Recuperation for Internal Combustion Engines*, Energy and Fuels, vol. 24:3, pp. 1529-1537, 2010.

9. K. D. Edwards, R. M. Wagner, R. L. Graves, *Identification of Potential Efficiency Opportunities in Internal Combustion Engines Using a Detailed Thermodynamic Analysis of Engine Simulation Results,* SAE Technical Paper 2008-01-0293.
10. T. E. Briggs, R. M. Wagner, K. D. Edwards, S. Curran, E. J. Nafziger, *A Waste Heat Recovery System for Light Duty Diesel Engines,* SAE Technical Paper 2010-01-2205.
11. K. D. Edwards, R. M. Wagner, T. E. Briggs, *Investigating Potential Light-Duty Efficiency Improvements Through Simulation of Turbo-Compounding and Waste-Heat Recovery Systems,* SAE Technical Paper 2010-01-2209.
12. B. C. Kaul, K. D. Edwards, T. E. Briggs, R. M. Wagner, *High efficiency enabling technologies for heavy-duty Diesel engines,* ORNL Report to Caterpillar, 2009